CENTRO DE INVESTIGACIÓN Y DE ESTUDIOS AVANZADOS
DEL INSTITUTO POLITÉCNICO NACIONAL

UNIDAD ZACATENCO
DEPARTAMENTO DE FÍSICA

"Propagación de la luz en Electrodinámica No Lineal"

Tesis que presenta

Elda Guzmán Herrera

para obtener el Grado de

Doctora en Ciencias

en la Especialidad de

Física

Directora de tesis: Dra. Nora Eva Bretón Báez

Ciudad de México Junio, 2024

CENTER FOR RESEARCH AND ADVANCED STUDIES OF THE
NATIONAL POLYTECHNIC INSTITUTE

PHYSICS DEPARTMENT

“Light propagation in Nonlinear Electrodynamics”

by

Elda Guzmán Herrera

In order to obtain the

Doctor of Science

degree, speciality in

Physics

Advisor: Ph. D. Nora Eva Bretón Báez

Mexico City June, 2024

Agradecimientos

The work has been sponsored by CONAHCyT-Mexico through the Ph.D. scholarship No.761878.

Abstract

Light propagation in an intense electromagnetic field background is examined from the perspective of three different nonlinear electrodynamics (NLED) theories, Euler-Heisenberg, Born-Infeld, and ModMax. The effective metric approach is used to determine the light phase velocity.

For the case of Euler-Heisenberg (EH), using a Lorentz boost, it is considered the situation when the background is in movement, modeling then a magnetized flowing medium. We determine how this motion affects the speed of propagation of the electromagnetic wave. Since this theory exhibits birefringence there are two possible phase velocities that depend on the magnetic background and the direction and velocity of the boost.

In a background of purely magnetic or electric Born-Infeld (BI) fields we examine light propagation from the point of view of an accelerated observer, situated in a Rindler frame. The phase velocity as measured by the Rindler observer increases, in some cases even exceeding the one in vacuum; however, the BI background field tends to decrease it. We consider light propagating parallel or transversal to the acceleration direction of the Rindler frame. Moreover, we determine the redshift of light pulses sent from one Rindler observer to another.

Euler-Heisenberg and ModMax are nonlinear theories that present birefringence, i.e. the phase velocity depends on the intensity of the external electromagnetic field as well as on the polarization of the wave.

Regarding ModMax NLED theory, the static spherically symmetric solution of the ModMax NLED coupled to the Einstein equations represents a black hole and we analyze light propagation in its vicinity; we determine light trajectories, deflection, redshifts, as well as the shadow of the black hole. The results are compared with the corresponding effects in the neighborhood of the Reissner-Nordstrom black hole, which is the static spherically symmetric solution to the Einstein-Maxwell equations.

For completeness, we compare the diminishing in the phase velocities as measured by a still observer, another one in uniform motion by means of a Lorentz boost, and also an accelerated observer (in the Rindler frame) for the three NLEDs: EH, BI, and ModMax. Moreover, we consider the black hole solutions for each NLED coupled to the Einstein gravity and we compare the shadow radii of the corresponding black holes with the observed shadow of the black hole in the center of our galaxy, Sagittarius A^*.

Resumen

Se examina la propagación de la luz en presencia de un campo electromagnético intenso mediante tres teorías de electrodinámica no lineal: Euler-Heisenberg, Born-Infeld y ModMax y se compara con la electrodinámica de Maxwell. Usamos el concepto de métrica efectiva para determinar la velocidad de fase de la luz.

Para el caso de Euler-Heisenberg (EH), se modela la situación de un medio magnetizado en movimiento mediante una transformación de Lorentz. Determinamos cómo esta transformación afecta la velocidad de propagación de la onda electromagnética, resultando que las velocidades de fase dependen tanto del campo magnético de fondo como de la dirección de la velocidad de la transformación de Lorentz.

Por otra parte, se considera la propagación de la luz en presencia de un campo de Born-Infeld (BI) puramente magnético o puramente eléctrico y se analiza la situación desde el punto de vista de un observador acelerado haciendo uso del marco de Rindler, resultando que el campo de BI y el marco acelerado tienen efectos opuestos sobre la velocidad de propagación de la luz: el campo de BI tiende a disminuir la velocidad de fase, mientras que en el marco acelerado se observa un incremento, en algunos casos incluso excediendo la velocidad de la luz en vacío. Consideramos ambos, propagación de la luz paralela o tranversal a la dirección de la aceleración del marco de Rindler; también se calcula el corrimiento al rojo de pulsos de luz enviados desde un observador de Rindler a otro.

Las teorías de Euler-Heisenberg y ModMax son las que presentan birrefringencia, es decir, la velocidad de fase de la onda electromagnética que se propaga depende de la intensidad del campo electromagnético externo y de la polarización de la onda.

En cuanto a la teoría de ModMax, estudiamos la solución estática y esféricamente simétrica de la teoría de ModMax acoplada con las ecuaciones de Einstein, es decir, el agujero negro de ModMax. Analizamos la propagación de la luz en la vecindad del agujero negro de ModMax y determinamos las trayectorias, deflección, corrimiento al rojo y la sombra del agujero negro. Estos resultados son comparados con los efectos correspondientes al agujero negro de Reissner-Nordstrom, el cual es la solución estática y esféricamente simétrica de las ecuaciones de Einstein-Maxwell.

Por completez, comparamos la disminución en las velocidades de fase para los casos en que el observador está en reposo, en movimiento uniforme, mediante una transformación de Lorentz, así como el caso de un observador acelerado, visto desde el marco de Rindler, para las tres electrodinámicas no lineales estudiadas: EH, BI y ModMax. Además se consideran las soluciones estática y esféricamente simétrica de agujeros negros cuando se acopla cada electrodinámica a la gravitación de Einstein y se confrontan los radios de las sombras resultantes con el radio de la sombra observado para el agujero negro en el centro de nuestra galaxia, Sagitario A^*.

Contents

Chapter 1

Introduction

Light propagation in the presence of an electromagnetic field, in vacuum or in a medium, has been discussed throughout the history of humanity, at least since Euclid in the IV century BC. There are questions that even today have not yet been answered, mostly due to technical advances not being sufficiently precise. In the next section, we give a historical review of the evolution of light propagation studies and how it is affected in the presence of an electromagnetic field.

1.1 Historical review

Euclid's "*Optica*" is considered the first treaty about light and its properties described through geometry [1]–[3]. However, at that time and for many years, the propagation of light was considered to be instantaneous or with an infinite velocity. Around the same time (350 BC) the concept of vacuum was also discussed by Aristotle's "*Physics*", who denied the possibility of vacuum, known at the time as void [4]. Although in other parts of the world, other scholars like Al-Farabi also rejected the existence of vacuum, some other physicists supported the existence of a void [5], [6].

These lines of thinking were carried through the years and while at the beginning of 1600 propagation of light was still considered to be instantaneous, it had been verified that the velocity of light changed according to the medium of propagation [1]. In 1676, M. Roemer observed Jupiter's satellite, Io, and confirmed that light required time to travel a certain distance [1], [7]; this, jointly with the observation of stellar aberration (celestial objects that appear to be in a different position towards the direction of motion of the observer) helped to reach a consensus on the finiteness of the velocity of light. The concept of vacuum also evolved; in 1640 E. Torricelli was able to measure the weight of the air and successfully produced a vacuum while in Germany (1650) the

vacuum pump was invented and it allowed R. Boyle to investigate the properties of vacuum [8].

Some observed phenomena raised more questions about vacuum: reflection, refraction, and diffraction. Around 1621, W. Snell described the relationship between angles of incidence and refraction, and the laws of refraction are named after him. Around 1662, P. Fermat explained refraction using the principle of minimum time (Fermat's principle).

In the meantime, physicists were also debating about two interpretations of light. In Newton's "*Optics*" (1704), he applied the particle interpretation of light to explain reflection; however, regarding diffraction and refraction he had some wrong assumptions related to the corpuscular interpretation of light [9]. In contrast, in 1690 C. Huygens proposed the idea of wavefronts produced by light sources (Huygens-Fresnel principle) and with it explained reflection and refraction. The wave interpretation was also accepted by L. Euler, who, in 1746, argued that by assuming light as a wave an easier explanation for diffraction can be obtained. Moreover, T. Young, in 1799, experimented on light and he formulated the principle of interference [10]. Later, A. Fresnel's wave theory became more accepted in 1815, since it explained the phenomena of diffraction, polarization, and birefringence [10]. Even so, it was believed that these waves moved through a medium called aether, although Fresnel's explanation did not employ this concept at all.

Meanwhile, it was considered that light could not be affected by magnetism until 1845, when M. Faraday observed that linear polarization of light rotates when light propagates in the presence of a magnetic field, and the degree of rotation depends on the strength of the magnet; this is a magneto-optical effect known as the *Faraday rotation*. Following Faraday's work, J. C. Maxwell interpreted electric and magnetic phenomena and, although his investigation was particularly abstract at the time, it did not rely on the concept of aether [10]. However the scientific community was reluctant to abandon the aether idea, and it was still considered that electromagnetic processes happened in this aether, which could be characterized by certain properties depending on the position. With this in mind, some experiments intended to measure these properties [10]–[15]. However, the efforts were in vain; in 1887 A. A. Michelson and E. Morley published their null result to measure the aether drift; this is now considered the first step to the birth of A. Einstein's theory of Special Relativity (SR). Considerable resistance faced SR to be trusted because it was difficult to perform direct experiments due to the high velocities required to observe SR effects. At the moment, even Michelson and Morley's interferometer and the observation of stellar aberration were not convincing enough.

In 1907 H. Minkowski formulated Einstein's SR theory in terms of tensors in a 4-dimensional geometry. Einstein's studies on the 4-dimensional geometry and tensors led him to become familiar with the works of B. Riemann, G. Ricci-Curbastro, and T. Levi-Civita; curvature ideas eventually resulted in the formulation of the General Theory

of Relativity (GR) in 1915 [10]. However, GR was a theory that needed experimental support unreachable for the technological landscapes at that time. To distinguish between Special Relativity and Newton's theory, high velocities were needed; while for GR evidence, intense gravitational fields were required. In the solar system, our greatest source of a gravitational field is the sun, therefore astronomers looked for GR proofs. It was found that GR explained Mercury's perihelion and then the problem of the solar redshift, but it was decades later, with technological advances, that more precise tests of GR were achieved.

Returning to the study of light affected by electromagnetic fields, Einstein understood that if a magnetic field would affect light propagation, the dependence on the magnetic field must be squared, B^2, because the direction of the field should not affect the decrease in the velocity of light. Moreover, a magnetic field affects the velocity of light through the refraction index, but Maxwell's theory is a linear theory that fulfills the superposition principle and it cannot describe self-field interactions. It was quantum electrodynamics (QED) formulated by R. Feynman, J. Schwinger, and S. Tomonaga that unblocked the problem. In particular, Schwinger in 1950 analyzed the polarization of vacuum that occurred in the presence of an electromagnetic field and concluded that nonlinear properties of the electromagnetic field could give a reliable description of the phenomenon; this is, electromagnetic fields affect the properties of the quantum vacuum and a nonlinear theory could describe it [16].

With nonlinearity in mind over the years nonlinear theories of electrodynamics have emerged. We focus on three in particular, Euler-Heisenberg, Born-Infeld, and the modified Maxwell, ModMax.

In 1934 M. Born and L. Infeld developed a nonlinear electrodynamics (NLED) theory [17] that is a nonlinear correction to Maxwell electrodynamics from a classical perspective. The aim was to contribute to the discussion on the nature of the electromagnetic mass of charged particles; at that time the opinion was divided as to whether the mass of a charged particle is a manifestation of the electromagnetic field or if the field and particle are two separate entities. A second aim was to solve the singularity of the field and energy of a point charge at its position, proposing the existence of a maximum attainable electromagnetic field, as a resemblance of the maximum attainable velocity in SR.

Later in 1936, H. Euler and W. Heisenberg derived a nonlinear electrodynamics theory from QED principles [18]. After P. Dirac's works on the positron (1933) and the Born QED, Heisenberg became interested in the quantum fluctuations of QED vacuum and realized that those fluctuations lead to the scattering of light by light; since the self-interaction of fields is not sustained by Maxwell's theory due to the linear superposition principle, the theories that explain the phenomena had to be nonlinear in the fields. H. Euler and B. Kockel were, at the time, students of Heisenberg and were put to the task of studying light-light scattering. In 1935, Euler and Kockel published the results for the light-light scattering amplitude in the low-frequency limit [19], [20]. This paper

established the idea that vacuum could be interpreted as a medium.

However, by calculating the light-light scattering interaction cross-section, they concluded that the effect was small, and then, measuring this deviation from Maxwell ED was difficult. In 1936, Euler and Heisenberg extended those results by applying the concept of a critical field strength E_{cr}, also called the Schwinger critical field $E_c \sim 10^{18} V/m$.

After the Euler-Heisenberg paper was published, V. Weisskopf stated the physical significance of the new nonlinear theory

> "The electromagnetic properties of the vacuum can be represented by a field-dependent electric and magnetic polarizability of empty space, which leads, for example, to refraction of light in electric fields or scattering of light by light."[20], [21]

By treating the vacuum as a medium, EH effective action predicts rates of nonlinear light interaction processes considering vacuum polarization to one loop and is valid for electromagnetic fields that change slowly compared to the inverse of the electron mass.

More recently in 2020, it was derived from the Modified Maxwell nonlinear theory. This theory fulfills the same symmetries as Maxwell's theory, which are: conformal invariance and electric-magnetic duality invariance.

1.2 Measuring nonlinear effects

Regarding the experimental evidence of electromagnetic nonlinear effects, for example, vacuum birefringence or photon-photon scattering, we mention some experiments concerning the measurement of the variation of light velocity.

Two types of experiments exist to measure the variation of light velocity when it is in the presence of an intense electromagnetic field. The first type is the interferometers but the limits obtained are 14th orders of magnitude higher than the ones predicted by QED [22]. The second type of experiment focuses on measuring vacuum polarization effects [23].

Some of the experiments to prove vacuum birefringence are the BFRT Collaboration [24], PVLAS Collaboration[25]–[27] and the BMV group [28]. The BFRT Collaboration experiment used a superconducting magnet which provided a magnetic field of 3.5T [24]. PVLAS experiment consists of a Fabry-Perot optical cavity and a superconducting magnet providing a 2.3T magnetic field, and a more recent version of this experiment was based on two 2.5T permanent magnets [27]. The BMV experiment uses pulsed magnetic fields, that allow it to reach the highest magnetic field in terrestrial laboratories of 6.5T [28]. Nonetheless, these experiments do not reach the predictions of QED in measuring vacuum birefringence and the BMV recognizes that the improvement needed is of three orders of magnitude [28].

QED vacuum nonlinearities have also been detected using waveguides [29]. Vacuum pair production, known as the Sauter-Schwinger effect [16], was predicted in the EH 1936 paper, however, the necessary electric field strengths, corresponding to a critical laser intensity of about $I_{\rm cr} = 4.3 \times 10^{29}$W cm^{-2} [30] have not yet been reached experimentally. New scenarios have been proposed to establish limits for the detection of vacuum birefringence [31].

The other phenomena that could be useful to measure or set bounds on NLED is the analysis of photon-photon scattering or photon splitting. Light-by-light interactions can be studied using heavy-ion collisions; the electromagnetic (EM) field strengths produced, for example by a Pb nucleus, are up to 10^{25} V m^{-1}. These intense EM fields can be treated as a beam of quasi-real photons, and light-by-light scattering has been measured in $Pb + Pb$ collisions at the Large Hadron Collider (LHC) [32], [33]. Other experimental evidence includes the measurement of photon splitting in strong magnetic fields [34], [35]. A larger study in experiments using intense laser and energetic particle beams focusing in QED is presented in [36] and a more recent review of photon-photon scattering at LHC can be consulted in [37].

To reach QED predictions there is needed a stronger magnetic field source, that from now is only achievable in astrophysical objects. Strong magnetic fields are also of interest in astrophysics; as neutron stars can possess magnetic fields in the range of $10^6 - 10^9$ Tesla, processes such as photon splitting and pair conversion are expected to occur in their vicinity [38], [39].

On the other hand, it is well known that an electromagnetic wave traveling through intense EM fields reduces its phase velocity due to vacuum polarization. This subject has been addressed since the 1970s in the literature [40], [41], as well as recently; see for instance [42], [43] for the EH theory, and [44] for wave propagation in a BI background. In [45], the use of a Michelson-Morley interferometer is proposed for measuring the changes in the phase velocity due to NLED theories, specifically the Born-Infeld theory. They concluded that for a BI parameter of the order $b \approx 10^{20}$ V m^{-1}, the intensity of the background fields in question will not be attained experimentally in the near future. Instead, using realistic intensities of background fields ($B \approx 1$T), interferometric experiments could place bounds on the BI parameter b to an order of $10^{14} - 10^{15}$ V m^{-1}. In [46] it is explored the change in the refraction index due to the NLED, the proposed experiment aims to measure the refraction of a laser pulse when it crosses a transverse vacuum index gradient, produced by an intense pump pulse using a Sagnac interferometer.

In [22] a general framework for experiments that intend to test QED predictions is presented, and it would make it possible to test different NLED theories.

1.3 Motivation to investigate NLED

Nonlinear electromagnetic effects can be taken into account in a phenomenological way by classical theories. Vacuum in the presence of strong magnetic and/or electric fields behaves in some aspects like a material medium; however, the description will be, in general, more complex than for simple polarizable media due to the nonlinear dependence of the Lagrangian on the fields and many of these effects are subtle even for magnetar field strengths, of the order of $10^9 - 10^{11}$ Tesla. If the index of refraction has an imaginary part then the effect of dichroism is present and it refers to the absorption of photons in vacuum depending on photon polarization [47].

Furthermore, each possible light trajectory is a null geodesic of an effective metric, and there are two possible effective metrics. Therefore this is an effect of the nonlinearity in the Lagrangian that results in birefringence in vacuum [48], meaning that electromagnetic waves with different polarizations have different velocities.

In a material medium, like anisotropic crystals, the notion of birefringence becomes evident as there are two rays of light propagating in the crystal with different phase velocities [49]. It turns out that this effect can also be associated with nonlinear electrodynamics, in this case, two dispersion relations lead to two different light cones for the wave vectors. Furthermore, from the QED predictions, the dispersion process of real photons from virtual photons causes a change in the polarization that depends on the phase velocity of the interacting photons, in this way birefringence in vacuum arises. Experimental observations are possible with intense laser beams [50]. The effects of nonlinear vacuum electrodynamics on the polarization plane of light have been explored in [51]. The constraints imposed to have a well-posed initial value problem in nonlinear electromagnetic theories coupled to gravity were explored in [52].

Moreover, at strengths approaching the critical electromagnetic fields, self-field interactions induce modifications in light trajectories that can be modeled as light propagating through a curved spacetime. Deviations from the trajectories in vacuum are described in NLED by the null trajectories of an effective metric (also known as the optical metric) that is derived from the analysis of the propagation of electromagnetic field discontinuities [53]–[55].

NLED can describe phenomena such as a change in the phase velocity of light in vacuum, due to the strong external background fields, and photon-photon scattering. In this thesis, we focus on the above-mentioned NLED theories, EH, BI, and ModMax, and analyze the modifications in the propagation of light in the presence of intense EM fields. For the BI NLED, we also consider an accelerated observer and compare the redshift description of two light pulses, using NLED and Maxwell electrodynamics.

Another application of the NLED theories is to consider charged black holes, and study light trajectories in their vicinity. This is, there are BH solutions to the coupled Einstein-NLED equations. Light trajectories are the null geodesics of an optical metric in the BH background. Then we compare these behaviors with the ones for the Einstein-

Maxwell solution, the Reissner-Nordstrom BH.

1.4 Overview

In Chapter 2 we set the basics of the nonlinear theories and review the concept of dispersive media and birefringence. Then, we introduce the tools for the analysis of light propagation in nonlinear electrodynamics; we determine the effective optical metric methodology and with the dispersion relations, we set up the formalism to determine the phase velocity of light in the presence of very intense electromagnetic fields.

Chapter 3 is devoted to the study of light propagation in an Euler-Heisenberg background. In Sections 3.1-3.3 are presented the field equations derived from the Euler-Kockel Lagrangian; then using the effective metric approach we determine the two effective metrics, whose null geodesics are the light trajectories, determining then the corresponding phase velocities, the polarizations, and the dispersion relations; this is done for both a uniform magnetic and a uniform electric background. In section 3.4, by performing a Lorentz boost, we model a moving medium and determine the effects in the phase velocities of the moving medium. These results are published in "Euler-Heisenberg waves propagating in a magnetic background", E. Guzman-Herrera, N. Breton, Eur. Phys. J. C **81**, 115 (2021).

In Chapter 4 we analyze light propagation in a background governed by a BI NLED for an accelerated observer. In section 4.1 we present the effective optical metric, whose null geodesics are the light trajectories, as well as the phase velocity for a BI electromagnetic background. In Section 4.2 are introduced the Rindler spacetime and the coordinate transformation that connects the Minkowski metric with the accelerated frame. In Section 4.3 the phase velocity of light propagating through a purely magnetic BI background from the point of view of the accelerated observer (uniform gravitational field) is derived. In Section 4.4 the phase velocity of light propagating in a purely electric BI background from the point of view of the Rindler observer is determined. In both cases, we consider light that propagates parallel and perpendicular to the accelerated frame. Section 4.5 is devoted to determining the redshift of the propagating light, and how the presence of the BI electromagnetic field affects the frequency shift. These results are published in "Light Propagating in a Born-Infeld background as seen by an accelerated observer", E. Guzman-Herrera, N. Breton, Annalen Der Physik, **534**, 2200043 (2022).

In Chapter 5 we address light behavior in the vicinity of a ModMax black hole. In section 5.1 it is introduced the ModMax NLED Lagrangian. In section 5.2 we set up the basics of the static spherically symmetric ModMax-Einstein BH as the background metric. In section 5.2.1, using the effective metric we analyze the birefringence in the dyonic ModMax BH. In section 5.2.2 we compare the light orbits of the two effective

metrics of the ModMax BH with the massless trajectories in the Reissner Nordstrom (RN) BH. The deflection angles and the gravitational lensing are calculated in section 5.2.3. In section 5.2.5 the redshifts produced by the two effective metrics are determined, first considering an emitter moving in a circular orbit and then a static emitter. In section 5.2.7 the shadow of the ModMax BH is calculated and we set the bounds on the values of the nonlinear parameter γ consistent with the observations of the shadow of the BH at the center of our galaxy, Sagittarius A^*. We compare the effects mentioned above in the ModMax BH vicinity with the corresponding ones of the RN BH, its linear counterpart. The content of this chapter is published in "Light propagation in the vicinity of the ModMax black hole", E. Guzman-Herrera, N. Breton, Journal of Cosmology and Astroparticle Physics, JCAP, **01**, 041 (2024).

In Chapter 6 we compare the phase velocities for light pulses in the presence of EH, BI, and ModMax fields, following the methods of the previous chapters an observer in uniform motion and accelerated are considered. In Section 6.2 we consider the NLEDs coupled to Einstein BH solutions and compare the radii of the shadow of the EH, BI, and ModMax BHs with the one of the RN BH.

We use the Mathematica package "EDCRGTCcode" for the calculations with tensors. We use natural units, $\hbar = 1$, $G = 1$, $c = 1$, and for the EH and BI chapters we use the signature $(+,-,-,-)$ of the metric. For the ModMax chapter, dealing with the black hole case, we use the signature of the metric $(-,+,+,+)$.

We use indistinct light ray, light pulse, light wave and also photons, however, we focus on classical trajectories the more accurate concept would be light ray.

Chapter 2

Basics of Nonlinear Electrodynamics

At a macroscopic level and even at an atomic level, the linear superposition of electromagnetic fields is confirmed experimentally with a precision of less than 1%. Nonetheless, at a subatomic level, there are deviations from the linear superposition and the Maxwell electromagnetic theory presents singularities due to the proximity between charged particles and the high intensity of their fields.

In the presence of intense electromagnetic fields (EM), quantum electrodynamics (QED) predicts that vacuum has properties of a material medium as a consequence of self-field interactions. Nonlinear electromagnetic (NLEM) theories describe self-field effects, for example, light-light interaction or pair production in vacuum excited by an electric field. These effects become significant when the electromagnetic field strengths approach the critical fields $E_{cr} \approx m_e^2 c^3/(e\hbar) \approx 10^{18}$ Volt/m or $B_{cr} \approx 10^9$ Tesla; B_{cr} represents the field at which the cyclotron energy equals $m_e c^2$, where m_e is the mass of the electron, and it defines the field scale at which the external field on quantum processes becomes significant, it is also known as Schwinger critical field and is used to estimate where the nonlinear QED scale begins [20].

The NLEM interactions can be described in a classical way by means of an effective Lagrangian that depends nonlinearly on the two Lorentz and gauge invariants, F and G, of the Faraday tensor $F_{\mu\lambda} = \partial_\mu A_\lambda - \partial_\lambda A_\mu$,

$$F = F^{\mu\lambda}F_{\mu\lambda} = 2(B^2 - E^2), \quad G = F^{*\mu\lambda}F_{\mu\lambda} = -4\vec{B}\cdot\vec{E}, \tag{2.0.1}$$

where $F^{*\mu\lambda} = \frac{1}{2}\epsilon^{\mu\lambda\alpha\beta}F_{\alpha\beta}$ Maxwell's electrodynamics cannot describe nonlinear interactions between two electromagnetic waves, for example, the interaction light-by-light, these phenomena are well known in QED, and considering a classical nonlinear electro-

dynamics (NLED) it is possible to describe them [56]. Several NLED proposals exist to describe such nonlinear effects, but two of them stand out: the Euler–Heisenberg (EH) and the Born-Infeld (BI) theories.

The EH theory was derived from QED principles by W. Heisenberg and H. Euler in 1936 [18]. EH theory has been studied from the perspective of QED in [56]–[58], it considers vacuum polarization to one loop and is valid for electromagnetic fields that change slowly compared to the inverse of the electron mass. By treating the vacuum as a medium, EH effective action predicts rates of nonlinear light interaction processes.

M. Born and L. Infeld, in 1934, developed another relevant NLED theory. Born and Infeld [17] presented a theory with nonlinear corrections to Maxwell electrodynamics from a classical perspective. To solve the singularity of the field and energy of a point charge at its position, they propose the existence of a maximum attainable electromagnetic field, given by the BI parameter b, with a magnitude $b = e/r_0^2 = 10^{20}$ V m^{-1}, where r_0 is the classical electron radius. The interpretation of this absolute field is also that the classical self-energy of the electron is equal to its mass-energy at rest [22]. This classical theory effectively models vacuum polarization as a material medium, in this sense resembling EH theory.

From the perspective of QED, the modifications of BI theory result in a change in the signal of photon-photon scattering, this is the reason why it has been proposed that experiments that measure the QED process could bound the value of the maximum field b of the BI theory [36]. Another interesting feature is that it presents neither birefringence nor shock waves. The absence of birefringence leads to the idea that vacuum birefringence experiments could set bounds on the BI parameter b [36], [59], [60].

It is well known that the BI NLED is not conformally invariant while the EH NLED is neither conformal invariant nor dual invariant. The question arose if any NLED fulfills the same symmetries as Maxwell's, this is, conformal invariance and electric-magnetic duality invariance. The answer is yes.

In [61] was derived a NLED theory endowed with the two symmetries; it is characterized by a dimensionless parameter γ and it reduces to Maxwell theory if $\gamma = 0$. This theory, known as Modified Maxwell (ModMax) NLED, has stimulated research in several aspects, from classical solutions [62], [63] to supersymmetric analysis [64]–[71].

2.1 Effective Optical Metric

It is well known that intense EM fields, where the Maxwell theory is no longer valid, can resemble a curved spacetime, in the sense that light trajectories are not straight lines but undergo deflection. Deviations from the straight trajectories in vacuum are described in NLED by the null trajectories of an effective or optical metric.

The concept of effective metric in nonlinear electrodynamics has its origin in the works by G. Boillat [72], Bialynicki-Birula [41], Plebański [54] and more recently by Novello [53]. In this thesis, we take the approach developed by Plebański and later on by Novello and collaborators. It is derived using the Hadamard theory of the propagation of discontinuities or perturbations of the EM field [54], [53], [55]; i. e. it is assumed that the EM fields of the propagating wave are much smaller than the background fields. The effective optical metric approach is equivalent to the soft photon approximation. Splitting the total electromagnetic field into a background field $F_{\mu\nu}$ and a propagating photon $f_{\mu\nu}$, and keeping the linear approximation with respect to $f_{\mu\nu}$ in the equations of motion, leads to an eigenvalue equation for the propagating modes [42], [73].

Considering a null vector $k_\mu = (\omega, \vec{k})$ that is normal to the characteristic surfaces or wavefronts the effective metric $g_{\text{eff}}^{\mu\nu}$ must be the metric in which the wave vector is null, $k^\mu k_\mu = 0$,

$$g_{\text{eff}}^{(i)\mu\nu} k_\mu k_\nu = 0, \quad i = 1, 2, \tag{2.1.1}$$

the (i) superscript corresponds to the two metrics that can arise in NLED when birefringence occurs. The equations of the propagation of the field discontinuities in nonlinear electrodynamics characterized by a Lagrangian $\mathcal{L}(F, G)$ are derived by analyzing the propagation of linear waves associated with the discontinuity of the field $f_{\alpha\beta}$, in the limit of geometrical optics [55]. From the pair of coupled equations

$$\zeta k^2 = \frac{4}{L_F} F^{\lambda\nu} F^{\mu}{}_{\lambda} k_\nu k_\mu (L_{FF}\zeta + L_{FG}\zeta^*) - \frac{G}{L_F} k^2 (L_{FG}\zeta + L_{GG}\zeta^*) \tag{2.1.2}$$

$$\zeta^* k^2 = \frac{4}{L_F} F^{\lambda\nu} F^{\mu}{}_{\lambda} k_\nu k_\mu (L_{FG}\zeta + L_{GG}\zeta^*) - \frac{G}{L_F} k^2 (L_{FF}\zeta + L_{FG}\zeta^*) + 2\frac{F}{L_F} k^2 (L_{FG}\zeta + L_{GG}\zeta^*), \tag{2.1.3}$$

where, $\zeta = F^{\alpha\beta} f_{\alpha\beta}$, $\zeta^* = F^{*\alpha\beta} f_{\alpha\beta}$ y $k^2 = g^{\mu\nu} k_\mu k_\nu$. Eqs. 2.1.2 and 2.1.3 were also presented in [53]. Considering $k^2 \neq 0$ i.e. in the background spacetime, k^μ is not null, the relation between ζ and ζ^* is obtained as $\Omega_1 \zeta^{*2} + \Omega_2 \zeta\zeta^* + \Omega_3 \zeta^2 = 0$ with

$$\begin{aligned}
\Omega_1 &= -L_{FG} + 2\frac{F}{L_F} L_{FG} L_{GG} - \frac{G}{L_F} L_{FG}^2 + \frac{G}{L_F} L_{GG}^2 \\
\Omega_2 &= L_{GG} - L_{FF} + 2\frac{F}{L_F} L_{FF} L_{GG} + 2\frac{F}{L_F} L_{FG}^2 - 2\frac{G}{L_F} L_{FF} L_{FG} + 2\frac{G}{L_F} L_{FG} L_{GG} \\
\Omega_3 &= L_{FG} + 2\frac{F}{L_F} L_{FF} L_{FG} - \frac{G}{L_F} L_{FF}^2 + \frac{G}{L_F} L_{FG}^2,
\end{aligned}$$

and

$$\Omega_{(a)} = \frac{-\Omega_2 \pm \sqrt{\Omega_2^2 - 4\Omega_1\Omega_3}}{2\Omega_1}, \qquad a = \mp \tag{2.1.4}$$

this leads to two possible paths of propagation which indicates the possibility of birefringence as we can relate the each paths to a given polarization mode, then

$$k_{(a)}^2 = 4\frac{L_{FF} + \Omega_{(a)} L_{FG}}{L_F + G\left(L_{FG} + \Omega_{(a)} L_{GG}\right)} F^{\lambda\mu} F_\lambda^\nu k_\mu k_\nu. \tag{2.1.5}$$

NLED can be modeled as a material medium characterized by indices of birefringence or refractive indices [55], [61], λ_a, given in terms of the NLED Lagrangian and its derivatives by,

$$\lambda_a = -4\frac{L_{FF} + \Omega_{(a)} L_{FG}}{L_F + G(L_{FG} + \Omega_{(a)} L_{GG})}, \tag{2.1.6}$$

where $L_X = \frac{dL}{dX}$, $X = F, G$, and $\Omega_{(a)}$ in Eq. (2.1.4), depends on the derivatives of the Lagrangian with respect to the invariants [55]. The expression for the effective metric can be identified from the dispersion relation, Eq. (2.1.1),

$$\left\{g^{\mu\nu} + \lambda_a t^{\mu\nu}\right\} k_\mu k_\nu = g_{\text{eff}(a)}^{\mu\nu} k_\mu k_\nu = 0, \tag{2.1.7}$$

where $t^{\mu\nu} = F^{\mu\lambda} F_\lambda{}^\nu$ and $g^{\mu\nu}$ is the background metric that can be the Minkowski metric or a general curved spacetime, for instance, a black hole or a cosmological spacetime. And the effective metrics for general nonlinear electrodynamics with Lagrangian $L(F, G)$ are given by,

$$g_{\text{eff}(a)}^{\mu\nu} = g^{\mu\nu} - 4\frac{L_{FF} + \Omega_{(a)} L_{FG}}{L_F + G(L_{FG} + \Omega_{(a)} L_{GG})} t^{\mu\nu}. \tag{2.1.8}$$

If the Lagrangian is such that $\mathcal{L}_{FG} = 0$, from Eqs. 2.1.2 and 2.1.3 the effective metrics become

$$g_{\text{eff}(1)}^{\mu\nu} = \left(L_F - 2L_{GG}F\right) g^{\mu\nu} - 4L_{GG} t^{\mu\nu}, \tag{2.1.9}$$

$$g_{\text{eff}(2)}^{\mu\nu} = L_F g^{\mu\nu} - 4L_{FF} t^{\mu\nu}, \tag{2.1.10}$$

Additionally when we turn off either the electric or the magnetic field, i.e., $\vec{E} = 0$ or $\vec{B} = 0$, then $G = 4\vec{E} \cdot \vec{B} = 0$, and the effective metrics become

$$g_{\text{eff}(1)}^{\mu\nu} = L_F g^{\mu\nu}, \tag{2.1.11}$$

$$g_{\text{eff}(2)}^{\mu\nu} = L_F g^{\mu\nu} - 4L_{FF} t^{\mu\nu}, \tag{2.1.12}$$

where we note that the effective metric $g_{\text{eff}(1)}$ is conformal to the background metric; in this case, one of the optical paths is the null geodesic of the background metric and the other one is the null geodesic of the effective metric $g_{\text{eff}(2)}$.

In the Maxwell case $L = -F/4, \quad L_F = -1/4, \quad L_{FF} = 0$ and $L_G = 0$, then both effective metrics become conformal to the background metric, $g_{\rm eff}^{(1)\mu\nu} = g_{\rm eff}^{(2)\mu\nu} = g^{\mu\nu}$, and the null geodesics coincide with the light trajectories in the background spacetime.

See [49] for a study on the Fresnel equation in nonlinear electrodynamics and [74] for a classification of the effective metrics.

2.2 Light propagation in the effective metric

The phase velocity of light can be calculated from the dispersion relation. Let us consider a null vector $k_\mu = \{\omega, \vec{k}\}$. If k_i is the light propagation direction, from the dispersion relation, Eq. (2.1.1),

$$g^{tt}_{{\rm eff}(a)}\omega^2 + 2g^{it}_{{\rm eff}(a)}\omega k_i + g^{ij}_{{\rm eff}(a)}k_i k_j = 0, \tag{2.2.1}$$

where i, j subscripts (or superscripts) denote the spatial coordinates and t denotes the time coordinate. Defining the normalized wave vector $\tilde{k}_i = k_i/|\vec{k}|$, then Eq. (2.2.1) can be written as

$$g^{tt}_{{\rm eff}(a)}\frac{\omega^2}{|\vec{k}|^2} + 2g^{it}_{{\rm eff}(a)}\frac{\omega}{|\vec{k}|}\tilde{k}_i + g^{ij}_{{\rm eff}(a)}\tilde{k}_i\tilde{k}_j = 0. \tag{2.2.2}$$

Then the light's phase velocity, $v = \omega/|\vec{k}|$, for propagation in the direction $\tilde{k}_i$, v^i is given by

$$\left(v^i\right)_a = \frac{\omega}{|\vec{k}|}\tilde{k}_i = \frac{g^{it}_{{\rm eff}(a)}\tilde{k}_i}{g^{tt}_{{\rm eff}(a)}} \pm \sqrt{\left(\frac{g^{it}_{{\rm eff}(a)}\tilde{k}_i}{g^{tt}_{{\rm eff}(a)}}\right)^2 - \frac{g^{ij}_{{\rm eff}(a)}\tilde{k}_i\tilde{k}_j}{g^{tt}_{{\rm eff}(a)}}}, \qquad a = 1, 2 \tag{2.2.3}$$

in the case that the effective metric is diagonal, i.e. $g_{ti} = 0$ and $g_{ij} = 0, \quad i \neq j$, Eq. (2.2.3) simplifies to $\left(v^i\right)_a = \pm\sqrt{-\frac{g^{ij}_{{\rm eff}(a)}\tilde{k}_i\tilde{k}_j}{g^{tt}_{{\rm eff}(a)}}}$.

The two possible effective metrics $g^{\mu\nu}_{{\rm eff}(a)}$, $a = 1, 2$, render two dispersion relations that correspond to two modes of polarization, this is known as the birefringence effect [53]. Note that these velocities differ from the phase velocities of a massless test particle that follows the null geodesics of the background metric $g_{\mu\nu}$; they are given by analogous expressions making $g^{\mu\nu}_{\rm eff(a)} \mapsto g^{\mu\nu}$, then

$$v^i_{\rm massless} = \pm\sqrt{-\frac{g^{ij}\tilde{k}_i\tilde{k}_j}{g^{tt}}}. \tag{2.2.4}$$

Chapter 3

Light propagation in Euler-Heisenberg theory

Taking into account vacuum polarization to one loop, by treating the vacuum as a medium and restricting to electromagnetic fields that change slowly compared to the inverse electron mass, the Euler-Heisenberg (EH) effective action predicts nonlinear light interaction processes. The EH Lagrangian $\mathcal{L}_{\rm EH}(F,G)$ depends in nonlinear way on the two Lorentz and gauge invariants of the Faraday tensor $F_{\mu\lambda}$, $F = F^{\mu\lambda}F_{\mu\lambda} = 2(B^2 - E^2)$ and $G = F^{*\mu\lambda}F_{\mu\lambda} = -4\vec{B}\cdot\vec{E}$, with the dual field $F^{*\mu\lambda} = \frac{1}{2}\epsilon^{\mu\lambda\alpha\beta}F_{\alpha\beta}$,

$$L_{\rm EH}(F,G) = -\frac{F}{4} - \frac{1}{8\pi^2}\int_0^\infty e^{-m^2 s}\left[(es)^2\frac{{\rm Re}[\cosh(es\sqrt{2(F+iG)})]}{{\rm Im}[\cosh(es\sqrt{2(F+iG)})]} - \frac{2}{3}(es)^2F - 1\right]\frac{ds}{s^3}. \tag{3.0.1}$$

From this Lagrangian new nonlinear interactions can be derived, that do not occur in the tree-level Maxwell action; among them are light-light interaction and pair production in vacuum excited by an external electromagnetic field. It has been thoroughly investigated, and higher loop contributions in strong fields have been calculated as well, see for instance [75], [76].

The Lagrangian (3.0.1) can be expanded as an asymptotic series [77], [40] whose first terms of the order α^2, are

$$L_{\rm EK}(F,G) = -\frac{F}{4} + \frac{\mu}{4}\left(F^2 + \frac{7}{4}G^2\right), \tag{3.0.2}$$

where μ is the parameter of the EH theory that in terms of the fine structure constant,

α ($c = 1, \quad h = 1$), is

$$\mu = \frac{2\alpha^2}{45 m_e^4}; \tag{3.0.3}$$

that in terms of the critical fields, is of the order $\mu \sim \alpha/B_{cr}^2$. Actually (3.0.2) is the Euler-Kockel (EK) Lagrangian, also known as the weak field limit of the EH Lagrangian. H. Euler and B. Kockel, two of Heisenberg's students, investigated QED vacuum polarizations in the constant background limit, obtaining the leading nonlinear correction in powers of the field strengths, presenting the Lagrangian (3.0.2) in 1935 [19]. To describe the propagation of photons in an external field in QED only this first correction is needed, i.e. the terms of the order α^2, $\alpha^2(F^2 + 7G^2/4)/(90 m_e^4)$. The use of the first terms in this expansion is justified if the dimensionless expansion parameter $4\pi\alpha\hbar^3|F|^2/(m_e^4 c^5)$ is much smaller than unity [41]. This is indeed the case even for strong magnetic fields, for instance, the magnetic fields in neutron stars that may be as large as 10^{12} Gauss [78], where processes like photon splitting and pair conversion are expected to occur in the vicinity of neutron stars [38].

The phase velocity of an electromagnetic wave traveling through intense EM fields will be altered due to vacuum polarization. It is also well known the emergence of a longitudinal field component, as well as the decrease of the phase velocity [77], [79], [41]. Another effect that arises in strong electromagnetic backgrounds is the birefringence [80]. To detect nonlinear electromagnetic effects it is crucial to determine the velocity of propagation of the electromagnetic wave in the intense EM background, and this chapter aims to determine the phase velocities that correspond to the birefringence as well as the electric field longitudinal component in terms of the magnetic background derived from the Euler-Kockel Lagrangian. Although these effects have been the subject of many studies, we approach them in terms of the effective metrics derived in nonlinear electrodynamics for curved spaces.

3.1 The Euler-Heisenberg propagating wave

In this section, we study the propagation of light in a background of intense electric and magnetic uniform fields. We start by presenting the electromagnetic field equations derived from the EK Lagrangian (3.0.2), that are,

$$F_{\lambda\mu;\nu} + F_{\nu\lambda;\mu} + F_{\mu\nu;\lambda} = 0; \qquad \partial_\nu \left[\sqrt{-g}\,(L_{\rm F} F^{\mu\nu} + L_{\rm G} F^{*\mu\nu})\right] = 0, \tag{3.1.1}$$

where $L_{\rm X}$ denotes the derivative of L with respect to the invariant X, dL/dX.

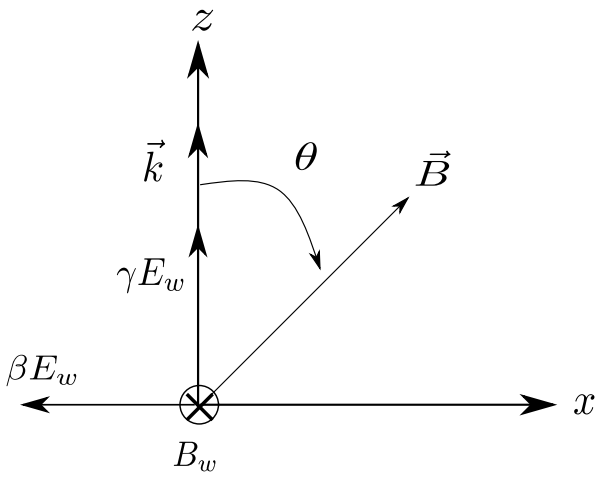

Figure 3.1: Plane wave electromagnetic fields with the electric component $\gamma E_w(\xi)$ arising in the $\hat{z}$ direction, due to the nonlinear interaction. The uniform magnetic field background $\vec{B}$ is shown making a θ angle with the z-axis. The magnitudes of the fields are not on scale. The subscript w refer to the electromagnetic wave with potential a_μ.

Due to the interaction between the wave and the background, it is known that the parallel mode of the propagating wave fails to be orthogonal to the wave vector $\vec{k}$ [80], because a longitudinal wave component arises in the presence of strong magnetic fields.

We shall consider an electromagnetic (EM) wave propagating through a uniform magnetic background. The wave fields are a function of $\xi = (z - vt)$, where v is the phase velocity of the propagation in the $\hat{z}$ direction; the electric and magnetic fields of the propagating wave in terms of the electromagnetic potential a^μ are proposed as

$$a_\mu(\xi) = (0, a(\xi), 0, -\gamma a(\xi)/v). \tag{3.1.2}$$

We consider the arising electric component to be $\gamma a(\xi)$, and the constant γ is to be determined by solving the nonlinear electrodynamics (NLED) field Eqs. (3.1.1). The propagating vector $\vec{k}$ is along the z-direction, $k^\mu = (\omega, 0, 0, k)$, the wave electric field is along the $-x$-direction, and the wave magnetic field is along the y-direction. For the uniform background A^μ

$$A_\mu(\xi) = (0, 0, B_x z - B_z x, B_y x). \tag{3.1.3}$$

In Fig. 3.1 shows the plane wave propagating in the magnetic background; for convenience, we locate the magnetic background in the plane XZ, $\vec{B} = B\sin\theta\hat{x} + B\cos\theta\hat{z} = B_x\hat{x} + B_z\hat{z}$, and $B_y = 0$.

The photon polarization tensor in a homogeneous electromagnetic background in the context of QED has been addressed in [81], and in [44] was studied the case of a

Born-Infeld wave in a magnetic background. In the next subsection, we determine the phase velocities v_i, $i = 1, 2$, and γ in the effective metric approach. for the EH magnetic background.

3.2 Effective metric and phase velocities of light rays

In the case of the EK Lagrangian, $L_{FG} = 0$, and the effective metrics are given by Eqs. (2.1.9) and (2.1.10). With the considerations for the electromagnetic field, the nonvanishing electromagnetic tensor components of the magnetic background are $F^{xy} = -B_z, \quad F^{xz} = B_y = 0, \quad F^{yz} = -B_x$, and $F = 2B^2$, the corresponding phase velocities v_i derived from the two effective metrics (2.1.9) and (2.1.10), through Eq. (2.2.3) are, to the first order in μ

$$(v_1)^2 = 1 - \frac{14\mu B_x^2}{1 + 10\mu B^2}, \tag{3.2.1}$$

$$(v_2)^2 = 1 - \frac{8\mu B_x^2}{1 - 4\mu B^2}. \tag{3.2.2}$$

The effective metric approach turns out to be equivalent to a soft photon approximation. Splitting the total electromagnetic field into the background field $\vec{B}$ and the propagating photon $f_{\mu\nu}$,

$$f_{\mu\nu} = \partial_\mu a_\nu - \partial_\nu a_\mu = (\epsilon_\mu k_\nu - \epsilon_\nu k_\mu) e^{-ikx}, \tag{3.2.3}$$

with the vector potential $a^\mu(k)$, the polarization $\epsilon_\mu = a_\mu / \sqrt{a^\alpha a_\alpha}$, the wave vector $k^\mu = (\omega, 0, 0, k)$, and being the phase $kx = k^\alpha x_\alpha = -k\xi$. Keeping the linear approximation with respect to $f_{\mu\nu}$ in the equations of motion leads to an eigenvalue equation for the propagating modes [73], [42]

$$A^{\mu\nu}\epsilon_\nu = 0 \tag{3.2.4}$$

where $A^{\mu\nu}$ is given by

$$A^{\mu\nu} = c_1 F^{\mu\alpha} F^{\nu\beta} k_\alpha k_\beta + c_2 F^{*\mu\alpha} F^{*\nu\beta} k_\alpha k_\beta + c_3(\delta^{\mu\nu}\kappa^2 - k^\mu k^\nu), \tag{3.2.5}$$

$$c_1 = \frac{1}{2}\mathcal{L}_{FF}, \quad c_2 = \frac{1}{2}\mathcal{L}_{GG}, \quad c_3 = \frac{1}{2}\mathcal{L}_F, \tag{3.2.6}$$

where $\kappa = k^\alpha k_\alpha = \omega^2 - k^2, \quad k^\mu = (\omega, 0, 0, k)$. Eq. (3.2.4) is the light cone condition and its solutions are the dynamically allowed polarization modes. Moreover, adopting the temporal gauge $\epsilon_0 = 0$, then Eq. (3.2.4) splits into

$$A^{0i}\epsilon_0 = 0, \quad A^{ij}\epsilon_j = 0. \tag{3.2.7}$$

For the case under study, the nonvanishing electromagnetic tensor components of the magnetic background are $F^{xy} = -B_z, \quad F^{xz} = B_y = 0, \quad F^{yz} = -B_x$, and their dual $F^{*tx} = -B_x, \quad F^{*ty} = -B_y = 0, \quad F^{*tz} = -B_z$ and $F = 2B^2$. Explicitly Eqs. (3.2.7) become

$$c_2 B_z B_x \epsilon_1 + (c_2 B_z^2 - c_3)\epsilon_3 = 0, \tag{3.2.8}$$

$$[c_2 \omega^2 B_x^2 - c_3(\omega^2 - k^2)]\epsilon_1 + c_2 \omega^2 B_z B_x \epsilon_3 = 0, \tag{3.2.9}$$

$$[c_1 k^2 B_x^2 - c_3(\omega^2 - k^2)]\epsilon_2 = 0, \tag{3.2.10}$$

The Eq. $A^{0i}\epsilon_0 = 0$ turns out to be the same as Eq. (3.2.8). Note that in Eqs. (3.2.8) and (3.2.9) are coupled ϵ_1 and ϵ_3; these Eqs. define the parallel polarization tensor as $\epsilon_\parallel = [0, a(\xi)/ka, 0, -\gamma a(\xi)/(\omega a)]$ or $\epsilon_\parallel = [0, 1, 0, -\gamma/v]$ and determine the arising electric component γ and a first dispersion relation as

$$\gamma = \frac{14\mu B_x B_z}{1 - 4\mu B^2 + 14\mu B_z^2} v_1, \tag{3.2.11}$$

$$\left(\frac{\omega}{k}\right)^2_{(1)} = (v_1)^2 = 1 - \frac{14\mu B_x^2}{1 + 10\mu B^2}. \tag{3.2.12}$$

The angle δ between the polarization $\epsilon_\parallel$ and the propagating vector $\vec{k}$, is

$$\delta = \operatorname{arccot}\left(\frac{\gamma}{v}\right) = \frac{14\mu B_x B_z}{1 - 4\mu B^2 + 14\mu B_z^2}. \tag{3.2.13}$$

While Eq. (3.2.10) does not impose any condition on $\epsilon_2 \neq 0$, then we can set the transversal polarization mode as $\epsilon_\perp = (0, 0, 1, 0)$, and the second dispersion relation is

$$\left(\frac{\omega}{k}\right)^2_{(2)} = (v_2)^2 = 1 - \frac{8\mu B_x^2}{1 - 4\mu B^2}, \tag{3.2.14}$$

where $B^2 = B_x^2 + B_z^2$. Transversal and parallel are defined with respect to the plane spanned by the magnetic field B and the wave number $\vec{k}$, that is the plane XZ. Phase velocities are in agreement with the ones derived from the effective metrics given by (2.1.9) and (2.1.10).

As a consequence of the nonlinear interaction wave-background there is a retarding term in v_i that depends on the background field; specifically the retarding term arises due to the magnetic component that is perpendicular to the propagating direction, $B_x = B_\perp$, in such a way that if $B_\perp = 0$, then the velocity is the one in vacuum.

The phase velocities $v_{\rm i}, \quad i = 1, 2$ of the propagation through the magnetic background, Eqs. (3.2.12), (3.2.14), are illustrated as a function of the dimensionless μB^2 in Fig. 3.2. The truncation we have used to describe the propagation of photons in an external field is indeed valid for strong magnetic fields that may be as large as 10^{12}

Gauss (10^{-1} Tesla), compared to the critic field $B_{\rm cr} \sim 10^9$ Tesla, gives us a range of validity of our variable $\mu B^2 \sim \alpha(B/B_{\rm cr})^2$, and considering that $B/B_{\rm cr} \sim 1/100$, the range of validity is $\mu B^2 \in [0, 10^{-6})$. In agreement with this range, the slowing down of the wave is in the hundreds of thousandths. As shown in Fig. 3.2 it would be very difficult to distinguish in an experiment if birefringence occurs.

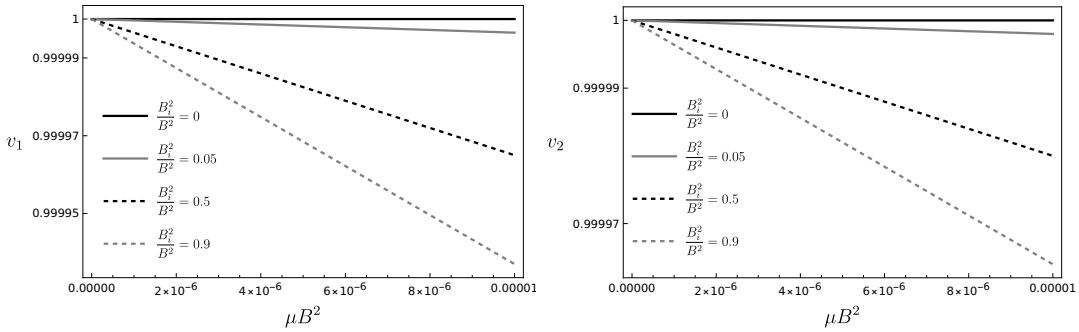

Figure 3.2: The phase velocities v_1, v_2 are shown as a function of the (dimensionless) magnetic background μB^2, for four values of $(B_x/B)^2$. As μB^2 increases $v_{1,2}$ diminish. If $\mu B^2 = 0$ the velocity is the one in vacuum, $v_i = c = 1$. Note that the slowing effect increases as the transversal magnetic component B_x does. The velocity is lower for values $(\frac{B_x}{B})^2 < 0.5$.

If v_2 Eq. (3.2.14) is a real number, a lower bound arises for the magnetic field B, $\mu B^2 \leq 1/4$, that in terms of the critical magnetic field B_{cr} is $\mu B^2 \approx \alpha(B/B_{cr})^2$, since $(B/B_{cr}) \ll 1$ that value is never reached in this approximation. If $\mu = 0$, that means the absence of vacuum polarization, then the light velocity in vacuum, $v = c$, is recovered. In Fig. 3.3 it is illustrated the factor γ of the rising wave electric component in the propagating direction.

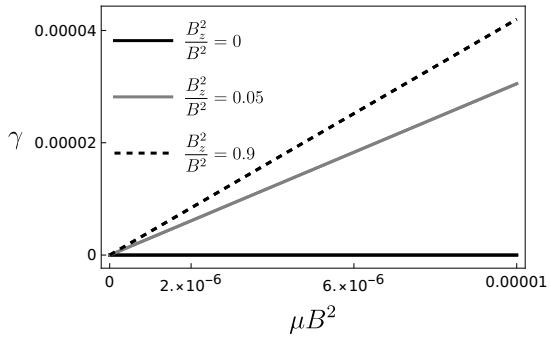

Figure 3.3: It is plotted γ, the arising wave electric component in the propagating direction, as a function of μB^2 for different values of B_z^2/B^2.

3.3 The electric uniform background

In an analogous way to the previous subsection, we now consider an electric background. The propagation of an EM wave through an intense uniform electric field is of interest [77] since there is the prediction of vacuum electron-positron production that has not yet been measured, however, it might be feasible in the near future, due to the high power reached lately by lasers [82], [83].

In this case, the nonvanishing electromagnetic tensor components for the electric background are $F^{tx} = -E_x$, $F^{ty} = -E_y$, $F^{tz} = -E_z$, and their dual $F^{*xy} = E_z$, $F^{*xz} = -E_y = 0$, $F^{*yz} = E_x$, and $F = -2E^2 = -2(E_x^2 + E_z^2)$. The resulting equations from (3.2.7) have the form of Eqs. (3.2.8), (3.2.9),(3.2.10) interchanging $c_1 \leftrightarrow c_2$ and $B_i \leftrightarrow E_i$. Solving them we get the following γ-component and the phase velocities

$$\gamma = \frac{8\mu E_x E_z}{1 + 4\mu E^2 + 8\mu E_z^2} v_1, \tag{3.3.1}$$

$$\left(\frac{\omega}{k}\right)^2_{(1)} = (v_1)^2 = 1 - \frac{14\mu E_x^2}{1 + 4\mu E^2}, \tag{3.3.2}$$

$$\left(\frac{\omega}{k}\right)^2_{(2)} = (v_2)^2 = 1 - \frac{8\mu E_x^2}{1 + 12\mu E^2}. \tag{3.3.3}$$

Phase velocities v_1 and v_2 can be derived as well from Eqs. (2.2.3). v_1 and v_2 are shown in Fig. 3.4; the plots are very similar and in the scale considered there is not much qualitative difference. Analogous observations for the magnetic background apply to the electric case.

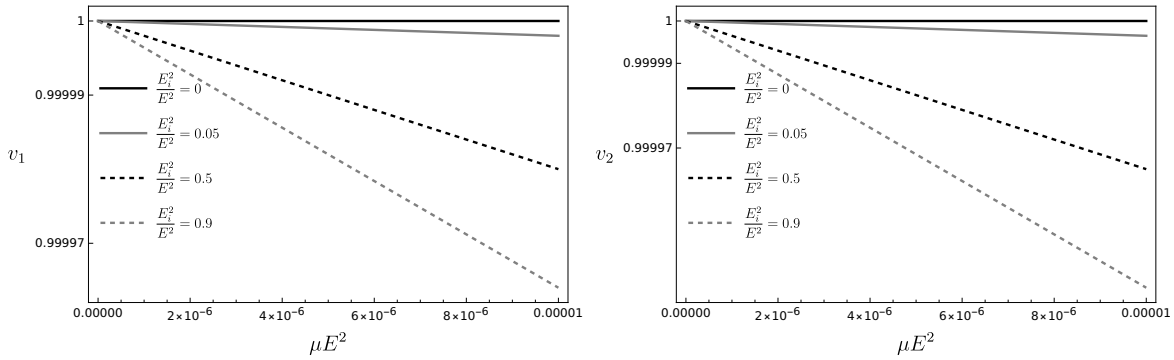

Figure 3.4: The phase velocities v_i versus μE^2 are displayed. Velocities approach the ones in vacuum as $\mu E^2 \mapsto 0$. For the electric uniform background, v_2 reaches lower values than v_2.

3.4 The phase velocity of the electromagnetic wave in a flowing magnetic background

Another interesting situation is when the background is not still but moving with constant velocity; it can be considered as a plasma model, for instance. Any effective metric can be considered as a moving medium, as we show in what follows, as long as the effective metric is nondiagonal. For the case we have studied this means that the metric component g^{eff}_{tz} be nonvanishing. This we achieve by performing a Lorentz transformation on the NLED effective metric.

3.4.1 The effective metric as a Painlevé-Lemaitre-Gullstrand metric

Let us consider a completely general effective metric (nondiagonal); to determine the phase velocity of the EM wave $\beta = v/c$, we calculate the null geodesics of the effective metric by making zero the line element, $ds^2 = g^{\text{eff}}_{\mu\nu} dx^\mu dx^\nu = 0$,

$$\frac{ds^2}{d\tau^2} = g^{\text{eff}}_{\mu\nu} \frac{dx^\mu}{d\tau} \frac{dx^\nu}{d\tau} = g^{\text{eff}}_{\mu\nu} \dot{x^\mu} \dot{x^\nu} = 0. \tag{3.4.1}$$

Considering Cartesian coordinates (t, x, y, z) and a light trajectory for fixed x and y, $(\dot{x} = 0 = \dot{y})$, we obtain from Eq. (3.4.1) a quadratic equation for the phase velocity along the z-direction, $\beta = dz/dt = \dot{z}/\dot{t}$; then solving for $\beta = v/c$ we obtain the phase velocity in terms of the metric components of the effective metric,

$$\beta = \frac{dz}{dt} = -\frac{g^{\text{eff}}_{tz}}{g^{\text{eff}}_{zz}} \pm \frac{\sqrt{(g^{\text{eff}}_{tz})^2 - g^{\text{eff}}_{tt} g^{\text{eff}}_{zz}}}{g^{\text{eff}}_{zz}}. \tag{3.4.2}$$

This expression is in agreement with Eq. (2.2.3). The interpretation of the effective metric as a propagating medium can be seen clearly by writing the effective metric $g^{\text{eff}}_{\mu\nu}$ in the form of the Painlevé-Lemaitre-Gullstrand (PLG) metric, that in Cartesian coordinates $(\tilde{t}, \tilde{x}, \tilde{y}, \tilde{z})$ for $\tilde{x}$ =const $\tilde{y}$ = const, is given by

$$ds^2 = -(\tilde{c}^2 - V^2) d\tilde{t}^2 - 2V d\tilde{z} d\tilde{t} + d\tilde{z}^2, \tag{3.4.3}$$

where $V(\tilde{t}, \tilde{z})$ represents the velocity of the propagating medium and $\tilde{c}(\tilde{t}, \tilde{z})$ the velocity of the perturbation propagating through such a medium [84]. Taking advantage of the constant curvature (scalar curvature is zero $R = 0$) of the effective metric, by making a scale transformation on the (t, z) coordinates we can write the effective metric Eq.

(3.4.1) in the PLG form (3.4.3). By re-scaling as

$$t \mapsto \frac{\sqrt{V^2-\beta^2}}{\sqrt{g_{tt}}}\tilde{t}, \quad z \mapsto \frac{1}{\sqrt{g_{zz}}}\tilde{z}, \tag{3.4.4}$$

the effective metric in the $(\tilde{t},\tilde{z})$ coordinates acquires the form,

$$d\tilde{s}^2 = -\left(\beta^2 - V^2\right)d\tilde{t}^2 + 2g_{tz}^{\text{eff}}\frac{\sqrt{V^2-\beta^2}}{g_{tt}^{\text{eff}}g_{zz}^{\text{eff}}}d\tilde{z}d\tilde{t} + d\tilde{z}^2, \tag{3.4.5}$$

comparing with (3.4.3), we identify the velocity of the perturbation as $\tilde{c}=\beta$ and we determine the velocity of the medium V as

$$V = \pm\frac{-g_{tz}^{\text{eff}}\beta}{\sqrt{(g_{tz}^{\text{eff}})^2 - g_{tt}^{\text{eff}}g_{zz}^{\text{eff}}}}. \tag{3.4.6}$$

Note that if $g_{tz}^{\text{eff}}=0$ then $V=0$, i.e. the medium is static. By performing a Lorentz boost of velocity β_L in the $z-$direction Λ_z, on the effective metric, $\Lambda_z g_{\text{eff}}\Lambda_z^T = g'_{\text{eff}}$, we obtain a nondiagonal metric, that we denote with a prime $g'^{\text{eff}}_{\mu\nu}$. The effect of the Lorentz transformation is of mixing the components of the effective metric, in such a way that if the effective metric is diagonal, the transformed one has nondiagonal components, i.e. g'^{eff}_{tz} does not vanish. The original effective metric (previous to Lorentz transformation) is recovered when $\beta_L=0$. Note as well that the velocity of the medium V is not the same as the one of the Lorentz transformation β_L. The relationship between V and β_L is given implicitly in Eq. (3.4.6), with $g^{\text{eff}}_{\mu\nu}\mapsto g'^{\text{eff}}_{\mu\nu}$.

3.4.2 The magnetic background Lorentz boosted

In this subsection, we show how the phase velocity is affected when a Lorentz boost is performed on the magnetic background.

Making a Lorentz transformation along the z-direction changes the magnetic background and an electric component field arises: such that now the nonvanishing electromagnetic tensor components of the magnetic background are $F^{ty}=-\gamma_L\beta_L B_x$, $F^{xy}=-B_z$, $F^{xz}=B_y=0$, $F^{yz}=-\gamma_L B_x$, and $F=2B^2$.

Calculating the phase velocities using the effective metrics in Eqs. (2.1.9) and (2.1.10), through Eq. (2.2.3) are

$$v_1^{LTz} = \frac{-14\mu\gamma_L^2 B_x^2\beta_L \pm \sqrt{(1+10\mu B^2)(1+10\mu B^2-14\mu B_x^2)}}{1+10\mu B^2+14\mu\gamma_L^2\beta_L^2 B_x^2}, \tag{3.4.7}$$

$$v_2^{LTz} = \frac{-8\mu\gamma_L^2 B_x^2\beta_L \pm \sqrt{(1-4\mu B^2)(1-4\mu B^2+8\mu B_x^2)}}{1-4\mu B^2+8\mu\beta_L^2\gamma_L^2 B_x^2} \tag{3.4.8}$$

where we are denoting β_L as the velocity of the Lorentz transformation along z and $\gamma_L^2 = (1-\beta_L^2)^{-2}$. Although the factor $\gamma_L > 1$ enhances the retarding term, the denominator increases as well, in such a way that the effect of retarding does not increase much with the Lorentz transformation along the z-direction.

Let us now perform a Lorentz boost in the direction perpendicular to the propagation of the wave. By transforming the background with a Lorentz boost in the x-direction, the magnetic background results as $F^{ty} = \gamma_L \beta_L B_z, \quad F^{xy} = -\gamma_L B_z, \quad F^{xz} = B_y = 0, \quad F^{yz} = -B_x,$; in such a way that the phase velocities using the effective metrics in Eqs. (2.1.9) and (2.1.10), through Eqs. (2.2.3) are

$$v_1^{LTx} = \frac{14\mu\gamma_L\beta_L B_x B_z \pm \sqrt{(1+10\mu B^2)(1-4\mu B_x^2 + B_z^2(-4+14\gamma_L^2)\mu)}}{1+10\mu B^2 + 14\mu\gamma_L^2\beta_L^2 B_z^2}, \tag{3.4.9}$$

$$v_2^{LTx} = \frac{8\mu\gamma_L\beta_L B_x B_z \pm \sqrt{(1-4\mu B^2)(1-8\mu B_x^2\gamma_L^2 + 4B^2(-3+2\gamma_L^2)\mu)}}{1-4\mu B^2 + 8\mu B_z^2\beta_L^2\gamma_L^2}, \tag{3.4.10}$$

where we are denoting β_L as the velocity of the Lorentz transformation along x-direction and $\gamma_L^2 = (1-\beta_L^2)^{-2}$.

In Fig. 3.5 are illustrated the velocities for metric 1 in three cases, v_1 corresponding to the metric Eq. (2.1.9) and then the ones with the Lorentz boost along the z and x directions considering the phase velocities up to $\mathcal{O}(\mu^2 B^4)$

$$v_1^{LTz} = 1 - 14\mu B_x^2\left(1 - \frac{1-3\beta_L}{2(1-\beta_L)}\right) + \mathcal{O}(\mu^2 B^4) \tag{3.4.11}$$

$$v_1^{LTx} = 1 - 7B_x^2\mu\left(1 - \beta_L\gamma_L\frac{B_z}{B_x}\left(2 - \frac{\beta_L B_z\gamma_L}{B_x}\right)\right) + \mathcal{O}(\mu^2 B^4) \tag{3.4.12}$$

The direction of the Lorentz velocity is important: when β_L is in the same direction as the propagation, the braking of the wave is more effective than if β_L is perpendicular to the propagation. In the former case, the wave slows down with a magnetic background less intense than for a still medium.

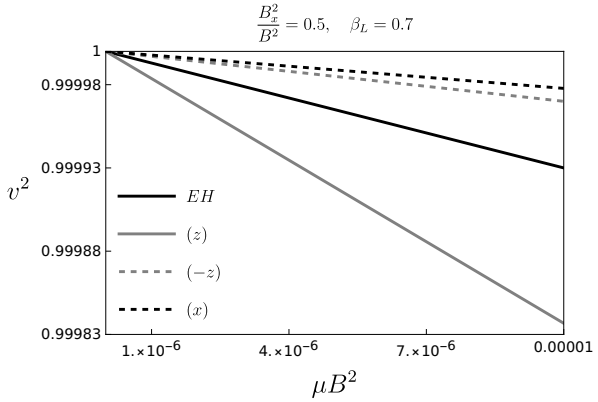

Figure 3.5: The phase velocities for metric 1 are shown in three cases: v_1 for the metric Eq. (2.1.9) (black) and then the corresponding to the Lorentz boost along the z (grey) and x (blue) directions. The slowing down is enhanced if the boost is along the propagation direction.

The modeling of a moving medium deserves further study, specifically the precise relationship between the medium effects and the velocity of the Lorentz transformation. For the case of the electric background we guess has a similar behavior to the magnetic one when Lorentz boosted.

3.5 Conclusions

In this chapter, we have analyzed the slowing down of an electromagnetic wave under the effect of very intense electromagnetic Euler-Heisenberg field background, in the context of the Euler-Kockel Lagrangian, that effectively takes into account the vacuum polarization phenomenon. We used the effective metric approach and showed that it is equivalent to the soft photon approximation. We find there is birefringence in both backgrounds, electric and magnetic, and the phase velocities of the propagation depend on its polarization.

The results contained in this chapter have been published in the paper

E. Guzman-Herrera, N. Breton,
"Euler–Heisenberg waves propagating in a magnetic background"
European Physics Journal C **81**, 115 (2021).
DOI 10.1140/epjc/s10052-020-08783-1

Chapter 4

Light propagation in a Born-Infeld environment

Born and Infeld (1934) [17] presented a theory with nonlinear corrections to Maxwell electrodynamics from a classical perspective. The BI Lagrangian is given by

$$L_{\mathrm{BI}}(F,G) = b^2\left\{1-\sqrt{1+\frac{F}{2b^2}-\frac{G^2}{16b^4}}\right\}, \tag{4.0.1}$$

where b isthe maximum attainable electromagnétic field. The linear electromagnetic Maxwell theory is recovered in the limit that $b \mapsto \infty$, then $L_{\mathrm{Maxwell}}(F) = -F/4$.

We examine the propagation of an electromagnetic wave in the BI-NLED background as seen by an accelerated observer. This setup is of interest because according to the Einstein Equivalence Principle, uniformly accelerated frame is equivalent to a gravitational field, and we are always under the influence of such a gravitational environment. A light ray moving in such an accelerated frame will modify its velocity and pulses will be redshifted similarly to the gravitational redshift. We determine the phase velocity of light showing the interplay of the magnetic (or electric) background and the acceleration of the frame. In the limit of zero acceleration, we recover the wave propagating in the BI background, and in the absence of the BI field, we recover the Rindler propagation and the corresponding frequency shifts.

4.1 Effective optical metric and phase velocity of light in a Born-Infeld background

Recalling the equation for the effective optical metrics 2.1.8, using the BI Lagrangian, the two metrics in Eqs. (2.1.9)-(2.1.10) become conformal $g_{\rm eff}^{(1)\mu\nu} = \Xi^2 g_{\rm eff}^{(2)\mu\nu}$, with the conformal factor Ξ^2 being a function of the coordinates, reflecting the nonexistence of birefringence in the BI nonlinear theory. Moreover, a conformal factor does not alter null geodesics, therefore, in what follows we shall omit the superscript (i), $\quad i = 1, 2$; then in the BI case, the effective optical metric is given by

$$g_{\rm eff}^{\mu\nu} = \left(b^2 + \frac{F}{2}\right)\eta^{\mu\nu} + F^{\mu}{}_{\lambda}F^{\lambda\nu}, \tag{4.1.1}$$

where the EM invariant $F = 2(B^2 - E^2)$. Since our goal is to study the propagation of light as seen by an accelerated observer, for completeness, we introduce the accelerated frame or Rindler spacetime and some of its relevant features in the next section, it is worth remarking that Rindler frame is noninertial, i. e. it is not subject to special relativity rules.

4.2 The accelerated frame or the Rindler spacetime.

We are interested in the characteristics of BI electromagnetic fields as seen by observers in a uniform gravitational field. According to the Einstein Equivalence Principle (EEP), a gravitational field can be (locally) modeled by an accelerated frame. An example of a "fake" gravity or accelerated frame is the Rindler space, which we briefly address in this section.

Let us consider an accelerated observer with constant acceleration $a = \sqrt{a_\mu a^\mu}$ in $\hat{z}$ direction and proper time τ. The Minkowski coordinates (t, z) are related to the accelerated observer by

$$t = \frac{1}{a}\mathrm{Sh}(a\tau); \qquad z = \frac{1}{a}\mathrm{Ch}(a\tau), \tag{4.2.1}$$

where we denote $\cosh(x) = \mathrm{Ch}(x)$ and $\sinh(x) = \mathrm{Sh}(x)$. The line element in Minkowski coordinates is related to the Rindler space in coordinates (T, Z, x, y), by [85]:

$$ds^2 = dt^2 - dx^2 - dy^2 - dz^2 = (1 + aZ)^2 dT^2 - dZ^2 - dx^2 - dy^2. \tag{4.2.2}$$

From this expression, we see that the coordinate transformation does not cover the entire Minkowski spacetime. At $Z = \frac{-1}{a}$ the metric becomes degenerate, and therefore the range of the coordinates must be $Z \in (\frac{-1}{a}, \infty)$, $T \in (-\infty, \infty)$. These coordinates cover only a part of the Minkowski spacetime, denoted as Region I in Figure 4.1, with the different regions separated by event horizons located at $z = \pm t$.

Eqs. (4.2.1) represent a hyperbolic curve in Minkowski spacetime, with the semi-major axis at $1/a$,

$$z^2 - t^2 = \frac{1}{a^2}. \tag{4.2.3}$$

The trajectory of the accelerated observer in the Minkowski space is a hyperbola as shown in Figure 4.1. It starts at $z \to \infty$, then slows down as it approaches the origin, returns at a finite distance from the origin, and speeds up as it approaches $z \to \infty$ [86]. Light rays are shown traveling along 45^o null lines. The observer in quadrant I can "send signals" towards the upper quadrant II, as represented by the cone A, but cannot receive signals from the upper quadrant II. The observer in the Rindler frame cannot access any signal beyond the horizon, located at $z = \pm t$, but can receive signals from the inferior quadrant IV, as illustrated with the light cone D; however, A cannot send signals towards D or C [85], [87].

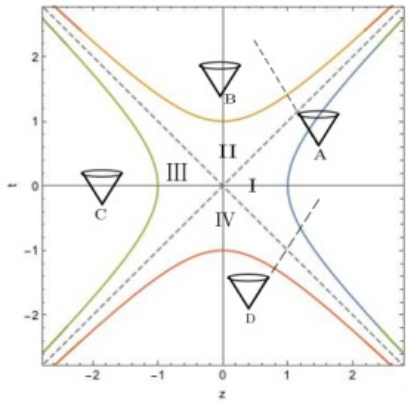

Figure 4.1: The dashed diagonal lines represent the null planes at $z = \pm t$ (horizons). An accelerated observer in Region I follows the hyperbola. They can receive information from regions I and IV and can send signals to regions I and II. Region III is space-like with respect to the whole Region I, and in particular to the worldline of the observer.

To determine what the accelerated observer sees, we need to carry out a coordinate transformation from the Minkowski frame, which can also be called *the Lab frame*, to the accelerated frame. In the accelerated frame we will describe the phenomena from the point of view of a privileged observer at $Z = 0$ with proper time $\tau = T$, but

the general transformation from Minkowski to a Rindler observer located at Z_i with acceleration a_i is given by [88], [89],

$$t_i = (\frac{1}{a_i} + Z_i)\mathrm{Sh}(a_i T_i); \qquad z_i = (\frac{1}{a_i} + Z_i)\mathrm{Ch}(a_i T_i). \tag{4.2.4}$$

Note that taking $Z = 0$ and $T = \tau$ results in Eqs. (4.2.1). Other Rindler observers (other hyperbolas) have different accelerations a_i, and different z_i (Lab coordinates). In the Rindler frame, they have different Z_i, but they all have the same velocity at the points that their world lines intersect a line of simultaneity, as shown in Figure 4.2. The proper position of each observer is $Z_i = 0$ and $\{t = \mathrm{Sh}(a_i T)/a_i, \mathrm{Ch}(a_i T)/a_i\}$, resulting in each observer having a different proper acceleration in the Lab frame. Then referring to the Rindler space as a "Uniformly accelerated reference frame" does not imply that all the observers have the same acceleration; in the Lab frame, these observers do not form a rigid lattice, as they do in the Rindler frame.

To define simultaneity, we consider that for each uniformly accelerated frame, there is a momentarily co-moving inertial frame so that, along the line of simultaneity, both frames have the 4-velocity parallel to each other, and they measure each other at rest, then it is said that they form a rigid lattice of observers and all of them agree on simultaneity, [88]. In Rindler spacetime, the lines that define the simultaneity are $T = n$, where n is an arbitrary constant (shown in Figure 4.2), and correspond to $t = z\mathrm{Th}(an)$ in Minkowski spacetime.

Let τ_A be the proper time of the principal observer, which dictates what is measured by the other observer's clocks. When $\tau_A = 0$ all the observers coincide with the z axis: $T = 0, \quad t = 0$. Let us distinguish the proper time τ and the coordinate time T. The Rindler line element is given by

$$ds^2 = g_{TT} dT^2 + g_{ij} dx^i dx^j, \qquad i, j = \{X, Y, Z\} \tag{4.2.5}$$

The differential proper time $d\tau$ and the spatial line element,$dl^2 = g_{ij} dx^i dx^j$, are such that $dl^2 = -d\tau^2 \mid_{dT=0}$ and the velocity of a Rindler observer is

$$v^2 = \frac{-g_{ij} dx^i dx^j}{dT^2}, \tag{4.2.6}$$

where v^2 is non-negative since we are taking the Minkowski metric, this is, $\eta_{\mu\nu} = \mathrm{diag}(+1, -1, -1, -1)$.

For the null trajectories, $d\tau^2 = 0$,

$$d\tau^2 = g_{TT} dT^2 + g_{ij} dx^i dx^j = 0, \tag{4.2.7}$$

and the phase velocity of a light ray traveling in the z-direction in the Rindler frame is

$$v_{\mathrm{ph}} = \frac{dZ}{dT} = \sqrt{-\frac{g_{TT}}{g_{ZZ}}} = (1 + aZ). \tag{4.2.8}$$

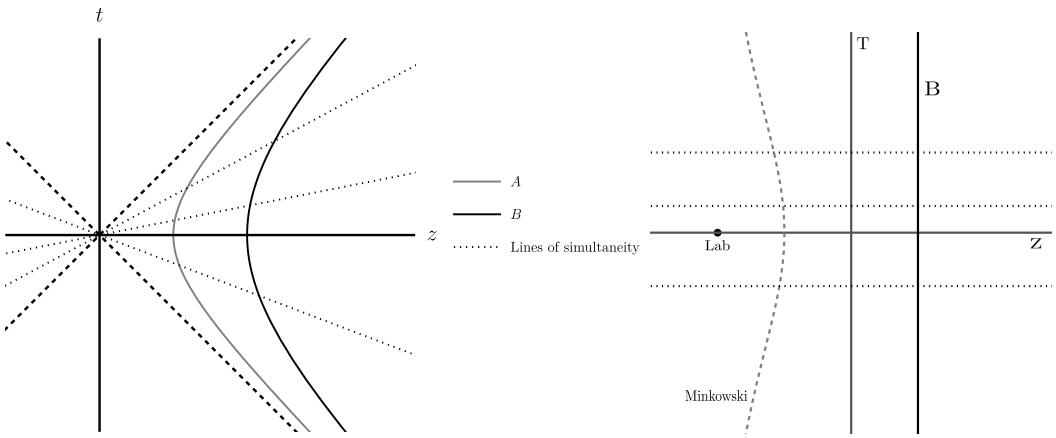

Figure 4.2: The worldlines of two observers A and B in the Minkowski spacetime are shown as the gray and black thick lines in the figure to the left. The dotted lines represent the lines of simultaneity in the Rindler frame. To the left are illustrated the observers in the Minkowski spacetime (z, t), and to the right are the trajectories in the Rindler frame (Z, T). We are considering A as the principal observer, whose trajectory is a vertical straight line (fixed Z); the dot at $\{Z = -\frac{1}{a}, T = 0\}$ is the Lab frame; the observer B is represented by the black thick line; the gray dashed curve corresponds to a third Rindler observer, located between $Z = 0$ and $Z = 1/a_A$.

If we interpret $d\tau/dT$ as the rate of flow of time [88] in the Rindler space, then the speed of light equals the rate of flow of time. The velocity now depends on the position of the observer; it is zero at the horizon $Z = -\frac{1}{a}$ and when $Z = 0$ the velocity is the one in vacuum, $c = 1$. The position $Z = 0$ corresponds to the "principal observer". From Eq. (4.2.8) we see that an observer at $Z > 0$ measures a light velocity greater than $c = 1$. This result is explained using the global line of simultaneity that is rotating in the Lab frame, like a radar. When it intersects the worldlines it moves faster for an observer at higher z (Lab frame) than for an observer closer to the origin. The interpretation is that time flows faster for higher z because the proper time of the observers at greater z is aging faster than for observers closer to the origin. Light therefore covers more distance per unit of time as z increases. However, each accelerated observer measures a local speed of light being $c = 1$, therefore any of them could be chosen as the "master" or "principal" observer.

We can visualize the trajectory of light in Rindler spacetime integrating (4.2.8).

$$Z = \frac{1}{a}\left[-1 + (1 + aZ_0)\exp a\,(T - T_0)\right]. \tag{4.2.9}$$

Then, the measurement of light velocity must be done locally, i.e. at $Z = 0$, the position of the "master" observer.

In the following two sections, 4.3 and 4.4, we address the propagation of light in purely magnetic and purely electric BI backgrounds, respectively, as seen in the Rindler frame.

4.3 Light propagating through a Born-Infeld magnetic background in the Rindler space.

In this section, we determine the phase velocity of light rays propagating in a purely magnetic BI background as seen by an accelerated observer. According to the Einstein Equivalence Principle (EEP), an accelerated frame is equivalent to a uniform gravitational field; therefore, our treatment describes the propagation of light under the influence of a very intense BI electric or magnetic background, as seen by an observer in a uniform gravitational field.

Light trajectories through an intense magnetic field are the null geodesics of the effective optical metric $g^{\mu\nu}_{\rm eff}$, Eq. (4.1.1). We begin with the effective optical metric corresponding to a BI uniform magnetic field B and then transform it into the Rindler accelerated frame.

Considering that the nonvanishing electromagnetic tensor components of the magnetic background are $F^{xy} = -B_z$, $F^{xz} = B_y$, $F^{yz} = -B_x$, and $F = 2B^2$, the effective metric $g^{\mu\nu}_{\rm eff}$ is given by

$$g^{\mu\nu}_{\rm eff} = \begin{pmatrix} b^2+B^2 & 0 & 0 & 0 \\ 0 & -b^2-B_x^2 & -B_xB_y & -B_xB_z \\ 0 & -B_xB_y & -b^2-B_y^2 & -B_yB_z \\ 0 & -B_xB_z & -B_yB_z & -b^2-B_z^2 \end{pmatrix}. \tag{4.3.1}$$

We will consider the uniform magnetic background, with no loss of generality, in the XZ plane as $\vec{B} = B_x\hat{x} + B_z\hat{z} = B\sin\theta\hat{x} + B\cos\theta\hat{z}$. From Eq. (2.2.3), the phase velocity $v_{\rm ph}$ of light propagating through a BI magnetic background, along the $\hat{z}$-direction, with wave frequency ω and wave number $k^z = k$, is

$$v_{\rm ph}^2 \;=\; 1 - \frac{B_x^2}{b^2+B^2}, \tag{4.3.2}$$

where $B^2 = B_x^2 + B_z^2$. Then the effect of the BI magnetic background is slowing down the phase velocity unless the magnetic component transversal to the propagating light is zero, in which case the phase velocity is the one in vacuum. This case was studied in [44].

To determine the phase velocity measured by a Rindler observer, the effective optical metric Eq. (4.3.1) is transformed to the Rindler frame. The transformation matrix to

transform to a Rindler frame with acceleration $\vec{a} = a\hat{z}$ is given by

$$R^{\mu}{}_{\alpha} = \frac{\partial x^{\mu}}{\partial X^{\alpha}} = \begin{pmatrix} (1+aZ)\mathrm{Ch}(aT) & 0 & 0 & \mathrm{Sh}(aT) \\ 0 & 1 & 0 & 0 \\ 0 & 0 & 1 & 0 \\ (1+aZ)\mathrm{Sh}(aT) & 0 & 0 & \mathrm{Ch}(aT) \end{pmatrix}. \tag{4.3.3}$$

The transformed effective optical metric, obtained from $g^{\mu\nu}_{\mathrm{eff,R}} = R^{\mu}_{\alpha} g^{\alpha\beta}_{\mathrm{eff}} R^{\nu}_{\beta}$, is

$$g^{\mu\nu}_{\mathrm{eff,R}} = \begin{pmatrix} \frac{b^2+B_z^2+B_\perp^2\mathrm{Ch}^2(aT)}{(aZ+1)^2} & \frac{B_xB_z\mathrm{Sh}(aT)}{aZ+1} & \frac{B_yB_z\mathrm{Sh}(aT)}{aZ+1} & -\frac{(B_\perp^2\mathrm{Sh}(2aT)}{2(1+aZ)} \\ \frac{B_xB_z\mathrm{Sh}(aT)}{aZ+1} & -\left(b^2+B_x^2\right) & -B_xB_y & -B_xB_z\mathrm{Ch}(aT) \\ \frac{B_yB_z\mathrm{Sh}(aT)}{aZ+1} & -B_xB_y & -\left(b^2+B_y^2\right) & -B_yB_z\mathrm{Ch}(aT) \\ -\frac{(B_\perp^2\mathrm{Sh}(2aT)}{2(1+aZ)} & -B_xB_z\mathrm{Ch}(aT) & -B_yB_z\mathrm{Ch}(aT) & B_\perp^2\mathrm{Sh}^2(aT)-b^2-B_z^2 \end{pmatrix}, \tag{4.3.4}$$

where the superscript "R" denotes the effective optical metric $g^{\mu\nu}_{\mathrm{eff}}$ in the Rindler frame and $B_\perp^2 = B_x^2 + B_y^2$. In the case of $a = 0$, the effective optical metric Eq. (4.3.1) is recovered. As a consequence of the transformation to the magnetic background, electric components arise in a similar way to when a Lorentz boost is performed. The nonvanishing electromagnetic tensor components are now $F_R^{tx} = \frac{B_y\mathrm{Sh}(aT)}{1+aZ}$, $F_R^{ty} = -\frac{B_x\mathrm{Sh}(aT)}{1+aZ}$, $F_R^{xz} = B_y\mathrm{Ch}(aT)$, $F_R^{yz} = -B_x\mathrm{Ch}(aT)$, $F_R^{xy} = -B_z$. The invariants are preserved, so $F = 2B^2$, $G = 0$.

The corresponding covariant effective optical metric is

$$g^{\mathrm{eff,R}}_{\mu\nu} = \begin{pmatrix} (aZ+1)\left[b^2 - B_\perp^2\mathrm{Sh}^2(aT)\right] & B_xB_z\mathrm{Sh}(aT) & B_yB_z\mathrm{Sh}(aT) & -\frac{1}{2}B_\perp^2\mathrm{Sh}(2aT) \\ B_xB_z\mathrm{Sh}(aT) & -\frac{b^2+B_y^2+B_z^2}{aZ+1} & \frac{B_xB_y}{aZ+1} & \frac{B_xB_z\mathrm{Ch}(aT)}{aZ+1} \\ B_yB_z\mathrm{Sh}(aT) & \frac{B_xB_y}{aZ+1} & -\frac{b^2+B_x^2+B_z^2}{aZ+1} & \frac{B_yB_z\mathrm{Ch}(aT)}{aZ+1} \\ -\frac{1}{2}B_\perp^2\mathrm{Sh}(2aT) & \frac{B_xB_z\mathrm{Ch}(aT)}{aZ+1} & \frac{B_yB_z\mathrm{Ch}(aT)}{aZ+1} & -\frac{B_\perp^2\mathrm{Ch}^2(aT)+b^2}{aZ+1} \end{pmatrix}. \tag{4.3.5}$$

For an EM wave in the $i-$direction with wave number $\kappa_R^{\mu} = (\omega_R, k_R^i)$, the phase velocity is given by Eq. (2.2.3), and the acceleration of the Rindler frame is $\vec{a} = a\hat{z}$. We consider successively three different propagating directions of the wave: $+\hat{z}$, $-\hat{z}$ and $+\hat{x}$; the setting is shown in Figure 4.3. We analyze the corresponding phase velocities in the next subsections.

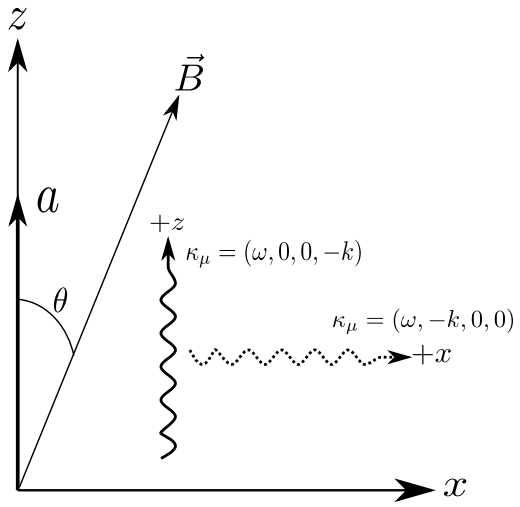

Figure 4.3: Scheme showing the relative directions: the proper acceleration of the Rindler frame is $\vec{a} = a\hat{z}$; the wavy lines indicate two propagating waves, one (thick) traveling in the $\hat{z}$-direction and another (dotted) in the $\hat{x}$-direction. The magnetic field makes an angle θ with the acceleration of the Rindler frame.

4.3.1 Magnetic Born-Infeld background. Light propagating in the $\pm\hat{z}$ direction

For a wave traveling in the $\pm\hat{z}$ direction: $\kappa_\mu = (\omega, 0, 0, \mp k)$ the phase velocity, from Eq. (2.2.3), is given by

$$\frac{v_{\rm ph}^{\rm R\pm\hat{z}}}{1+aZ} = \frac{\omega}{k} = \frac{\mp B_x^2 \mathrm{Sh}(aT)\mathrm{Ch}(aT) + \sqrt{(b^2+B^2)\,(b^2+B_z^2)}}{\left(b^2+B^2+B_x^2\mathrm{Sh}^2(aT)\right)}, \tag{4.3.6}$$

where the $\mp$ sign corresponds to the waves propagating in $+\hat{z}$ and in $-\hat{z}$ directions, respectively, and $B^2 = B_x^2 + B_z^2$. From this expression we can see that $v_{\rm ph}^{\rm R}$ depends on aT and aZ, i.e., the effect of increasing time is equivalent to increasing the acceleration of the frame, recalling that the Rindler observer will remain at a fixed Z. In addition, the acceleration affects the phase velocity only if there is a magnetic component that is transversal to the acceleration (in this case B_x). In the limit, $a \mapsto 0$, the expression for velocity in a BI magnetic field, Eq. (4.3.2), is recovered. Note that the only difference between the wave propagating along $+\hat{z}$ and $-\hat{z}$ is the sign in the first term in Eq. (4.3.6), which indicates that the Rindler frame distinguishes the travel direction of light. Moreover, it implies that the phase velocity for the

wave along $-\hat{z}$ will be greater than for the one traveling in the opposite direction.

Expanding $v_{\rm ph}^{\rm R}$, Eq. (4.3.6), in powers of B^2/b^2 and keeping terms of order $\mathcal{O}(1/b^2)$, i.e., neglecting terms of order $\mathcal{O}(1/b^4)$ and higher, we arrive at

$$\frac{v_{\rm ph}^{\rm R\pm\hat{z}}}{1+aZ} = 1 - \frac{B_x^2}{2b^2}\left\{1 + 2{\rm Sh}(aT)\left[{\rm Sh}(aT) \pm {\rm Ch}(aT)\right]\right\} + \mathcal{O}(1/b^4). \tag{4.3.7}$$

This approximation is still valid for very strong fields. If we consider, for instance, that $B^2/b^2 \approx 10^{-2}$, then the BI field B can be of the order 10^{10}Tesla, that is ten times the critical Schwinger field $B_{\rm cr} \approx 10^9$ Tesla. In the limit, $a \mapsto 0$, the expression for the pure BI magnetic field Eq. (4.3.2) is recovered, up to terms in $\mathcal{O}(1/b^2)$. Notice that even if $B \mapsto b$, the phase velocity reaches a minimum of half the velocity of light in vacuum. The linear limit (vanishing BI field) is obtained with $b \mapsto \infty$ and then $(v_{\rm ph}^R)^2 = (1+aZ)^2$ is recovered. In Eq. (4.3.7), the term that depends on aT increases monotonically for the wave traveling in $+\hat{z}$ as ${\rm Sh}(aT)\left[{\rm Sh}(aT) + {\rm Ch}(aT)\right]$, while for the wave traveling in $-\hat{z}$, the term, ${\rm Sh}(aT)\left[{\rm Sh}(aT) - {\rm Ch}(aT)\right]$, decreases monotonically up to $-1/2$. The effect of the accelerating frame in one case $(+\hat{z})$ is of slowing down the wave and in the other $(-\hat{z})$ is of increasing the phase velocity. In the latter case, the Rindler effect is opposite to the BI effect. Therefore, for a Rindler observer accelerated in $+\hat{z}$ direction the phase velocity of the wave propagating in the $+\hat{z}$ direction is smaller than that of the wave along $-\hat{z}$. Intuitively, this corresponds to traveling in the same direction of the wave in the first case, and in the opposite direction in the second case. This effect is superposed with the BI slowing down of the wave and the result is illustrated in Figures 4.4 and 4.5. As the intensity of the background field increases the light velocity diminishes, and by turning off the BI background field the light velocity in vacuum is recovered. Contrary to what happens for the wave propagating in $+\hat{z}$ direction, for the wave propagating in $-\hat{z}$ direction the pace of slowing down decreases as aT increases. In the limit of long times or large acceleration, $aT \mapsto \infty$, the BI effect of slowing down is lost, and the Rindler phase velocity $(v_{\rm ph}^R)^2 = (1+aZ)^2$ is recovered.

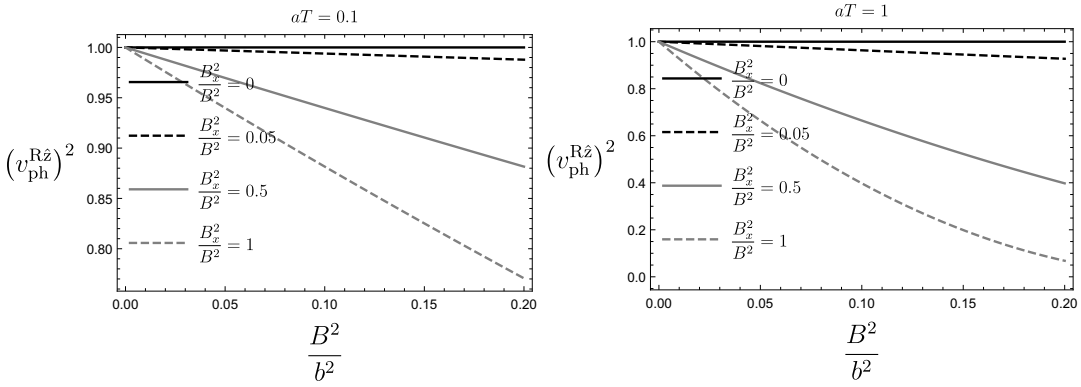

Figure 4.4: The plots for the squared phase velocity of a light ray propagating in z direction through a BI magnetic background as seen by an observer with acceleration a in the $\hat{z}$ direction. The plots are for different values of aT; as aT increases, the velocity slows down more rapidly. The intensities of the perpendicular magnetic components vary as shown and $B^2 = B_x^2 + B_z^2$.

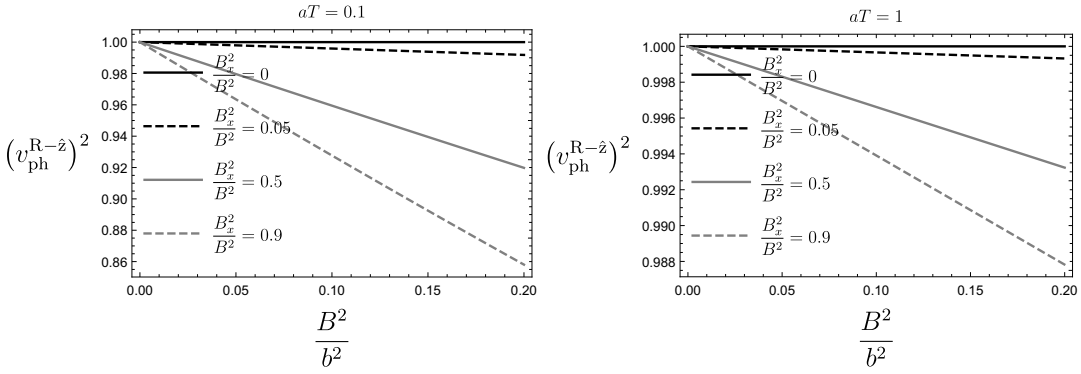

Figure 4.5: Phase velocities for a wave moving in the $-\hat{z}$ direction for different values of aT; v_{ph} is smaller as the magnetic field increases. As aT increases, the velocity slows down at a slower pace. The intensities of the perpendicular magnetic components vary as shown and $B^2 = B_x^2 + B_z^2$.

4.3.2 Magnetic Born-Infeld background. Light propagating in the $+\hat{x}$ direction

For a wave moving in the $\hat{x}$ direction with wave number $\kappa_\mu^R = (\omega_R, -k_R, 0, 0)$, the magnetic background component along $\hat{x}$, B_x, is parallel to the propagating ray and perpendicular to the Rindler acceleration, while B_z is perpendicular to the light direction. The phase velocity,

from Eq. (2.2.3), is given by

$$\frac{v_{\rm ph}^{\rm R\hat{x}}}{(1+aZ)} = \frac{B_x B_z {\rm Sh}(aT) + \sqrt{(b^2+B^2)\left(b^2+B_x^2{\rm Ch}^2(aT)\right)}}{b^2+B^2+B_x^2{\rm Sh}^2(aT)}. \tag{4.3.8}$$

In this case, the effect of turning off the B_x component eliminates the terms depending on aT, since only the transversal (to the acceleration frame) magnetic field affects the velocity of propagation. Making $a=0$ we obtain

$$v_{\rm ph}^{\rm R\hat{x}} = \sqrt{1-\frac{B_z^2}{b^2+B^2}}, \tag{4.3.9}$$

that corresponds to the pure BI effect of slowing down $v_{\rm ph}$. Expanding $v_{\rm ph}^{\rm R\hat{x}}$ in powers of B^2/b^2 and keeping terms of order $\mathcal{O}(1/b^2)$, i.e., neglecting terms of order $\mathcal{O}(1/b^4)$ and higher, we arrive at

$$\frac{v_{\rm ph}^{\rm R\hat{x}}}{(1+aZ)} = 1 - \frac{1}{2b^2}\left[B_z - B_x{\rm Sh}(aT)\right]^2 + \mathcal{O}(1/b^4). \tag{4.3.10}$$

In the linear limit, $b \mapsto \infty$, we recover the Rindler velocity, $(v_{\rm ph}^{\rm R\hat{x}})^2 = (1+aZ)^2$. In this case, the acceleration of the frame gives an effect opposite to the BI slowing down but only in a certain range of (aT). The minimum value of (4.3.10) occurs for

$$aT = {\rm ArcSinh}\frac{B_z}{B_x}. \tag{4.3.11}$$

For aT larger than the one of the minimum, $aT > {\rm ArcSh}(\frac{B_z}{B_x})$, $v_{\rm ph}^{R\hat{x}}$ decreases such that in the limit of large aT, $v_{\rm ph}^{R\hat{x}}$ approaches zero. Making zero the component parallel to the acceleration, $(B_z=0)$, the phase velocity becomes

$$\frac{v_{\rm ph}^{\rm R\hat{x}}}{(1+aZ)} = 1 - \frac{B_x^2}{2b^2}{\rm Sh}^2(aT); \tag{4.3.12}$$

while if the magnetic component that is perpendicular to the acceleration vanishes $(B_x=0)$,

$$\frac{v_{\rm ph}^{\rm R\hat{x}}}{(1+aZ)} = 1 - \frac{B_z^2}{2b^2}. \tag{4.3.13}$$

Then if we aimed to diminish the phase velocity by the maximum amount, the most effective way would be to turn off the component along the Rindler acceleration, $B_z=0$, since Sh(aT) $\geq$ 0, $\quad \forall aT$. Figure 4.6 shows the phase velocity of the wave traveling in $\hat{x}$ direction for different values of aT.

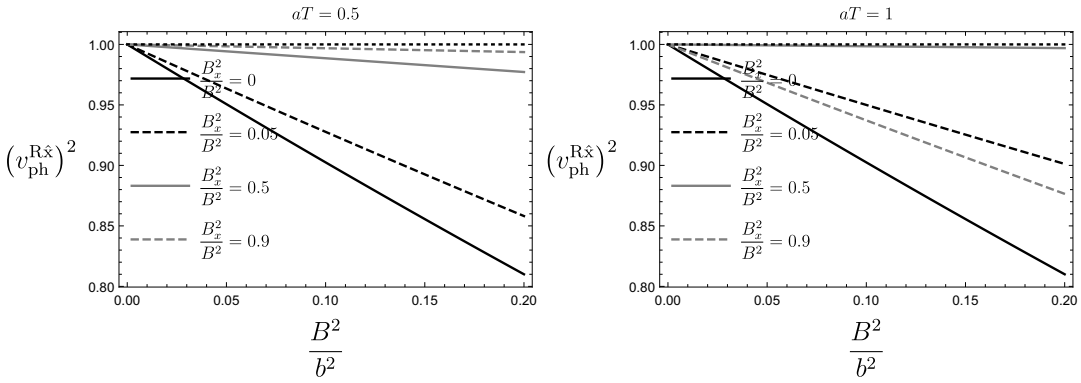

Figure 4.6: Phase velocities for the wave moving in the $\hat{x}$ direction, for different values of aT. In the plot to the left, for $aT = 0.5$, as B_x increases the phase velocity tends to the velocity of light in vacuum. To the right, for $aT = 1$, even for large field components, $(B_x/B)^2 = 0.9$ the phase velocity does not approach the one in vacuum.

In Figure 4.7 we compare the phase velocities for the three different directions of light rays. For all three directions of the light ray, $v_{\rm ph}^R$ decreases as B increases for a fixed (aT). The smallest velocity occurs for the wave moving in the $+\hat{z}$ direction. Figure 4.8 shows the phase

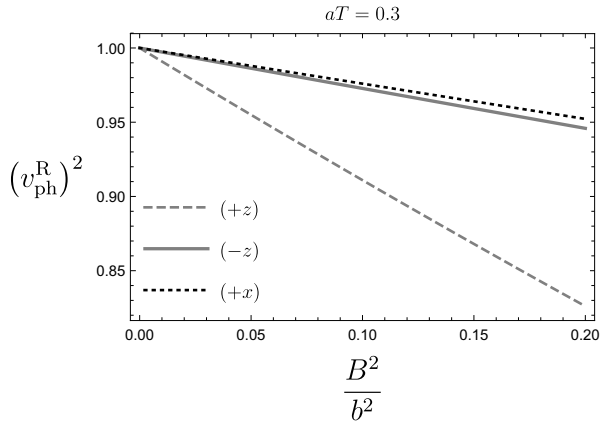

Figure 4.7: The phase velocities for the three directions of propagation of the light wave in the Rindler frame are shown. The Rindler acceleration is $a\hat{z}$. For all three directions $v_{\rm ph}^R$ decreases as B/b increases and $aT = 0.3$. The smallest velocity is for the wave moving in the $+\hat{z}$ direction. In this plot, the parallel and the transversal magnetic field components have the same intensity $B_x = B_z = B/\sqrt{2}$.

velocities of the light rays propagating along the three considered directions as a function of

aT, for fixed $(B/b)^2 = 0.2$. The parallel and transversal magnetic field components have the same intensities $B_x = B_z = B/\sqrt{2}$.

The increasing or decreasing phase velocity depends on the values of aT. For smaller values of aT, the velocity is smaller for the wave moving along $+\hat{z}$ and closer to $c = 1$ for the waves traveling in the $-\hat{z}$ and $+\hat{x}$ directions. For values of $aT > 2$, $v_{\rm ph}^R$ is smaller for the wave moving along $+\hat{x}$ and approaches $c = 1$ for the waves traveling in the $\pm\hat{z}$ directions. As aT increases the BI effect of slowing down the phase velocity is canceled for the waves traveling in the $\pm\hat{z}$ directions. Recall that these are the velocities as measured by the accelerated observer. This observer moves with respect to the light ray, first towards it, then reaching it and moving away. This does not violate any relativity principle since the Rindler frame is not inertial. The trajectories of light rays in $\pm\hat{z}$ directions are shown in Figure 4.9. From the previous analysis,

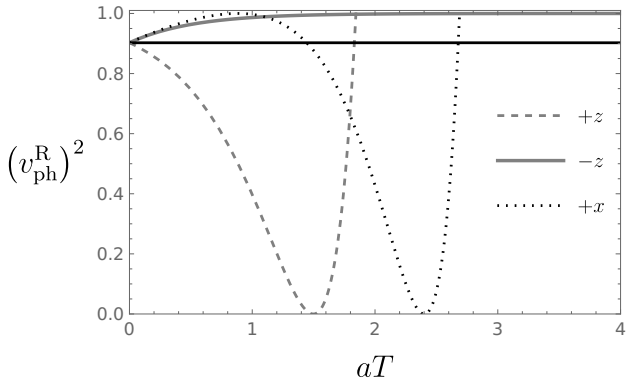

Figure 4.8: The squared modulus of phase velocities as a function of aT, in Eq. (4.3.10) are shown, for a fixed magnetic background, $(B/b)^2 = 0.2$. The magnetic field components are $B_z = B_x = B/\sqrt{2}$. The black thick line represents the phase velocity of the light ray in the presence of the BI magnetic background when $aT = 0$, this is, the phase velocity $(v_{\rm ph}^{\rm R})^2 = 1 - B_x^2/2b^2$. For the waves moving in the $+\hat{z}$ and $+\hat{x}$ directions, $v_{\rm ph}^{\rm R}$ decreases up to a minimum and then increases reaching the velocity in vacuum. This corresponds to the Rindler observer's view, which initially is behind the light ray, reaches it, and then moves away from it. Since the accelerated frame is no longer inertial, there is no conflict with surpassing the light velocity in vacuum. Light in the $-\hat{z}$ direction reaches $c = 1$ increasing monotonically.

we can summarize the behavior of the phase velocity of a light ray propagating through the BI

magnetic field as seen by an observer with acceleration $\vec{a} = a\hat{z}$: the phase velocity depends on aT such that the effect of increasing the acceleration is the same as that of time elapsing. For waves moving in the $+\hat{z}$ and $+\hat{x}$ directions, $v_{\rm ph}^{\rm R}$ decreases to a minimum and then increases to reach the velocity in vacuum, while for light in the $-\hat{z}$ direction it reaches $c = 1$ departing from the Rindler $v_{\rm ph}^{\rm R}$ and increasing monotonically. The change in direction of light can be understood by thinking of the relative motion of the accelerated observer, which is initially behind the light ray, then reaches it when the accelerated observer measures $v_{\rm ph}^{R} = 0$ and finally moves away from the light ray (the accelerated observer sees that the light ray changes direction). If the magnetic field is in the same direction as the Rindler acceleration, then there is no effect on the phase velocity. For a fixed BI magnetic field, the smallest velocity is reached faster for the wave moving in the $+\hat{z}$ direction. Figures 4.7 and 4.8 illustrate these behaviors. The question of whether the values of the BI field are reachable in experiments

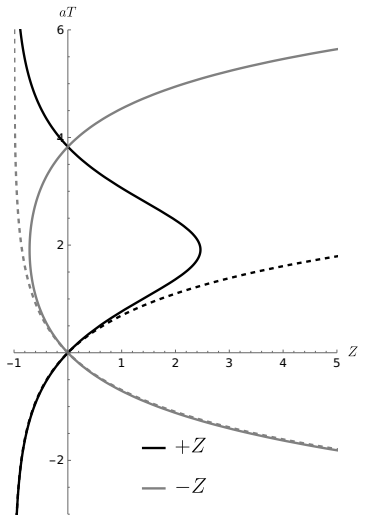

Figure 4.9: The trajectories in the Rindler space followed by the $\pm z$ waves are shown. The dashed lines represent the trajectories for the waves when there is no BI effect, and the thick lines are the trajectories of the waves in the presence of a magnetic background with $B_x = B_z = B/\sqrt{2}$ and $(B/b)^2 = 0.2$.

is discussed in [45]. It is not clear whether it would be possible to build such an accelerated frame, or if it would be possible to maintain the acceleration for long enough to observe the predicted changes in the phase velocities.

4.4 Light propagating through a Born-Infeld electric background in the Rindler space.

The propagation of an EM wave through an intense uniform electric field is of interest since the production of vacuum electron-positron pairs is predicted in [77]. This has not yet been measured, however, it may be feasible in the near future, due to the high power reached recently by lasers [82], [83]. Considering that the nonvanishing electromagnetic tensor components of a purely uniform electric background are $F^{xt} = E_x$, $F^{yt} = E_y$, $F^{zt} = E_z$, and the electromagnetic invariants $G = 0$ and $F = -2E^2$ ($B = 0$), the expression for the effective optical metric from Eq. (4.1.1) is

$$g^{\mu\nu}_{\text{eff}} = \begin{pmatrix} b^2 & 0 & 0 & 0 \\ 0 & -b^2 + E_y^2 + E_z^2 & -E_x E_y & -E_x E_z \\ 0 & -E_x E_y & -b^2 + E_x^2 + E_z^2 & -E_y E_z \\ 0 & -E_x E_z & -E_y E_z & -b^2 + E_\perp^2 \end{pmatrix}. \tag{4.4.1}$$

From Eq. (2.2.3) the phase velocity of light propagating in $\hat{z}$ direction through a uniform BI electric is determined as

$$v_{\text{ph}}^2 = 1 - \frac{E_\perp^2}{b^2} \tag{4.4.2}$$

with $E_\perp^2 = E_x^2 + E_y^2$, being the electric field component perpendicular to the acceleration direction $\hat{z}$. Note that in the absence of the perpendicular component, the phase velocity is that in vacuum. This expression was also derived in [44]. According to Eq. (4.4.2) in principle, the wave could reach zero velocity; however, taking the average in polarization and the electric field components, the minimum accessible phase velocity is $< v_{\text{ph}} >= 1/3$ [49].

Transforming the effective metric for the electric BI background to the Rindler frame with (4.3.3), we obtain

$$g^{\mu\nu}_{\text{eff,R}} = \begin{pmatrix} \frac{E_\perp^2 \text{Sh}^2(aT) + b^2}{(aZ+1)^2} & \frac{E_x E_z \text{Sh}(aT)}{aZ+1} & \frac{E_y E_z \text{Sh}(aT)}{aZ+1} & -\frac{E_\perp^2 \text{Sh}(aT)\text{Ch}(aT)}{aZ+1} \\ \frac{E_x E_z \text{Sh}(aT)}{aZ+1} & -b^2 + E_y^2 + E_z^2 & -E_x E_y & -E_x E_z \text{Ch}(aT) \\ \frac{E_y E_z \text{Sh}(aT)}{aZ+1} & -E_x E_y & -b^2 + E_x^2 + E_z^2 & -E_y E_z \text{Ch}(aT) \\ -\frac{E_\perp^2 \text{Sh}(aT)\text{Ch}(aT)}{aZ+1} & -E_x E_z \text{Ch}(aT) & -E_y E_z \text{Ch}(aT) & E_\perp^2 \text{Ch}^2(aT) - b^2 \end{pmatrix}. \tag{4.4.3}$$

As previously, we consider that the frame acceleration is $\vec{a} = a\hat{z}$ and that, with no loss of generality, the uniform BI field is located in the XZ plane, $\vec{E} = E_x\hat{x} + E_z\hat{z}$. The phase velocity of the wave moving in the $\pm\hat{z}$ and $+\hat{x}$ directions is then obtained from Eq. (2.2.3) and analyzed in the next two subsections.

4.4.1 Electric Born-Infeld background. Light propagating in the $\pm\hat{z}$ direction

For the wave moving in the $\pm\hat{z}$ direction, and considering the position of the principal observer at $Z = 0$, the phase velocity resulting from Eq. (2.2.3) is given by

$$v_{\rm ph}^{\rm R\pm\hat{z}} = \frac{\mp E_x^2 {\rm Sh}(aT){\rm Ch}(aT) + \sqrt{b^2\left(b^2 - E_x^2\right)}}{b^2 + E_x^2 {\rm Sh}^2(aT)}, \tag{4.4.4}$$

The term under the square root sign is used to recover the phase velocity in the absence of acceleration. The difference in the phase velocity between the wave propagating in $+\hat{z}$ direction and the one along $-\hat{z}$ is then only the sign in the first term. The consequence of this difference is that the magnitude of the phase velocity for the wave in the $+\hat{z}$ direction is smaller than the one traveling in the opposite direction. There are several features shared with the magnetic case: $v_{\rm ph}^{\rm R}$ depends on aT and aZ, i.e., the effect of increasing time T or spatial coordinate Z is equivalent to increasing the acceleration of the frame. In addition, the acceleration affects the phase velocity only if there is an electric component that is transversal to the acceleration (in this case E_x); i.e., the acceleration of the frame is affected only by the electric component that is transversal to $\vec{a} = a\hat{z}$. Expanding $v_{\rm ph}^{\rm R}$ in powers of E^2/b^2 and keeping terms of order $\mathcal{O}(1/b^2)$, i.e., neglecting terms of order $\mathcal{O}(1/b^4)$ and higher, we arrive at

$$v_{\rm ph}^{\rm R\pm\hat{z}} = 1 - \frac{E_x^2}{2b^2}\left\{1 + 2{\rm Sh}(aT)\left[{\rm Sh}(aT) \pm {\rm Ch}(aT)\right]\right\}. \tag{4.4.5}$$

Comparing the previous equation with the corresponding equation for the magnetic BI background, Eq. (4.3.7), we notice that the expression is the same apart from changing the magnetic to the electric component, $B_x \mapsto E_x$. This means that the application of a magnetic uniform background produces the same effect as the application of an electric background, as

long as the transversal magnetic and electric components have the same magnitude. Consequently, the limiting cases are very similar to the ones for the magnetic background: in the limit $a \mapsto 0$, the expression for the pure BI electric field Eq. (4.4.2) is recovered. The linear limit (no BI field) is obtained with $b \mapsto \infty$ and then $v_{\rm RT}^2 = 1$ is recovered ($Z = 0$). In the limit of long times or large acceleration ($aT \mapsto \infty$) the BI effect of slowing down the phase velocity is lost, and the Rindler phase velocity $v_{\rm RT}^2 = (1 + aZ)^2$ is recovered. In this case, we omit the figures for $v_{\rm ph}^{\rm R}$ for the wave propagating along $\pm\hat{z}$ to avoid redundancy.

4.4.2 Electric Born-Infeld background. Light propagating in the $+\hat{x}$ direction

For the wave moving in the $+\hat{x}$ direction, the phase velocity is

$$v_{\rm ph}^{\rm R\hat{x}} = \frac{E_x E_z {\rm Sh}(aT) + \sqrt{b^2\left(E_x^2 {\rm Sh}^2(aT) + b^2 - E_z^2\right)}}{E_x^2 {\rm Sh}^2(aT) + b^2}. \tag{4.4.6}$$

Recall that E_x is perpendicular with respect to the acceleration of the Rindler frame, $\vec{a} = +a\hat{z}$. In this case, both components of the BI electric field, parallel and perpendicular to the acceleration, play a role. In the case that $E_x = 0$ there is no effect of the acceleration of the frame, and the wave slows down due to the pure BI effect,

$$v_{\rm ph}^{\rm R\hat{x}} = \sqrt{1 - \frac{E_z^2}{b^2}} \approx 1 - \frac{E_z^2}{2b^2}. \tag{4.4.7}$$

Note that even if $E_z = b$, the light velocity does not vanish but there is a lower bound of $v_{\rm phmin}^{R\hat{x}} = 1/2$. Expanding $v_{\rm ph}^{\rm R\hat{x}}$ in powers of E^2/b^2 and keeping terms of order $\mathcal{O}(1/b^2)$, i.e., neglecting terms of order $\mathcal{O}(1/b^4)$ and higher, we arrive at

$$v_{\rm ph}^{\rm R\hat{x}} = 1 - \frac{1}{2b^2}\left[E_z - E_x {\rm Sh}(aT)\right]^2. \tag{4.4.8}$$

Note that this is the same expression as Eq. (4.3.10) with $B_i \to E_i$. Then, as in the $\pm\hat{z}$ directions, the limiting cases are very similar to those for the magnetic background at orders B^2/b^2, or E^2/b^2. Since the behaviours are the same than in the magnetic case, we omit the figures for the wave propagating along $\hat{x}$ and the comparison between the considered directions.

For the light propagating along $+\hat{z}$ direction, $v_{\rm ph}^R$ diminishes monotonically in an interval of (aT) until it reaches a minimum that is arbitrarily close to zero. For (aT) larger than a certain aT_c given by

$$aT_c = \frac{1}{2}\text{ArcSh}\left(2\sqrt{\frac{b^2 - E_x^2}{E_x^4}}\right), \tag{4.4.9}$$

$v_{\rm ph}^R$ changes its propagation direction and increases up to the light velocity in vacuum. For the wave in the $+\hat{x}$ direction, the behavior is qualitatively similar to that for the wave along $+\hat{z}$. As aT increases, the wave slows down monotonically until reaching a minimum that is arbitrarily close to zero, then increases till reaching $v_{\rm ph}^R = 1$; the slowing down is maximized for $E_z = 0$. For the wave moving in the $-\hat{z}$ direction, as aT increases the phase velocity reaches its value in vacuum. Recall that these velocities are measured by the accelerated observer, and the relative directions change as aT increases. Initially, the observer chases the light ray, and as it approaches the wave, the velocity of the wave seems to decrease and eventually reaches zero (the moment the observer reaches the wave). The relative direction then changes and subsequently, the observer moves away from the wave, and the velocity of the wave starts to increase. The plot shows the modulus squared of the phase velocity. Since the accelerated frame is no longer inertial, no Lorentz invariance is expected.

If the electric field component that is perpendicular to the acceleration vanishes, then there is no effect neither of the acceleration nor the BI field on the phase velocity, and its value is the one in vacuum.

4.4.3 The phase velocities for strong fields

The series expansion of the phase velocities up to terms of order B^2/b^2 or E^2/b^2 gives the same behavior for BI magnetic and electric backgrounds. However, it is worth (briefly) discussing the behavior of the phase velocities considering the exact expressions, Eqs. (4.4.4) and (4.4.6). For strong fields, i.e., when the fields approach the maximum attainable electromagnetic field, differences arise and the electric and the magnetic backgrounds can be distinguished.

Figure 4.10 plots the exact expressions for the phase velocities, Eqs. (4.4.4) and (4.4.6), for waves moving in the $\pm\hat{z}$ and $\hat{x}$ directions.

In (a), for waves moving in the $\pm\hat{z}$ direction, the lowest phase velocity is reached by the wave in an electric background. The wave moving in the $\hat{z}$ direction reaches lower values in both background fields. The behavior of the wave moving in the $\hat{x}$ direction is similar to the one in $-\hat{z}$ but it reaches slightly higher values in both background fields.

Note in Figure 4.10 that for the range $\frac{B^2}{b^2} < 0.2$ or $\frac{E^2}{b^2} < 0.2$ it is not possible to distinguish between the magnetic and electric background.

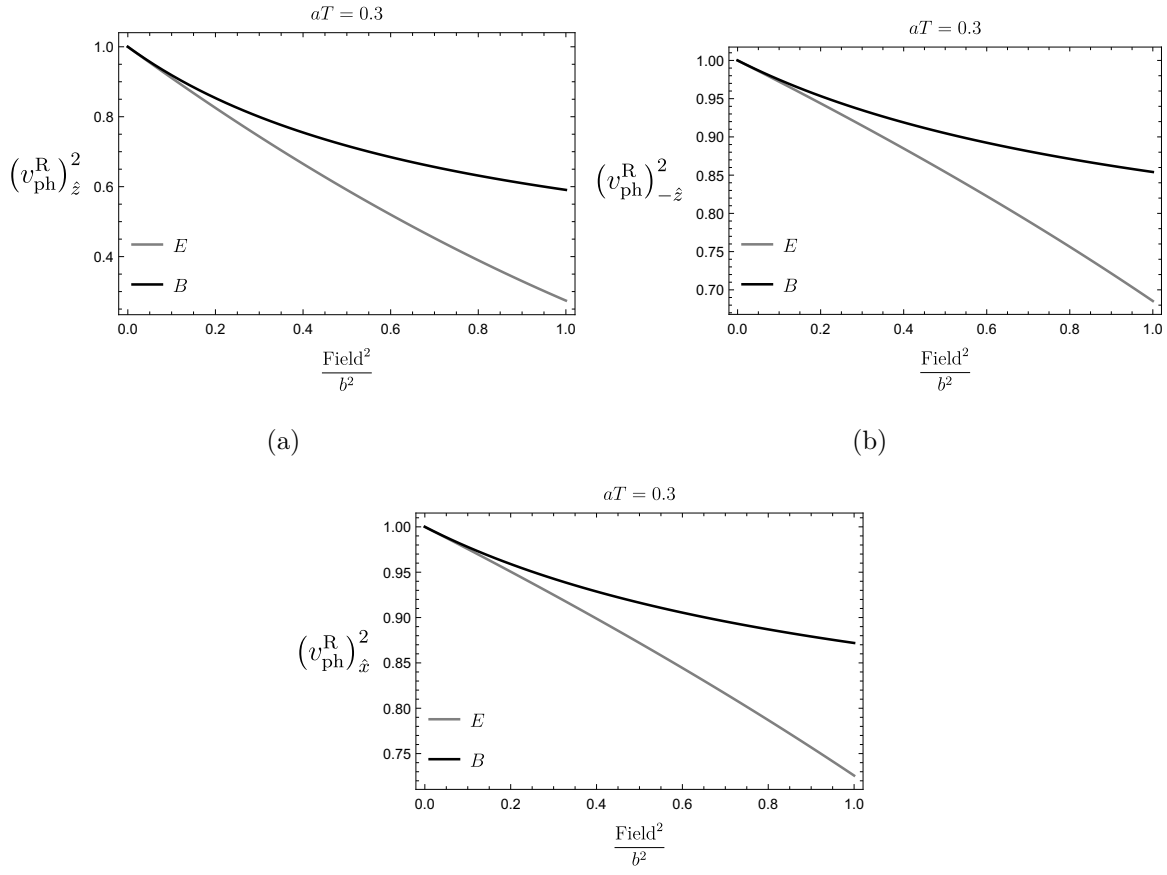

Figure 4.10: The exact expressions, Eqs. (4.4.4) and (4.4.6), are shown for fixed aT. The black curve is for a BI magnetic background and the gray curve corresponds to a BI electric background. The upper plots correspond to waves moving in the $\pm\hat{z}$ directions, and the bottom to movement in the $\hat{x}$ direction. We consider that the components of the background fields have the same intensities, $B_x = B_z$, and $E_x = E_z$.

For completeness, in Figure 4.11 we compare the behavior of the phase velocities as a function of aT for fixed electric and magnetic BI background. Comparing (a) and (b), note that the behavior is similar for both background fields. For waves moving in the $\pm\hat{z}$ directions, as aT is higher the phase velocity tends to the velocity of light in vacuum. The phase velocity tends to zero as aT increases for the wave moving in $\hat{x}$ direction.

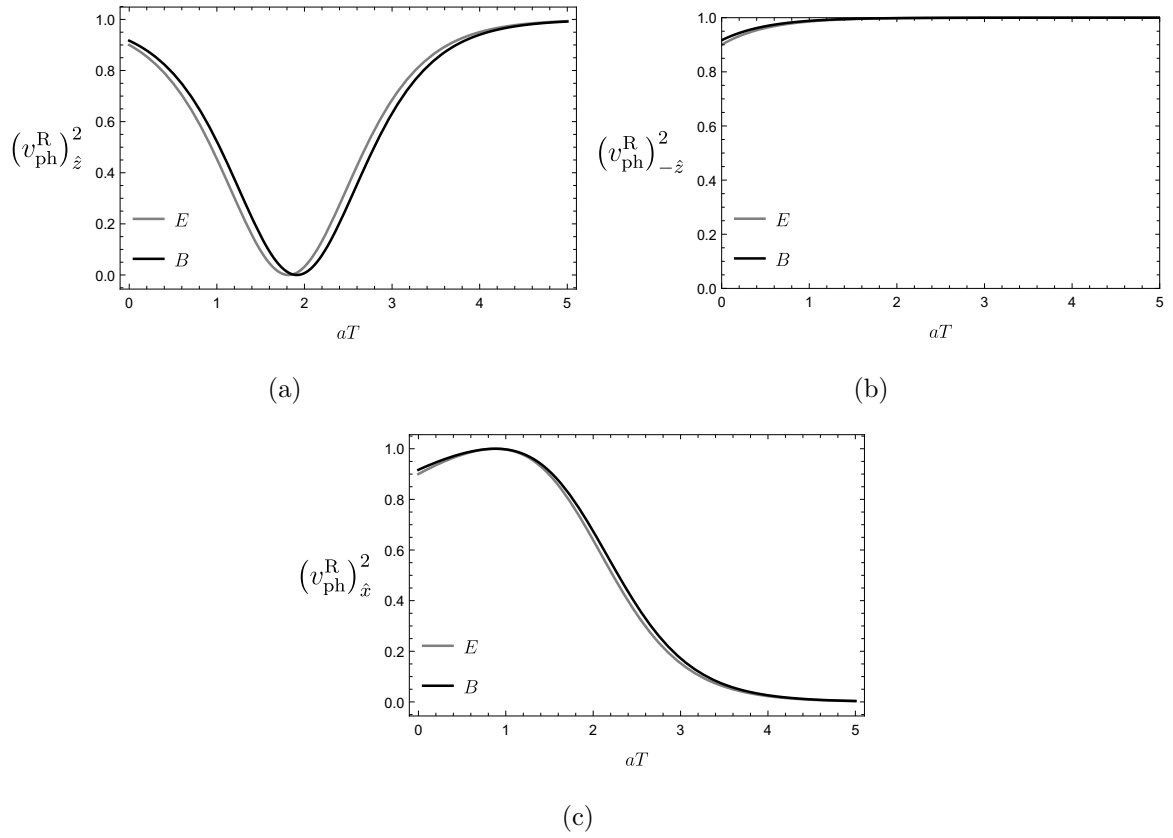

Figure 4.11: The exact expressions, Eqs. (4.4.4) and (4.4.6), are shown as a function of aT, for a fixed BI background. The components of the background fields are of the same magnitude, $B_x = B_z$, $E_x = E_z$, and $B^2/b^2 = 0.2$, $E^2/b^2 = 0.2$; the behavior of the phase velocity is similar in both backgrounds.

4.5 The redshift of light pulses propagating through a Born-Infeld background in the Rindler frame

Gravitational redshift is the increment of the wavelength of electromagnetic radiation due to the presence of a gravitational field. According to the Einstein Equivalence Principle (EEP), an accelerated frame is equivalent to a gravitational field, and it is therefore expected that light pulses sent from one accelerated object to another will modify their frequency, resembling what happens in the presence of a gravitational field. This is indeed what happens, see [88], [90], [91], [92].

In this section, we determine how the redshift due to the acceleration of the frame is affected by the addition of a BI magnetic background.

The redshift, denoted as z_R, can be written in terms of the intervals in the proper time of emission $\Delta\tau_e$ and reception $\Delta\tau_r$ of two light rays with wavelength λ and frequency f as:

$$z_R + 1 = \frac{\lambda_r}{\lambda_e} = \frac{f_e}{f_r} = \frac{\Delta\tau_r}{\Delta\tau_e} > 1 \tag{4.5.1}$$

where the subscripts e and r refer to the emitter and receiver, respectively. Therefore, to determine the redshift in the Rindler frame we first need to calculate the proper time intervals elapsed between sending the first signal and the second one, $\Delta\tau_e$ and the interval elapsed between the reception of the two pulses, $\Delta\tau_r$, as measured by the receiver. These intervals will be different if a redshift occurs. In Figure 4.12 are illustrated the time intervals for two accelerated objects A and B. Figure 4.13 shows the intervals in the world lines of the accelerated objects in the presence of a BI magnetic background.

When A sends a light pulse, the light trajectory goes from the event of emission $A1$ to the reception $B1$. When B receives the signal, its velocity with respect to the Lab frame is higher than the velocity of A at the moment of emission. An analogous situation exists for the second signal, in such a way that the proper time intervals of reception and emission, respectively, are given by,

$$\Delta\tau_r = \tau_{B2} - \tau_{B1}, \quad \Delta\tau_e = \tau_{A2} - \tau_{A1}. \tag{4.5.2}$$

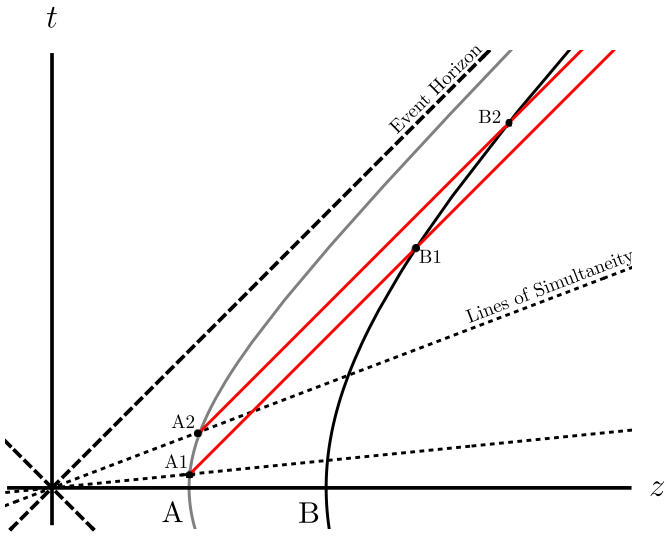

Figure 4.12: This diagram shows, in the Lab frame coordinates (z,t), the world lines (hyperbolas) of two accelerated objects, A and B, the (dotted) lines of simultaneity of the two light rays emitted from A to B, and the trajectories of the two light pulses (in gray). The proper time intervals are seen to be different, $\Delta\tau_r = \tau_{B2} - \tau_{B1} > \Delta\tau_e = \tau_{A2} - \tau_{A1}$.

The (z,t) coordinates in the Lab frame in terms of the proper time τ_i and the acceleration a_i of each accelerated object are

$$z_i = \frac{1}{a_i}\mathrm{Ch}(a_i\tau_i), \quad t_i = \frac{1}{a_i}\mathrm{Sh}(a_i\tau_i), \quad i = A, B. \tag{4.5.3}$$

As each accelerated object is considered the principal observer, their proper positions are $Z_i = 0$.

To determine the redshift we restrict ourselves to a wave moving in the $(+\hat{z})$ direction in a magnetic BI background located in the plane XZ, with the Rindler acceleration being $\vec{a} = a\hat{z}$. The light trajectory, in Minkowski coordinates (t,z), is calculated by integrating the phase velocity in Eq. (4.3.2), $v_{\mathrm{ph}} = \beta = \frac{dz}{dt} = \sqrt{1 - \frac{B_x^2}{b^2+B^2}}$:

$$z - z_0 = \sqrt{1 - \frac{B_x^2}{b^2 + B^2}}(t - t_0) = \beta(t - t_0), \tag{4.5.4}$$

where the phase velocity is denoted by β. When $\beta \to 1$ (zero BI field) the trajectory is that of light in vacuum; this case is examined in [88].

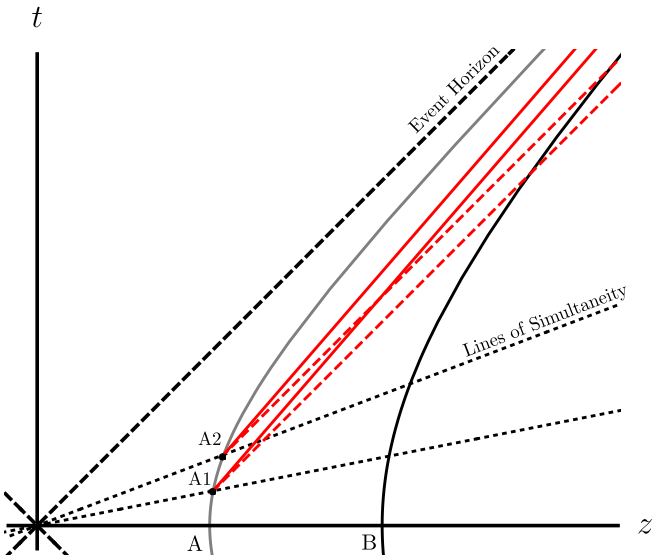

Figure 4.13: The difference between the light rays in vacuum (dashed gray) and the presence of a magnetic BI background (continuous gray) is shown. The difference between the intervals is larger in the presence of the BI field, which means a larger redshift than that due only to the acceleration of the Rindler frame.

Considering that the first light pulse is emitted by A at the initial coordinates $z_0 = z_1$ and $t_0 = t_1$, the trajectory of the light pulse is $z - z_1 = \beta(t - t_1)$, which in Rindler coordinates, Eqs. (4.5.3), becomes

$$z - \frac{1}{a_A}\mathrm{Ch}(a_A\tau_{A1}) = \beta[t - \frac{1}{a_A}\mathrm{Sh}(a_A\tau_{A1})]. \tag{4.5.5}$$

This light ray intersects the world line of B at (z_3, t_3) when the proper time of B is τ_{B1}. Since $t_3 = \mathrm{Sh}(a_B\tau_{B1})/a_B$, then knowing t_3 we can determine τ_{B1}. Solving for t_3 implies solving the system of equations consisting of the hyperbola equation for B and the light trajectory equation, i.e. solving the system

$$z_3^2 = \frac{1}{a_B^2} + t_3^2 \tag{4.5.6}$$

$$z_3 - z_1 = \beta(t_3 - t_1). \tag{4.5.7}$$

From these equations is obtained a quadratic equation for t_3 with solution

$$a_A a_B t_3 = \frac{1}{(\beta^2 - 1)}\left[\beta a_B \chi_1 \pm \sqrt{a_B^2\chi_1^2 + a_A^2(\beta^2 - 1)}\right], \tag{4.5.8}$$

where $\chi_i = a_A(\beta t_i - z_i)$. In terms of the Rindler coordinates for the emitter A, this is

$$\chi_i = a_A(\beta t_i - z_i) = \left[\beta \mathrm{Sh}(a_A \tau_{A1}) - \mathrm{Ch}(a_A \tau_{A1})\right]. \tag{4.5.9}$$

Using t_3 in Rindler coordinates, $t_3 = \mathrm{Sh}(a_B\tau_{B1})/a_B$, we obtain

$$\begin{aligned} \mathrm{Sh}(a_B\tau_{B1}) &= \frac{1}{a_A(\beta^2-1)}\left(\beta a_B \chi_1 \pm \sqrt{a_B^2\chi_1^2 + a_A^2(\beta^2-1)}\right), \to \\ a_B\tau_{B1} &= \mathrm{ArcSh}\left[\frac{1}{a_A(\beta^2-1)}\left(\beta a_B \chi_1 \pm \sqrt{a_B^2\chi_1^2 + a_A^2(\beta^2-1)}\right)\right] \\ &= \mathrm{ArcSh}(g). \end{aligned} \tag{4.5.10}$$

Following the same procedure for the second light ray, we obtain

$$\begin{aligned} \mathrm{Sh}(a_B\tau_{B2}) &= \frac{1}{a_A(\beta^2-1)}\left(\beta a_B \chi_2 \pm \sqrt{a_B^2\chi_2^2 + a_A^2(\beta^2-1)}\right), \to \\ a_B\tau_{B2} &= \mathrm{ArcSh}\left[\frac{1}{a_A(\beta^2-1)}\left(\beta a_B \chi_1 \pm \sqrt{a_B^2\chi_1^2 + a_A^2(\beta^2-1)}\right)\right] \\ &= \mathrm{ArcSh}(f), \end{aligned} \tag{4.5.11}$$

where we have defined f and g as the argument of ArcSh in the right-hand sides of the previous equations. After determining $\Delta\tau_r = \tau_{B2} - \tau_{B1}$ and $\Delta\tau_e = \tau_{A1} - \tau_{A2}$ from the previous expressions, we can measure the redshift of the two light pulses propagating through a BI magnetic background in the Rindler frame using Eq. (4.5.1).

From (4.5.11) and (4.5.10) the proper time interval of the reception of the pulses is

$$a_B(\tau_{B2} - \tau_{B1}) = \mathrm{ArcSh}f - \mathrm{ArcSh}g = \log\frac{\sqrt{f^2+1}+f}{\sqrt{g^2+1}+g}. \tag{4.5.12}$$

Expanding the result for "small" intensities of the field, i.e., neglecting terms of order $(B/b)^4$ and higher,

$$\tau_{B2} - \tau_{B1} \approx \frac{a_A}{a_B}(\tau_{A2} - \tau_{A1}) + \frac{\left(\left(a_A^2 - a_B^2\right)\left(e^{2a_A\tau_{\mathrm{A2}}} - e^{2a_A\tau_{\mathrm{A1}}}\right)\right)}{4a_B^2}\frac{B_x^2}{b^2}. \tag{4.5.13}$$

In this equation, the first term corresponds to the redshift due to the acceleration of the objects, while the second term is the contribution due to the presence of the BI electromagnetic background, which depends on the magnetic BI component that is transversal to the acceleration of the Rindler frame. We can obtain a simpler expression approximating for small

proper times; in this case, we approximate the exponentials as $e^x \approx 1 + x$, neglecting terms $(a_A\tau_A)^2$ and higher:

$$\tau_{B2} - \tau_{B1} \approx \frac{a_A}{a_B}\left(\tau_{A2} - \tau_{A1}\right)\left(1 + \frac{a_A^2 - a_B^2}{2a_B^2}\frac{B_x^2}{b^2}\right), \tag{4.5.14}$$

$$\Delta\tau_B \approx \frac{a_A}{a_B}\Delta\tau_A\left(1 + \frac{a_A^2 - a_B^2}{2a_B^2}\frac{B_x^2}{b^2}\right). \tag{4.5.15}$$

To obtain (4.5.15) in terms of the frequency we note that if A sends a pulse with a proper frequency f_A, A will measure the number of waves per unit of their proper time, while B receives and measures a proper frequency f_B. Since the number of light pulses is the same,

$$f_A\Delta\tau_A = f_B\Delta\tau_B, \tag{4.5.16}$$

then

$$\frac{f_A}{f_B} = \frac{\Delta\tau_B}{\Delta\tau_A} \approx \frac{a_A}{a_B}\left(1 + \frac{a_A^2 - a_B^2}{2a_B^2}\frac{B_x^2}{b^2}\right). \tag{4.5.17}$$

Since the proper accelerations are $a_A/a_B > 1$, and the BI term is always positive, then for the frequencies $f_A/f_B > 1$, and in terms of the redshift parameter $z_R = \frac{f_A}{f_B} - 1$

$$z_R = \frac{a_A}{a_B}\left(1 + \frac{a_A^2 - a_B^2}{2a_B^2}\frac{B_x^2}{b^2}\right) - 1. \tag{4.5.18}$$

Analyzing the redshift expression, we see that there is a loss of energy by the light pulse. This loss is composed of two terms: the first part is used in overcoming the gravitational field (Rindler acceleration), as expected, and the second part is due to the effect of the BI field, i.e., the pulse has to spend additional energy while traveling through the magnetic background, resulting in a larger redshift. Figure 4.14 shows two examples.

Another way of writing the redshift is in terms of the position of the accelerated objects. Considering the coordinate transformation to $(\bar{T}, \bar{Z})$ coordinates

$$\bar{Z} = Z + \frac{1}{a}, \qquad \bar{T} = T, \qquad \bar{X} = X, \qquad \bar{Y} = Y; \tag{4.5.19}$$

the transformation implies that

$$\left\{\begin{array}{c} t \\ z \end{array}\right\} = \bar{Z}\left\{\begin{array}{c} \mathrm{Sh}a\bar{T} \\ \mathrm{Ch}a\bar{T} \end{array}\right\} \rightarrow \begin{array}{c} \bar{Z} = \sqrt{z^2 - t^2} \\ \bar{T} = \frac{1}{a}\mathrm{ArcTh}(\frac{t}{z}); \end{array} \tag{4.5.20}$$

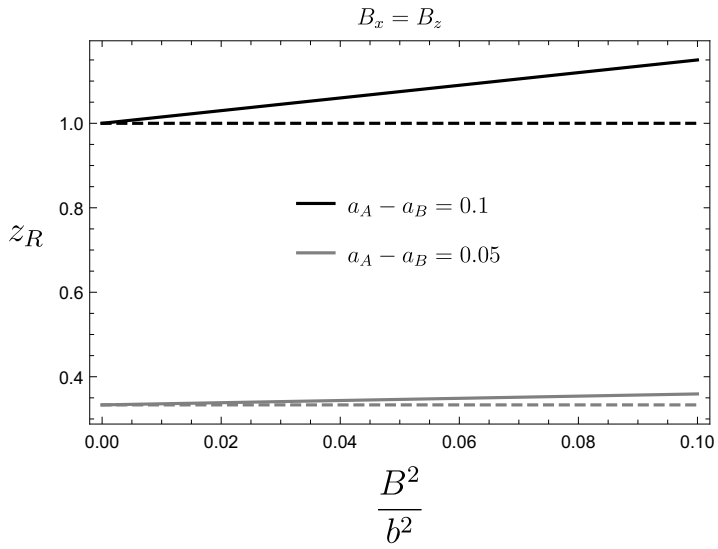

Figure 4.14: The redshift in Eq. (4.5.18) is plotted with respect to the intensity of the BI magnetic background, for two different proper acceleration differences between the emitter (A) and the receiver (B). As the difference becomes smaller, the resulting redshift is also smaller. The dashed lines represent the pure Rindler effect, i.e., the one corresponding to a vanishing BI magnetic background, while the continuous lines account for the total redshift. The difference between the two lines (continuous minus dashed) corresponds to the BI redshift. In the plot the magnetic components are of the same magnitude, $B_x = B_z$.

while the Rindler metric takes the form $ds^2 = a^2\bar{Z}^2 d\bar{T}^2 - d\bar{Z}^2 - d\bar{X}^2 - d\bar{Y}^2$. In these coordinates, the event horizon is at $\bar{Z} = 0$.

To calculate the redshift, we write the proper coordinates of the emitter (A) and the receiver (B) as:

$$A : \{\bar{\tau}_A, \bar{Z}_A = \frac{1}{a_A}\}, \qquad B : \{\bar{\tau}_B, \bar{Z}_B = \frac{1}{a_B}\} \tag{4.5.21}$$

Note that now the proper position of the accelerated objects is at $\bar{Z}_i = 1/a_i$. The Minkowski coordinates corresponding to the positions of emission and reception of the light pulses are Eqs. (4.5.3). We can then determine the redshift analogously and Eq. (4.5.18) can be written in terms of $(\bar{T}, \bar{Z})$ as

$$z_R = \frac{\bar{Z}_B}{\bar{Z}_A}\left(1 + \frac{\bar{Z}_B}{\bar{Z}_A}\frac{B_x^2}{2b^2}\right) - 1. \tag{4.5.22}$$

Figure 4.15 shows the redshift as a function of the receiver position for a fixed emitter at

different field intensities.

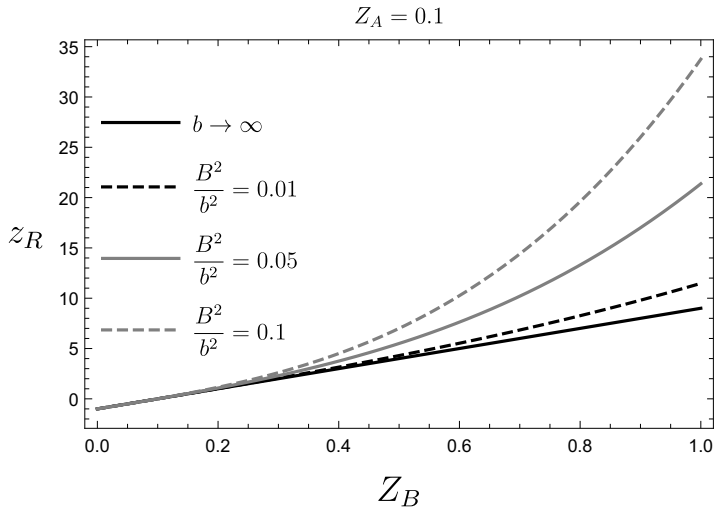

Figure 4.15: The redshift in Eq. (4.5.22) is plotted with respect to the proper coordinates of the receiver Z_B, for different values of the intensity of the BI field. The redshift increases as the intensity of the field increases. In this plot $Z_a = 0.1$. The redshift is larger for greater distances between the receiver and the emitter.

4.6 Conclusions

We study an electromagnetic wave propagating through an intense uniform BI background and determine the phase velocities using the effective optical metric as measured by an accelerated observer.

Our treatment is valid for strong fields; if we consider, for instance, that $B^2/b^2 \approx 10^{-2}$, where b is the maximum attainable electromagnetic field, then the BI field is of the order of 10^{19}V m^{-1} that is ten times the critical Schwinger field or $B_{\rm cr} \approx 10^9$ Tesla. The phase velocities depend on the product of the acceleration of the frame times the time coordinate, (aT), such that the effect of increasing the acceleration is the same as that of time elapsing. If the magnetic field component transversal to the acceleration vanishes, then there is no effect on the phase velocity of either the acceleration or the BI field, and its value is that in vacuum.

Since the accelerated frame is no longer inertial, no special relativity velocity invariance is expected.

Then it was examined a wave propagating through an intense electric field background, turning out that the effect of the BI electric field (decreasing the phase velocity) is qualitatively very similar to the one of the BI magnetic background. For strong fields, when B approaches the maximum attainable BI field b, the most effective for slowing down the phase velocity is the electric background, for all propagating directions of the light rays.

We analyzed the redshift of a light pulse sent from one Rindler observer and received by another one when the light pulses travel through the BI magnetic background. In the approximation of small fields and small intervals of time, we found an expression for the redshift and distinguished two contributions, one due to the acceleration of the frame and the other produced by the presence of the BI magnetic background, resulting in a larger total redshift.

In summary, we have analyzed the phase velocity of light propagating under the effect of a very intense magnetic or electric BI field as measured by an accelerated (Rindler) observer. According to the Einstein Equivalence principle (EEP), the situation is equivalent to the measurements by an observer under the influence of a uniform gravitational field.

E. Guzman-Herrera, N. Breton,
"Light Propagating in a Born–Infeld Background as Seen by an Accelerated Observer"
Annalen Der Physik, **534**, 2200043 (2022).
DOI 10.1002/andp.202200043

Chapter 5

Light propagation in the vicinity of a ModMax black hole

Recently in [61] was proposed a NLED theory that shares the two symmetries of Maxwell's equations: the four-dimensional conformal symmetry and the electric-magnetic duality. It is known as Modified Maxwell (ModMax) NLED and is characterized by a dimensionless parameter γ that in the limit $\gamma = 0$ reduces to Maxwell theory. ModMax theory has stimulated research in several aspects, from classical solutions [62], [63] to super symmetric analysis [64]–[71].

Coupling the ModMax NLED with Einstein gravity, for a static and spherically symmetric (SSS) metric, black hole (BH) solutions were found [93]. In the present chapter, we focus on light propagation in the neighborhood of a ModMax BH, determining light trajectories as the null geodesics of the effective metric.

5.1 ModMax Nonlinear electrodynamics.

The ModMax NLED possesses both Maxwell's symmetries, conformal invariance and SO(2) duality-rotation invariance. The ModMax NLED Lagrangian was derived in [94] using the Bessel-Hagen criterion for conformal invariance, and the Gaillard–Zumino one for invariance

under duality transformations. In [61] the symmetries of the theory are deduced by means of the Hamiltonian formalism and it is demonstrated that there are only two theories that share the same symmetries than Maxwell's, the Bialynicki-Birula (BB) and the ModMax. Considering that the Hamiltonian depends on two parameters, one with dimensions of energy density (T) and the other being the dimensionless parameter γ, the BB theory is the generalization for strong fields ($T \to 0$) and cannot be written in Lagrangian form [61]. The ModMax theory is the generalization for weak fields ($T \to \infty$) and Maxwell's theory is recovered when the nonlinear parameter γ vanishes.

The ModMax Lagrangian is given by

$$L_{\text{ModMax}} = -\frac{F}{4}\cosh\gamma + \frac{\sinh\gamma}{4}\sqrt{F^2+G^2}, \tag{5.1.1}$$

where F and G are the electromagnetic Lorentz invariants; the Maxwell Lagrangian [95], $L_{\text{M}} = -\frac{F}{4}$, corresponds to the vanishing of the nonlinear parameter $\gamma = 0$ (specifics of the ModMax theory can be found in [94], [96], [97]). The birefringence indices λ_a in Eq. (2.1.6), for the ModMax Lagrangian, Eq. (5.1.1), are

$$\lambda_1 = \frac{L_{FF} + L_{GG}}{L_F + 2\left(GL_{FG} - FL_{GG}\right)}, \qquad \lambda_2 = 0, \tag{5.1.2}$$

or in terms of γ and the electromagnetic invariants F and G,

$$\lambda_1 = \frac{4\tanh\gamma}{\sqrt{F^2+G^2} + F\tanh\gamma}, \qquad \lambda_2 = 0. \tag{5.1.3}$$

The effective metric $g^{\mu\nu}_{\text{eff}(1)}$ from Eq. (2.1.8) is given by

$$g^{\mu\nu}_{\text{eff}(1)} = g^{\mu\nu} + \frac{4\tanh\gamma}{\sqrt{F^2+G^2} + F\tanh\gamma}t^{\mu\nu}. \tag{5.1.4}$$

As a consequence of the conformal invariance one of the birefringence index vanishes, $\lambda_2 = 0$, then the corresponding effective metric coincides with the background metric,

$$g^{\mu\nu}_{\text{eff}(2)} = g^{\mu\nu}, \tag{5.1.5}$$

this means that one of the polarization modes follows the null geodesics of the background metric, with the dispersion relation given by $\omega^2 = |\vec{k}|^2$. It is important to highlight that this

result does not imply the absence of birefringence as in the case of the BI theory. The two paths followed by photons are established by $g^{\mu\nu}_{\text{eff}(1)}$ and, coincidentally, by the background metric $g^{\mu\nu}$.

The existence of two effective metrics corresponds to the birefringence effect, i.e. there are two possible paths that light rays can follow, depending on their polarization. In case $\gamma = 0$ we recover one single effective metric for the propagation of electromagnetic waves $g^{\mu\nu}_{\text{eff}(1)} = g^{\mu\nu} = g^{\mu\nu}_{\text{eff}(2)}$.

Let us consider a vanishing electric field and a uniform magnetic field $\vec{B}$ in Minkowski spacetime $g^{\mu\nu} = \eta^{\mu\nu}$, then the dispersion relation amounts to

$$\omega^2 = k^2(\cos^2\phi + \mathrm{e}^{-2\gamma}\sin^2\phi), \tag{5.1.6}$$

where ϕ is the angle between the propagation direction $\vec{k}$ and the magnetic field, $\vec{B}$. There is no birefringence when $\phi = 0$ because in this case, the background preserves the rotational symmetry in the plane defined by $\vec{k}$ [61]. This equation also indicates that superluminal velocities are reached for negative values of the nonlinear parameter γ; therefore to avoid superluminal velocities we should restrict to $\gamma \geq 0$.

In case the effective metric is diagonal, the two-phase velocities, from Eq. (2.2.3), are

$$(v_1)^2 = \left(\frac{\omega}{|\vec{k}|}\right)^2_{(1)} = -\frac{g^{ij} + \lambda_1 t^{ij}}{g^{tt} + \lambda_1 t^{tt}}\tilde{k}_i\tilde{k}_j, \tag{5.1.7}$$

$$(v_2)^2 = \left(\frac{\omega}{|\vec{k}|}\right)^2_{(2)} = -\frac{g^{ij}}{g^{tt}}\tilde{k}_i\tilde{k}_j. \tag{5.1.8}$$

In the next section, we present the ModMax NLED BH and analyze several aspects of light propagation in its vicinity.

5.2 ModMax black hole

In [93] was derived the static spherically symmetric (SSS) solution to the Einstein equations coupled to ModMax NLED; it is characterized by the BH mass, BH charge, and the nonlinear

parameter γ; its line element is given by

$$ds^2 = g_{\mu\nu}dx^\mu dx^\nu = -f(r)dt^2 + \frac{1}{f(r)}dr^2 + r^2 d\Omega, \quad f(r) = 1 - \frac{2M}{r} + \frac{e^{-\gamma}Q^2}{r^2}, \tag{5.2.1}$$

where $d\Omega = d\theta^2 + \sin^2\theta d\phi^2$; the charge can be electric $Q = Q_e$, magnetic $Q = Q_m$, or both (Dyonic case) $Q = \sqrt{Q_e^2 + Q_m^2}$, [93]. This metric represents a charged BH with horizons defined by the roots of $f(r) = 0$,

$$r_+ = M + \sqrt{M^2 - e^{-\gamma}Q^2}, \quad r_- = M - \sqrt{M^2 - e^{-\gamma}Q^2}. \tag{5.2.2}$$

There exists an event horizon r_+ if the condition $0 \leq Q^2 e^{-\gamma} \leq M^2$ is fulfilled. We shall consider $g_{\mu\nu}$ in Eq. (5.2.1) as the background metric. Recalling the metric function for the Reissner-Nordstrom (RN) BH, the SSS of the Einstein-Maxwell equations,

$$f_{RN}(r) = 1 - \frac{2M}{r} + \frac{Q^2}{r^2}, \tag{5.2.3}$$

note that the ModMax metric function $f(r)$ resembles the RN one with a screened charge, $Q^2 \to e^{-\gamma}Q^2$ In the RN BH the charge is restricted to $Q^2 \leq M^2$, while the ModMax BH can bear a larger charge, $Q^2 \leq e^{\gamma}M^2$, due to the charge screening.

Since the nonvanishing components of the electromagnetic tensor are $F_{rt} = Q_e/r^2$ and $F_{\phi\theta} = Q_m \sin\theta$, the tensor $t^{\mu\nu}$ in Eq. (5.1.4) is given by

$$t^{\mu\nu} = F^{\mu\lambda}F_\lambda{}^\nu = \text{diag}\left[-\frac{F_{tr}^2}{f(r)}, f(r)F_{tr}^2, -\frac{F_{\phi\theta}^2}{r^6}, -\frac{F_{\phi\theta}^2}{r^6}\right]. \tag{5.2.4}$$

In Fig. 5.1 we compare the metric functions $f(r)$ of the Schwarszchild, the RN, and the ModMax BHs. The radius of the ModMax BH event horizon is larger than the RN one and smaller than Schwarszchild's. The ModMax BH is singular at $r = 0$, i.e. its curvature scalars diverge at $r = 0$.

In the next subsections, we analyze light trajectories in the vicinity of the ModMax BH, by calculating the null geodesics of the effective metrics.

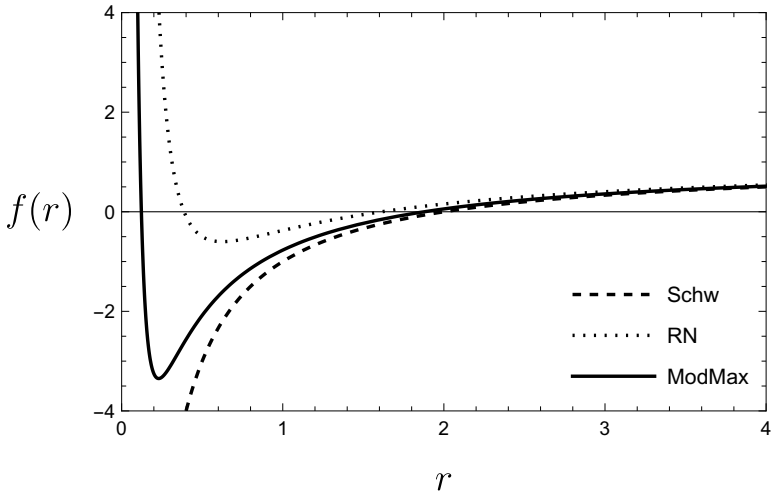

Figure 5.1: The metric functions $f(r)$ of Schwarszchild, RN and ModMax BHs are shown. The radii of the event horizons are the intersections of the corresponding metric functions with the $r-$axis: the radius of the event horizon for the ModMax BH is larger than the RN one and smaller than Schwarszchild's. In this plot, we fixed the BH parameters as $Q = 0.8$, $\gamma = 0.5$, $M = 1$.

5.2.1 Phase velocities in the vicinity of ModMax Black hole

Our aim in this subsection is to determine the phase velocities of light propagating near the ModMax BH. Without loss of generality, we consider equatorial trajectories of light, $\theta = \pi/2$. Then considering the tensor $t^{\mu\nu}$ in Eq. (5.2.4), the effective metrics, Eqs. (5.1.4) and (5.1.5), are given by

$$g^{\mu\nu}_{\text{eff}(1)} = \frac{Q^2}{e^{-\gamma}Q_e^2 + e^{\gamma}Q_m^2}\text{diag}\left[-e^{\gamma}f(r)^{-1}, e^{\gamma}f(r), \frac{e^{-\gamma}}{r^2}, \frac{e^{-\gamma}}{r^2}\right], \tag{5.2.5}$$

$$g^{\mu\nu}_{\text{eff}(2)} = g^{\mu\nu} = \text{diag}\left[-f(r)^{-1}, f(r), \frac{1}{r^2}, \frac{1}{r^2}\right], \tag{5.2.6}$$

where $f(r) = 1 - \frac{2M}{r} + \frac{e^{-\gamma}Q^2}{r^2}$, $Q^2 = Q_e^2 + Q_m^2$; and we have used the birefringence indices, that for the ModMax BH, are,

$$\lambda_1 = \frac{2e^{\gamma}r^4\sinh\gamma}{e^{2\gamma}F_{\phi\theta}^2 + r^4F_{rt}^2} = \frac{2r^4\sinh\gamma}{e^{-\gamma}Q_e^2 + e^{\gamma}Q_m^2}, \quad \lambda_2 = 0. \tag{5.2.7}$$

Note that both metrics are diagonal, then the expression of the phase velocity simplifies. Considering the propagation along radial and ϕ-angular directions, with a wave vector given

by $\tilde{k}_\mu = (\omega, 1, 0, 1)$, using Eq. (2.2.3)

$$\left(v^{r\phi}\right)_a = \pm\sqrt{-\frac{g^{rr}_{\text{eff}(a)}\tilde{k}_r^2 + g^{\phi\phi}_{\text{eff}(a)}\tilde{k}_\phi^2}{g^{tt}_{\text{eff}(a)}}}, \qquad a = 1, 2 \tag{5.2.8}$$

Then, for the two values of $\lambda_{1,2}$ in Eq. (5.1.3) the corresponding phase velocities are

$$v_1^{r\phi} = \sqrt{f(r)\left(f(r) + \frac{e^{-2\gamma}}{r^2}\right)}, \tag{5.2.9}$$

$$v_2^{r\phi} = \sqrt{f(r)\left(f(r) + \frac{1}{r^2}\right)}. \tag{5.2.10}$$

For light propagating in a purely radial direction, (ϕ and θ fixed), the two-phase velocities turn out to be equal, then there is no birefringence. From Eq. (5.1.7),

$$v^r_{1,2} = f(r). \tag{5.2.11}$$

The light phase velocity in the neighborhood of the ModMax BH is always less than the one corresponding to RN BH, $v^r_{RN} > v^r_{1,2}$. If $v^r = 0$ the orbits are circular and, if $\theta = \pi/2$, the light ray stays in the equatorial plane, however, these are unstable circular orbits (UCO). If the wave vector has angular components k^θ or k^ϕ, then there is birefringence, $v_1^i \neq v_2^i$,

θ-direction, $i = \theta$:

$$v_1^\theta = \frac{\mathrm{e}^{-\gamma}}{r}\sqrt{f(r)}, \qquad v_2^\theta = \frac{1}{r}\sqrt{f(r)}, \tag{5.2.12}$$

ϕ-direction, $i = \phi$:

$$v_1^\phi = \frac{\mathrm{e}^{-\gamma}}{r\sin\theta}\sqrt{f(r)}, \qquad v_2^\phi = \frac{1}{r\sin\theta}\sqrt{f(r)}. \tag{5.2.13}$$

In Figure 5.2 we compare the phase velocities in equatorial orbits. The phase velocities depend on the BH charge Q through the metric function $f(r)$ and the occurrence of birefringence is independent of whether the BH is electrically or magnetically charged. The effect of the nonlinear parameter γ is to reduce the phase velocities.

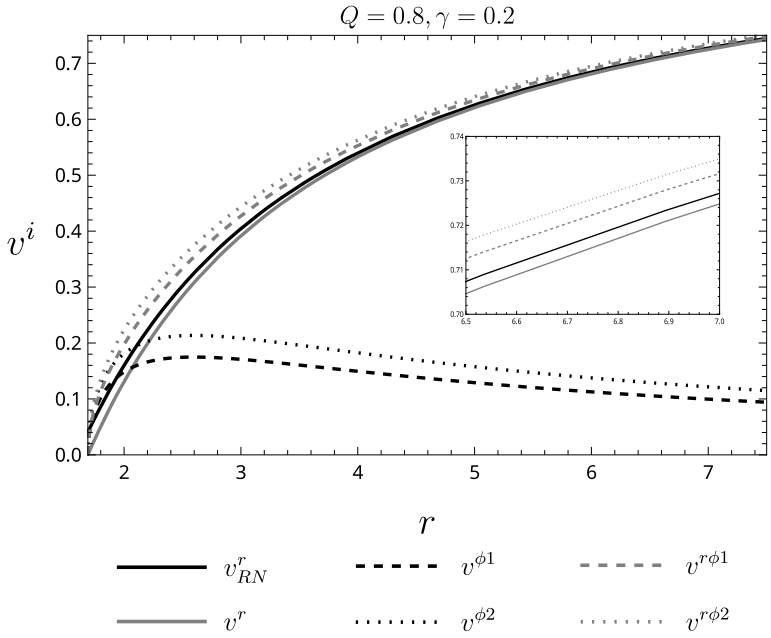

Figure 5.2: The radial and ϕ-angular phase velocities corresponding to the two effective metrics are shown. Measured by a distant observer, starting from infinity with velocity $c = 1$, as light approaches the horizon its phase velocity tends to zero. There is no birefringence in the radial direction; if the wave vector has angular components then there is birefringence. The gray curve is the phase velocity in the radial direction. The black dotted and dashed curves correspond to the phase velocity in purely ϕ-direction $v^{\phi 2}$, $v^{\phi 1}$ with $v^r = 0$. The gray dashed curve corresponds to the phase velocity $v^{r\phi}$ considering that the light propagates along radial and ϕ-angular directions. The phase velocities in the neighborhood of the RN BH (black solid curve for the radial direction, angular directions are not shown) are always greater than the ones for the ModMax BH. We fixed the BH parameters as $Q = 0.5$, $\gamma = 0.2$, $M = 1$.

5.2.2 Light trajectories, null Geodesics, and orbits around the ModMax Black hole.

We consider the Hamiltonian formalism and the conserved quantities for a test particle to obtain the equations of motion of a photon in the external field of a BH. In a SSS spacetime, due to the existence of two Killing vectors, a test particle has two conserved quantities, its

energy, and its angular momentum.

$$E = g_{tt}\frac{dt}{d\tau}, \qquad L = g_{\phi\phi}\frac{d\phi}{d\tau}. \tag{5.2.14}$$

where τ is the affine parameter along a geodesic. Without loss of generality, we consider equatorial orbits, $\theta = \pi/2$. Then from the mass invariance, $g_{\mu\nu}\dot{x^\mu}\dot{x^\nu} = \delta$, and making a distinction between the background metric and the effective metric,

$$\left(\frac{dr}{d\tau}\right)^2 + \frac{1}{g_{rr}^{\text{eff}(a)}}\left(g_{\phi\phi}^{\text{eff}(a)}\left(\frac{L}{g_{\phi\phi}}\right)^2 + g_{tt}^{\text{eff}(a)}\left(\frac{E}{g_{tt}}\right)^2 - \delta\right) = 0, \tag{5.2.15}$$

where $\delta = 1, 0, -1$ for space-like, null, or time-like geodesics, respectively; denoting $\dot{r} = dr/d\tau$ and the impact parameter $b = L/E$, the previous equation is

$$\dot{r}^2 + \frac{L^2}{g_{rr}^{\text{eff}(a)}}\left(\frac{g_{\phi\phi}^{\text{eff}(a)}}{r^4} + \frac{g_{tt}^{\text{eff}(a)}}{f^2(r)}\frac{1}{b^2} - \frac{\delta}{L^2}\right) = 0, \tag{5.2.16}$$

and $a = 1, 2$ denote the two effective metrics. Considering $\dot{r}^2 + V_{\text{eff}}^{(a)} = 0$, we identify the effective potential as

$$V_{\text{eff}}^{(a)} = \frac{L^2}{g_{rr}^{\text{eff}(a)}}\left(\frac{g_{\phi\phi}^{\text{eff}(a)}}{r^4} + \frac{g_{tt}^{\text{eff}(a)}}{f^2(r)}\frac{1}{b_a^2} - \delta\right). \tag{5.2.17}$$

The radius of the circular orbits r_c corresponds to an extreme of the effective potential,

$$V_{\text{eff}}^{(a)} = 0, \quad \frac{dV_{\text{eff}}^{(a)}}{dr} = 0, \tag{5.2.18}$$

and since we are focusing on light ray propagation, that corresponds to the null geodesics of the effective metric, we only study the case $\delta = 0$. We obtain the radius of the circular orbits r_c as

$$r_c = \frac{3M}{2}\left(1 \pm \sqrt{1 - \frac{8e^{-\gamma}Q^2}{9M^2}}\right). \tag{5.2.19}$$

There are two impact parameters, b_c^a, corresponding to the two effective metrics, given by

$$\left(b_c^2\right)_a = \left(-\frac{r_c^4 g_{tt}^{\text{eff}(a)}}{f^2(r_c) g_{\phi\phi}^{\text{eff}(a)}}\right)_{r_c}, \qquad a = 1, 2 \tag{5.2.20}$$

or explicitly,

$$b_{c1}^2 = \frac{e^{-2\gamma}r_c^2}{f(r_c)}, \qquad b_{c2}^2 = \frac{r_c^2}{f(r_c)}. \tag{5.2.21}$$

From Eq. (5.2.16) and $\dot{\phi} = L/g_{\phi\phi}$ we can write the equation for the light trajectories in the $r-\phi$ plane, $\phi_a(r)$,

$$\left(\frac{dr}{d\phi}\right)^2_a = \left(\frac{\dot{r}}{\dot{\phi}}\right)^2_a = -\frac{1}{g_{rr}^{\text{eff}(a)}}\left(g_{\phi\phi}^{\text{eff}(a)} + g_{tt}^{\text{eff}(a)}\frac{r^4}{f^2(r)}\frac{1}{b_c^2}\right) \tag{5.2.22}$$

and using the value of the critical impact parameters b_{ca}, Eq. (5.2.20)

$$\left(\frac{dr}{d\phi}\right)^2_a = -\frac{g_{\phi\phi}^{\text{eff}(a)}}{g_{rr}^{\text{eff}(a)}}\left(1 - \frac{g_{tt}^{\text{eff}(a)}}{g_{\phi\phi}^{\text{eff}(a)}}\left(\frac{g_{\phi\phi}^{\text{eff}(a)}}{g_{tt}^{\text{eff}(a)}}\right)_{r_c}\frac{r^4}{r_c^4}\frac{f^2(r_c)}{f^2(r)}\right), \tag{5.2.23}$$

where $f(r)$ is given in Eq. (5.2.1). Following a standard procedure to integrate the previous equation [98], the r coordinate is transformed as $r = 1/u$. In our case there are two possible trajectories of the photon $\phi_a(r)$, $a = 1, 2$; for $\phi_1(r)$ we have

$$\left(\frac{du}{d\phi_1}\right)^2 = e^{2\gamma}(u-u_c)^2\left[2u\left(M - e^{-\gamma}Q^2u_c\right) + u_c\left(M - e^{-\gamma}Q^2u_c\right) - e^{-\gamma}Q^2u^2\right], \tag{5.2.24}$$

where $u_c = 1/r_c$. Then it has to be integrated

$$\mathrm{e}^{\gamma}d\phi_1 = \pm\int\frac{d\xi}{\sqrt{-e^{-\gamma}Q^2 + c_1\xi + c_2\xi^2}} \tag{5.2.25}$$

where

$$\xi = \frac{1}{u-u_c}, \quad c_1 = 2(M - 2e^{-\gamma}Q^2u_c), \quad c_2 = u_c\left(3M - e^{-\gamma}Q^2u_c\right), \tag{5.2.26}$$

and u_c corresponding to r_c in Eq. (5.2.19) is

$$u_c = \frac{3M}{4e^{-\gamma}Q^2}\left(1 - \sqrt{1 - \frac{8e^{-\gamma}Q^2}{9M^2}}\right). \tag{5.2.27}$$

The solutions for $\phi_1(r)$ depend on the sign of c_2,

$$(\phi_1)_\pm = \mp\mathrm{e}^{-\gamma}\left(\frac{1}{\sqrt{c_2}}\ln\left(c_1 + 2c_2\xi + 2\sqrt{c_2}\sqrt{-e^{-\gamma}Q^2 + c_1\xi + x\xi^2}\right)\right), \quad c_2 > 0 \tag{5.2.28}$$

$$(\phi_1)_\pm = \mp\mathrm{e}^{-\gamma}\left(-\frac{1}{\sqrt{c_2}}\arcsin\left(\frac{2c_2\xi + c_1}{\sqrt{4e^{-\gamma}Q^2c_2 + c_1^2}}\right)\right), \quad c_2 < 0 \tag{5.2.29}$$

where the $\pm$ sign corresponds to the angle measured counterclockwise or clockwise, respectively and $\xi = \frac{rr_c}{r_c - r}$; we consider the positive solution because the constriction $c_2 > 0$ agrees with the value of u_c in Eq. (5.2.27).

We can clear out $r(\phi)$ from Eq. (5.2.28),

$$r_1(\phi_1) = \frac{\left(\left(c_1 - \text{Exp}(\pm \text{e}^{\gamma}\sqrt{c_2}\phi)\right)^2 + 4c_2 e^{-\gamma}Q^2\right) r_c}{\left(\left(c_1 - \text{Exp}(\pm \text{e}^{\gamma}\sqrt{c_2}\phi)\right)^2 + 4c_2 e^{-\gamma}Q^2\right) + 4c_2 r_c \text{Exp}(\pm \text{e}^{\gamma}\sqrt{c_2}\phi)}, \qquad c_2 > 0 \quad (5.2.30)$$

Following an analogous procedure, we determine the second photon trajectory, $\phi_2(r)$, corresponding to the second effective metric, as

$$\phi_2(r) = \mp\left(\frac{1}{\sqrt{c}}\ln\left(c_1 + 2c_2\xi + 2\sqrt{c_2}\sqrt{-e^{-\gamma}Q^2 + c_1\xi + c_2\xi^2}\right)\right), \quad c_2 > 0 \quad (5.2.31)$$

$$\phi_2(r) = \mp\left(-\frac{1}{\sqrt{c_2}}\arcsin\left(\frac{2c_2\xi + c_1}{\sqrt{4e^{-\gamma}Q^2c_2 + c_1^2}}\right)\right), \quad c_2 < 0 \quad (5.2.32)$$

and the trajectory r_2 as a function of ϕ_2 is

$$r_2(\phi_2) = \frac{\left(\left(c_1 - \text{Exp}(\pm\sqrt{c_2}\phi)\right)^2 + 4c_2 e^{-\gamma}Q^2\right) r_c}{\left(c_1 - \text{Exp}(\pm\sqrt{c_2}\phi)\right)^2 + 4c_2\left(e^{-\gamma}Q^2 + r_c\text{Exp}(\pm\sin\theta\sqrt{c_2}\phi)\right)}. \quad (5.2.33)$$

The expression for the latter trajectory, $r_2(\phi_2)$, is identical to the one in the vicinity of an RN BH, but for a reduced charge, $Q \mapsto Qe^{-\gamma/2}$; this orbit is as well the one corresponding to the massless test particles. In Fig. 5.3 we show radial orbits for the ModMax, RN, and Schwarzschild BHs. The trajectory corresponding to the metric $g_{\mu\nu}^{\text{eff}(2)}$, that coincides with the background metric lies between the Schwarzschild and RN trajectories, this is because the only difference with RN BH is the charge screening. In contrast, the null geodesics of $g_{\mu\nu}^{\text{eff}(1)}$, have larger radius, then the traveled distance before crossing the horizon is also larger. As γ increases the screening of the charge increases and the orbit approaches the one in Schwarzschild BH, this is, the unstable circular orbit of radius $3M$ characteristic of the Schwarzschild BH photosphere.

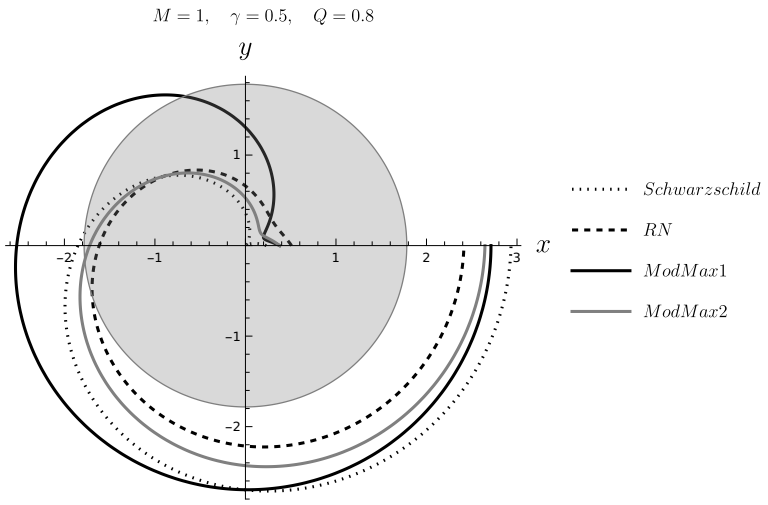

Figure 5.3: Photon trajectories in the vicinity of the Schwarzschild (dotted), RN (dashed), and ModMax (solid) BHs are shown. The gray circumference indicates the ModMax event horizon; the trajectories inside the event horizon are not considered in our study. The trajectory of the effective metric that coincides with the background ModMax metric lies between the Schwarzschild and the RN ones. In this plot are fixed $M = 1$, $Q = 0.8$, $\gamma = 0.5$.

5.2.3 Lensing and deflection angle

Gravitational lensing is a relativistic phenomenon consisting of the deflection of light rays in the vicinity of a massive object; it can be used to survey massive dark objects both in weak and strong gravitational fields. Many aspects of this effect produced by BH have been reported in the literature: the exact lens equation for the Einstein-Euler-Heisenberg static black hole [99], the RN BH and RN-de Sitter BH lensing [100], [101], the lensing in the strong field limit [102]–[104] and the gravitational lensing of massive particles in RN BH [105]. Recently the study of the lensing and the shadow of the ModMax BH was presented in [70], where the massless particle trajectories are determined from the background metric; such that their results correspond to ours for the effective metric that coincides with the BH metric, $g_{\mu\nu}^{\text{eff}(2)} = g_{\mu\nu}$. Therefore the deflection of light calculated from the effective metric $g_{\mu\nu}^{\text{eff}(1)}$ complement the results in [70]. Moreover, in the weak field limit, we present a more precise expression for the deflection angle including terms of higher order in Q. The results

in [70] for the weak deflection angle and the Einstein ring of the ModMax BH are compared with the data obtained from Sagittarius A^*(Sgr A^*) and M87*, then they can be a reference for ours as well.

The expression for the deflection angle α produced by the presence of a BH acting like a lens in the light trajectory, given in terms of the distance of closest approach, denoted by r_0, is

$$\alpha(r_0) = I(r_0) + \varphi_O - \varphi_S \tag{5.2.34}$$

where the angles $\varphi_O - \varphi_S$ are illustrated in Fig. 5.4 and $I(r_0)$ is calculated from the orbit Eq. (5.2.23) considering that the observer and the source are in the same plane of a flat space-time region and that the source of light is located at infinity, $I(r_0) = 2\Delta\phi = 2\left[\phi(r \mapsto \infty) - \phi(r_0)\right]$, [106], and $I(r_0)$ is given by

$$I_a(r_0) = 2\int_{r_0}^{\infty} \left(\frac{d\phi_a}{dr}\right) dr, \quad a = 1, 2. \tag{5.2.35}$$

where $\left(\frac{d\phi}{dr}\right)$ can be derived from Eq. (5.2.23).

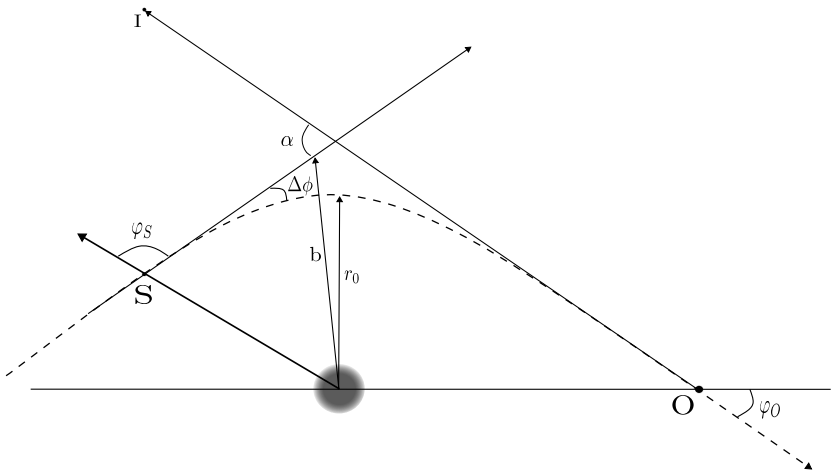

Figure 5.4: The diagram shows the light deflection angle α, the position of the source and of the observer, S and O, respectively. b is the impact parameter and r_0 the distance of closest approach. The gray circle indicates the position of the BH acting as a lens.

If the trajectory were a straight line as in Minkowski spacetime, there would be no deflection and $\varphi_O - \varphi_S = -\pi$, but the presence of the BH bends light's trajectory and $\varphi_O - \varphi_S \neq -\pi$

and to determine the difference we need to calculate the limit $r_0 \to \infty$ in Eq. (5.2.35), making $I_{r_0} = 0$. For the effective metrics in consideration, we obtain two deflection angles, α_1, α_2, that are given by

$$\alpha_1(r_0) = I_1(r_0) = e^{-\gamma}\left\{\int_{r_0}^{\infty} \frac{2}{r\sqrt{\frac{r^2}{r_0^2}f(r_0) - f(r)}}dr - \pi\right\} = e^{-\gamma}\alpha_2. \tag{5.2.36}$$

To integrate $I_{r_0} = 0$ we transform to the variable z, $z = 1 - \frac{r_0}{r}$ obtaining

$$I_1(r_0) = e^{-\gamma}\int_0^1 2\left(f(r_0) - (1-z)^2\left(1 - \frac{2M}{r_0}(1-z) + \frac{Q^2(1-z)^2}{r_0^2}\right)\right)^{-1/2} dz. \tag{5.2.37}$$

In Fig. 5.5 are shown the deflection angles produced by effective metric $g_{\mu\nu}^{\text{eff}(1)}$ of the ModMax BH, varying the nonlinear parameter γ and the BH charge; the integration was numerical.

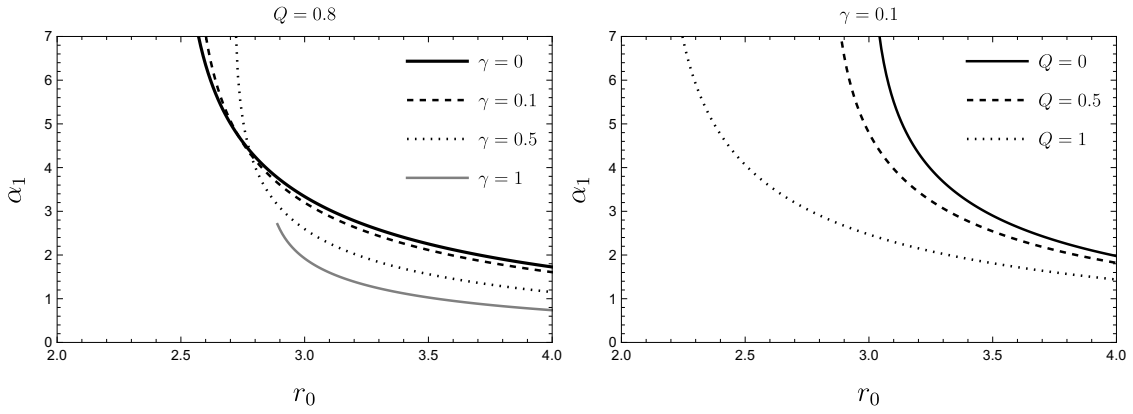

Figure 5.5: The deflection angles α_1 corresponding to $g_{\mu\nu}^{\text{eff}(1)}$ as a function of the distance of closest approach, r_0, for different values of the ModMax nonlinear parameter γ and the BH charge Q are shown. α_2 is larger than α_1, $\alpha_2 = e^{\gamma}\alpha_1$. The case $\gamma = 0$ corresponds to RN BH and $Q = 0$ corresponds to Schwarzschild's deflection angle. We are taking $M = 1$.

For fixed Q and r_0, increasing γ diminishes the deflection angle α and the effect is the same, for fixed γ and r_0, increasing the BH charge. The expression for $I_2(r_0)$ has the same form as for RN but with a charge screened by a factor $e^{-\gamma}$. In Fig. 5.6 we compare the deflection angle $\alpha_i, i = 1, 2$ of the two effective metrics with the RN one. When $r_0 \to r_c$, the

deflection angle reaches values greater than 2π, in this case, the light ray turns around several times before either escaping the photosphere region or falling into the BH [100].

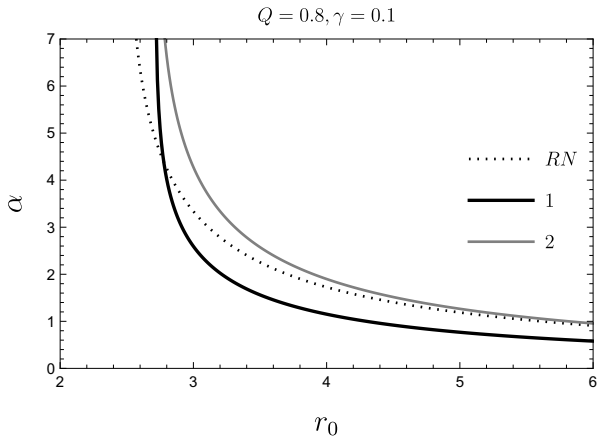

Figure 5.6: The deflection angles α_1 and α_2 for the two effective metrics and the corresponding to the RN-BH are shown. The relative magnitudes of the deflection angles for $r_0 > 3M$ is $\alpha_1 < \alpha_{RN} < \alpha_2$ and $\alpha_1 = e^{-\gamma}\alpha_2$. We are taking $M = 1$.

5.2.4 The weak field limit of the deflection angle

The weak field limit deals with small deflection angles that can be determined through the Gaussian curvature and using the Gauss-Bonnet theorem with the optical metric method (details can be consulted in [107], [108]).

The Gauss-Bonnet theorem connects the differential geometry of a surface with its topology, and the expression for a slight variation of the deflection angle $\delta\alpha$ is given by

$$\delta\alpha = -\int\int_D K dS, \tag{5.2.38}$$

where K is the Gaussian curvature and $dS = \sqrt{-g}drd\phi$, with g being the determinant of the surface metric; the range of integration is $r : \frac{b}{\sin\phi} < r < \infty$ and $\phi : 0 < \phi < \pi$, with b being the impact parameter. The Gaussian curvature is $K = R/2$, being R the Ricci scalar, and for the ModMax BH it is

$$K = \frac{2M}{r^3} - \frac{3M^2 + 3e^{-\gamma}Q^2}{r^4} + \frac{6e^{-\gamma}MQ^2}{r^5} - \frac{2e^{-2\gamma}Q^4}{r^6}. \tag{5.2.39}$$

The determinants of the effective metrics, $\det(g^{\mu\nu}_{\text{eff}(a)}) = g_a$, are

$$g_1 = -\frac{e^{-\gamma}\left(Q_e^2+Q_m^2\right)^3}{\left[e^{\gamma}Q_e^2+e^{-\gamma}Q_m^2\right]^3}r^2, \qquad g_2 = -\frac{\left(Q_e^2+Q_m^2\right)^6}{\left[2\cosh(2\gamma)Q_e^2Q_m^2+Q_e^4+Q_m^4\right]^3}r^2. \tag{5.2.40}$$

Such that if we consider only electric charge $Q = Q_e$ ($Q_m = 0$), the determinants are

$$g_1 = -e^{-4\gamma}r^2, \qquad g_2 = -r^2, \tag{5.2.41}$$

and the deflection angles α_1^{GB} and α_2^{GB} are given by

$$\alpha_2^{GB} = \left(\frac{4M}{b} - \frac{3\pi e^{-\gamma}Q_e^2}{4b^2} - \frac{3\pi M^2}{4b^2} + \frac{8e^{-\gamma}MQ_e^2}{3b^3} - \frac{3\pi e^{-2\gamma}Q_e^4}{16b^4}\right) = e^{2\gamma}\alpha_1^{GB}, \tag{5.2.42}$$

the deflection angle α_2^{GB} only differs from the RN deflection in the screening of the charge. For the deflection angle α_2^{GB} in [70] were considered only the first two terms in Eq. (5.2.42). The effect introduced in the deflection angle by the third and fourth terms is illustrated in Fig. 5.7. Note that in [70] the deflection angle is overestimated.

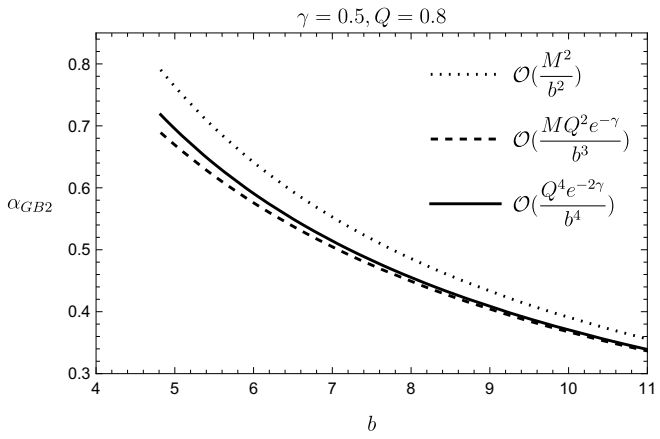

Figure 5.7: We compare the deflection angle α_2^{GB} of Eq. (5.2.42) to different orders of $\mathcal{O}(\frac{MQ^2}{b})$. The dotted line corresponds to the deflection angle considering the first two terms of Eq. (5.2.42), this is the deflection angle presented in [70]. The deflection angles taking the third and fourth terms in Eq. (5.2.42) are the dashed and solid lines, respectively. We are taking $M = 1$.

In Fig. 5.8 we compare the numerical result for the deflection angle (dashed) with the weak deflection angles of the ModMax BH calculated according to the Gauss-Bonnet theorem for different orders of $\mathcal{O}(\frac{MQ^2}{b})$ (solid curves). The dotted line is the deflection angle calculated

in [70] for the massless test particles. The deflection angles for the effective metric $g^{\text{eff}(1)}$ are the black curves while the ones for the metric $g^{\text{eff}(2)}$ are the gray curves. The lower value for the deflection angle is reached by considering all the terms in Eq. (5.2.42) for the metric $g^{\text{eff}(1)}$, and the higher value corresponds to the numerical result for the effective metric $g^{\text{eff}(2)}$.

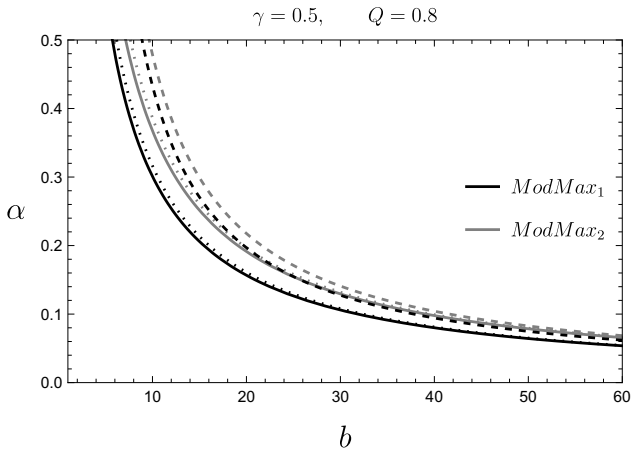

Figure 5.8: The plot compares the numerical result for α_1 and α_2 (dashed lines) with the Gauss-Bonnet calculation of the deflection angle in Eq. (5.2.42), α_1^{GB} and α_2^{GB} (solid lines), and the deflection angle presented in [70] (dotted lines). Note that as $b \to \infty$ the deflection angles approach the same limit. We are taking $M = 1$.

5.2.5 Redshift

The gravitational redshift z is a decrease in the frequency and photon energy of a light pulse, between the emission and the reception, when the pulse propagates through a gravitational field [109]–[111]; the redshift z is given by

$$1 + z = \frac{\omega_e}{\omega_o}, \tag{5.2.43}$$

where ω is the frequency and the subscripts e and o refer to the emitter and observer of the light pulse. In general, the frequency of a photon measured by an observer with proper 4-velocity U^μ is given by

$$\omega_i = -\left(k_\mu U^\mu\right)_i, \tag{5.2.44}$$

where "i" refers to "e" the emitter or "o" the observer, and $k_\mu = \{\omega, \vec{k}\}$ is the wave vector.

We shall determine the redshift z of a light pulse emitted from a particle moving in a circular orbit around the ModMax BH [112]. It is important to distinguish the trajectory of the emitter particle, which are timelike geodesics of the background metric $g_{\mu\nu}$; while the photon trajectories are the null geodesics of the effective or optical metric $g^{\text{eff}(a)}_{\mu\nu}$.

Considering equatorial circular orbits, for the emitter particle, the 4-velocity U^μ is of the form $U^\mu = (U^t, U^r = 0, U^\theta = 0, U^\phi)$, in this case, the redshift is given by

$$1 + z = \frac{\omega_e}{\omega_o} = \frac{\left(k_t U^t + k_\phi U^\phi\right)_e}{\left(k_t U^t + k_\phi U^\phi\right)_o}. \tag{5.2.45}$$

From an analysis analogous to the one in Sec. 5.2.2, now for the background geometry $g_{\mu\nu}$, we can determine the emitter particle velocity in an equatorial circular orbit; its energy, E_m, and angular momentum, L_m,, are conserved quantities, $U^t = -\frac{E_m}{g_{tt}}$ and $U^\phi = \frac{L_m}{g_{\phi\phi}}$, where the subscript m differentiate the emitter particle quantities from the photon ones. To determine E_m and L_m in terms of the BH parameters we use the circular orbit conditions (5.2.18), where the effective potential is given in Eq. (5.2.17) making $g^{\text{eff}}_{\mu\nu} \mapsto g_{\mu\nu}$, with $\delta = -1$,

$$V_{\text{eff,m}} = f(r)\left(\frac{1}{r^2} - \frac{1}{f(r)}\frac{E_m^2}{L_m^2} + 1\right), \tag{5.2.46}$$

obtaining for E_m and L_m,

$$E_m^2 = \frac{f^2(r)}{h(r)}, \qquad L_m^2 = \frac{\left(Mr - e^{-\gamma}Q^2\right)}{h(r)}, \tag{5.2.47}$$

where we defined $h(r) = 1 - 3M/r + 2e^{-\gamma}Q^2/r^2$. Writing the angular velocities of the emitter particle as $\Omega_i = U_i^\phi / U_i^t$,

$$\Omega_i^2 = \frac{Mr_i - e^{-\gamma}Q^2}{r_i^4}, \qquad i = e, o, \tag{5.2.48}$$

and the frequency ω_i of a photon given by

$$\omega_i = -U_i^t \left(k_t + k_\phi \Omega\right)_i. \tag{5.2.49}$$

The photons move along null geodesics of the effective metric $g^{\mu\nu}_{\text{eff}(a)} k_\mu k_\nu = 0$, where $k^t = E/f(r)$ and $k^\phi = L/r^2$; then in terms of the impact parameter, $b = L/E$, [113], the expression for the photon frequency is

$$\omega_i = -\sqrt{\frac{1}{h(r_i)}}\left(\frac{g^{\text{eff}(a)}_{tt}}{f(r)} + b\frac{g^{\text{eff}(a)}_{\phi\phi}}{r^4}\sqrt{Mr - e^{-\gamma}Q^2}\right)_i, \tag{5.2.50}$$

and considering the critical impact parameter in Eq. (5.2.20)

$$\omega_i = -\sqrt{\frac{1}{h(r_i)}}\left\{\frac{g_{tt}^{\text{eff}(a)}}{f(r)} \pm \sqrt{\frac{-g_{tt}^{\text{eff}(a)}}{f(r)}\frac{g_{\phi\phi}^{\text{eff}(a)}}{r^2}}\sqrt{\frac{Mr - e^{-\gamma}Q^2}{f(r)r^2}}\right\}_i , \tag{5.2.51}$$

where the $\pm$ sign refers to a receding or an approaching emitter particle, respectively. Such that the blueshift $(+)$ /redshift $(-)$ for the effective metrics $g_{\text{eff}(a)}, a = 1, 2$, are given by

$$(z_1)_\pm = \left(\frac{h(r_o)}{h(r_e)}\right)^{1/2}\left(\frac{-e^{-\gamma} \pm A(r_e)}{-e^{-\gamma} \pm A(r_o)}\right) - 1, \tag{5.2.52}$$

where we denote

$$A^2(r) = (Mr - e^{-\gamma}Q^2)/(f(r)r^2) \tag{5.2.53}$$

$$(z_2)_\pm = \left(\frac{h(r_o)}{h(r_e)}\right)^{1/2}\left(\frac{-e^{-\gamma} \pm e^{\gamma}A(r_e)}{-e^{-\gamma} \pm e^{\gamma}A(r_o)}\right) - 1. \tag{5.2.54}$$

Considering an observer at infinity, $r_o \to \infty$, then $A(r_o) = 0, \quad h(r_o) = 1$, and the redshifts are

$$(z_1)_\pm = -\sqrt{\frac{1}{h(r_e)}}\left[-1 \pm e^{\gamma}A(r_e)\right] - 1 \tag{5.2.55}$$

$$(z_2)_\pm = -\sqrt{\frac{1}{h(r_e)}}\left[-1 \pm e^{2\gamma}A(r_o)\right] - 1 \tag{5.2.56}$$

In Fig. 5.9 are plotted the redshifts as a function of the emitter position, r_e, as measured by an observer at r_o in the vicinity of the BH and an observer at infinity. Note the difference in the z-range. In terms of the frequency, for a given position of the emitter r_e, the frequency measured by an observer in the vicinity of the BH is larger than the frequency measured by the observer located at infinity.

In Fig. 5.10 is illustrated the effect on the redshift, Eq. (5.2.52), of varying the charge and NLED parameter of the ModMax BH, for the effective metric $(g_{\text{eff}(1)}^{\mu\nu})$, and for an observer located in the vicinity of the BH. For a fixed γ the increase of the BH charge diminishes the redshift (increases the frequency); and with a fixed BH charge Q, increasing γ increases the redshift (diminishes the frequency).

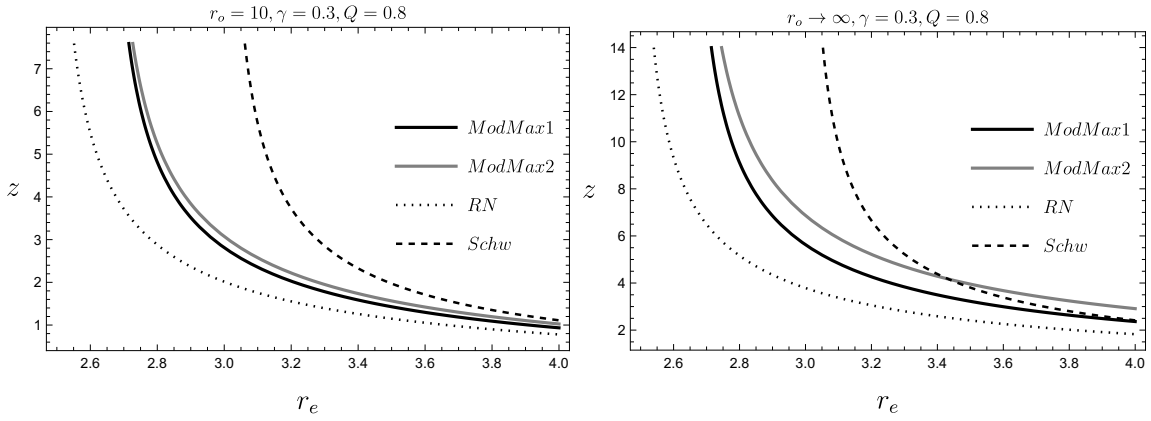

Figure 5.9: The redshifts of a pulse emitted from a particle moving in a circular orbit around the Schwarzschild, RN, and ModMax BHs as a function of the emitter position r_e measured by an observer in the vicinity of the BH ($r_o = 10$) are illustrated to the left. The case where the observer is located at infinity ($r_o \mapsto \infty$) is illustrated to the right. For a given value of r_e, the redshift for an observer in the vicinity of the BH is smaller than the one measured by the observer at infinity; in terms of the observed frequency ω_o, the one measured by the observer in the vicinity is higher than the frequency measured by the observer located at infinity. In this plot $\gamma = 0.3$, $Q = 0.8$, $M = 1$.

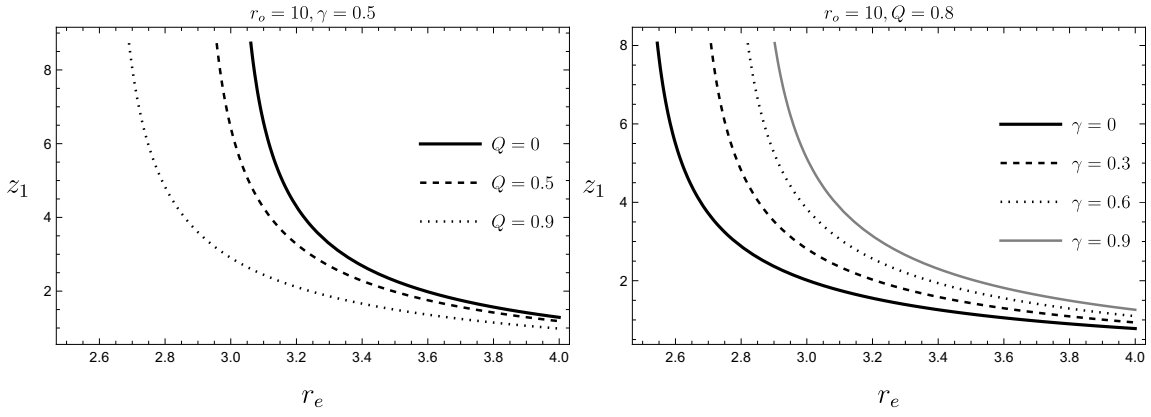

Figure 5.10: We plot the redshifts produced by ($g^{\mu\nu}_{\text{eff}(1)}$) as a function of the emitter position r_e, Eq. (5.2.52); to the left for different values of the BH charge with a fixed $\gamma = 0.5$; $Q = 0$ corresponds to Schwarzschild BH. And to the right for different values of the nonlinear parameter γ with fixed charge $Q = 0.8$; $\gamma = 0$ corresponds to RN BH. We are taking $M = 1$.

In the case that both the emitter and observer are static and the observer's position tends

to infinity, $r_o \to \infty$, then $U^\phi = 0$, and from $U^\mu U_\mu = -1$ we obtain

$$U^t = \sqrt{-\frac{1}{g_{tt}}}; \tag{5.2.57}$$

then the frequency ω_i of a light pulse is

$$\omega_i = -\left(k_t U^t\right)_i = \left(-\frac{g_{tt}^{\text{eff}(a)}}{f(r)}\sqrt{-\frac{1}{g_{tt}}}\right)_i; \tag{5.2.58}$$

while for the observer at infinity $r_o \to \infty$, $\omega_o = 1$, and the redshift is

$$1 + z = -\frac{g_{tt}^{\text{eff}(a)}}{f(r)}\sqrt{\frac{1}{f(r)}}. \tag{5.2.59}$$

The redshifts corresponding to the two effective metrics are given by

$$z_1 = \frac{e^{-\gamma}\left(e^{-\gamma}Q_e^2 + e^{\gamma}Q_m^2\right)}{Q_e^2 + Q_m^2}\sqrt{\frac{1}{f(r)}} - 1, \tag{5.2.60}$$

$$z_2 = \sqrt{\frac{1}{f(r)}} - 1; \tag{5.2.61}$$

z_2 corresponds to the redshift of a massless particle in a RN BH with a screened charge $Q^2 \mapsto e^{-\gamma}Q^2$.

In Fig. 5.11 are compared the redshifts for the ModMax, the RN, and the Schwarzschild BHs as a function of the emitter position, for a static observer ($r_o \mapsto \infty$); the frequency of the light pulse moving in the effective metric $g_{\mu\nu}^{\text{eff}(1)}$ is larger than the one of the light pulse moving in $g_{\mu\nu}^{\text{eff}(2)}$ or in the RN BH and Schwarzschild BH metric. The relative magnitudes of the redshift, $z_1 < z^{\text{RN}} < z_2 < z^{\text{Schw}}$, tell us that the ModMax BH creates a weaker gravitational field (for the photons) than RN BH since the photon in the vicinity of the ModMax BH suffers a smaller loss of energy to climb the gravitational potential than the RN one.

In Fig. 5.12, we compare the redshifts of a light pulse moving in the effective metrics $g_{\mu\nu}^{\text{eff}(a)}, a = 1, 2$, emitted from a particle orbiting the BH, for different positions of the observer. The larger frequency (smaller z) would be measured by the observer at infinity when the emitter is static and the pulse of light moves according to the effective metric $g_{\mu\nu}^{\text{eff}(1)}$.

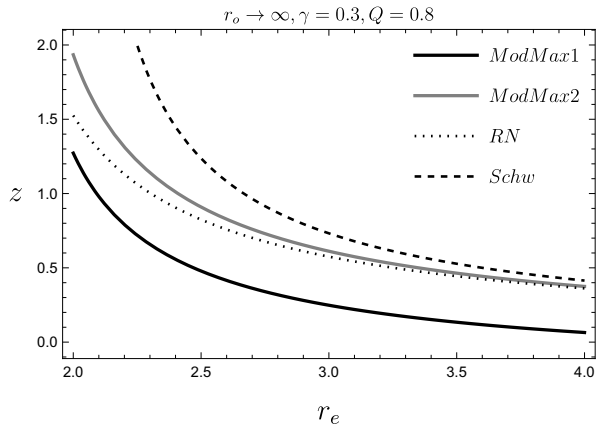

Figure 5.11: The redshifts of a light pulse emitted from a static particle at r_e in the vicinity of Schwarzschild, RN, and ModMax BHs, measured by an observer located at infinity ($r_o \mapsto \infty$). The frequency corresponding to the effective metric $g^{\text{eff}(1)}_{\mu\nu}$ is higher than the one for the effective metric $g^{\text{eff}(2)}_{\mu\nu}$, since $z_1 < z^{\text{RN}} < z_2 < z^{\text{Schw}}$. In this plot are fixed $\gamma = 0.3$, $Q = 0.8$, $M = 1$.

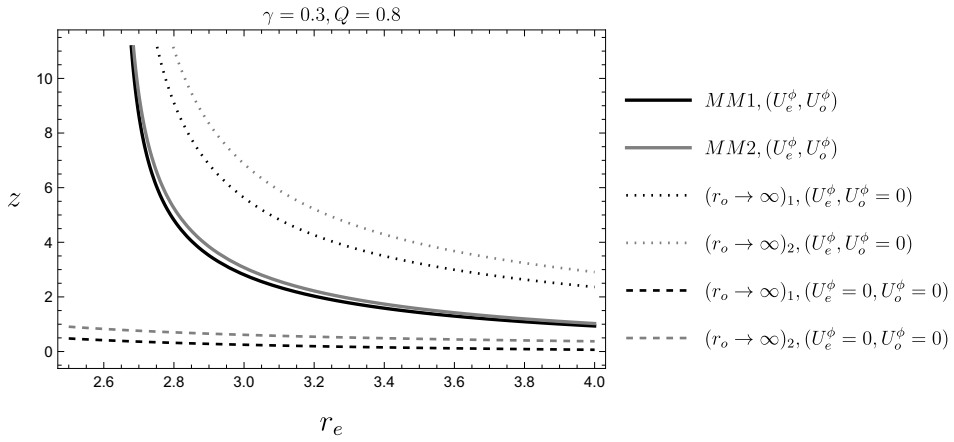

Figure 5.12: We plot the redshift of a light pulse in three situations: (1) the emitter is a particle moving in a circular orbit around the ModMax BH, and the observer is in the vicinity of the BH orbiting as well (solid curves), $U^\phi_e \neq 0$ and $U^\phi_o \neq 0$. (2) the emitter is orbiting around the ModMax BH and the observer is located at infinity (dotted), i.e. $U^\phi_e \neq 0$ and $U^\phi_o = 0$. (3) Both, emitter and observer, are static at infinity (dashed curves) $U^\phi_e = 0$ and $U^\phi_o = 0$. BH parameters are fixed: $\gamma = 0.3$, $Q = 0.8$, $M = 1$.

5.2.6 The kinematic redshift

The kinematic redshift is relevant in relation to astrophysical observations, for instance in measurements of galaxies redshift [112]. It is given by the difference between the redshift in Eq. (5.2.45) and the redshift of a photon emitted from $b = 0$, using Eq. (5.2.50)

$$z_k = \frac{\omega_e}{\omega_o} - \left(\frac{\omega_e}{\omega_o}\right)_{b=0} = b\frac{U_e^t}{U_o^t}\frac{\Omega_o - \Omega_e}{(1 - b\Omega_o)}. \tag{5.2.62}$$

Considering the two effective metrics, the kinematic redshifts z_{k_i} are given by

$$z_{k1} = e^{\gamma}\sqrt{\frac{h(r_o)}{h(r_e)}}\left(\frac{A(r_e) - A(r_o)}{\mp 1 + e^{\gamma}A(r_o)}\right), \tag{5.2.63}$$

$$z_{k2} = e^{\gamma}\sqrt{\frac{h(r_o)}{h(r_e)}}\left(\frac{A(r_e) - A(r_o)}{\mp e^{-\gamma} + e^{\gamma}A(r_o)}\right). \tag{5.2.64}$$

recalling Eq. (5.2.53). In the case that the observer is located at infinity with respect to the center of the BH, $r_{\rm o} \to \infty$, the kinematic redshifts are

$$z_{k1} = \mp e^{\gamma}\sqrt{\frac{A^2(r_e)}{h(r_e)}}, \tag{5.2.65}$$

and

$$z_{k2} = \mp e^{2\gamma}\sqrt{\frac{A^2(r_e)}{h(r_e)}}. \tag{5.2.66}$$

The kinematic redshift is illustrated in Fig. 5.13 for the Schwarzschild, RN, and ModMax BHs, as observed near the BH and at infinity; the relation between the redshifts of the two ModMax BH effective metrics is $z_{k2} = e^{\gamma}z_{k1}$. Note that there is a difference in the range between the kinematic redshift and the redshift in Fig. 5.9; the kinematic redshift reaches smaller values for a given position of the emitter.

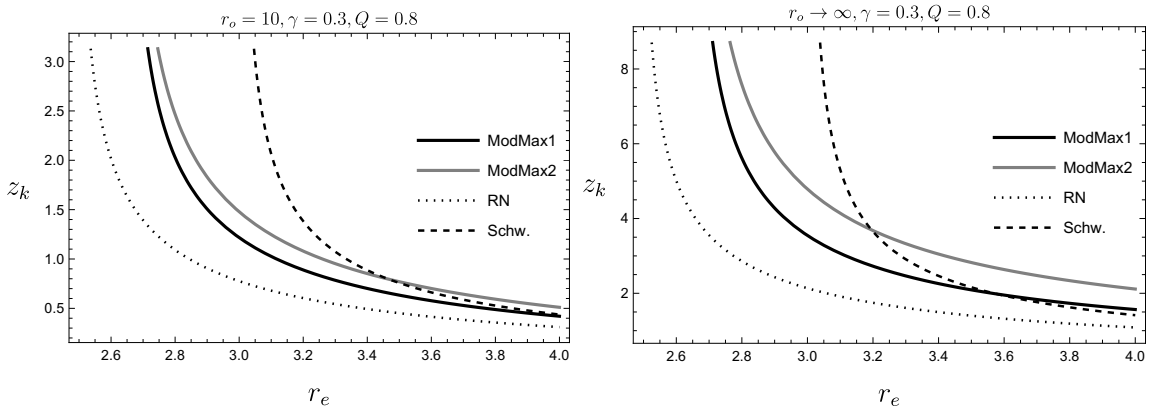

Figure 5.13: The kinematic redshifts z_k for Schwarzschild, RN, and ModMax BHs are illustrated as a function of the emitter position; to the left for an observer in the vicinity of the BH and to the right for an observer at infinity. For a given r_e the redshift measured by an observer at infinity is larger (smaller frequency) than the one for the observer in the vicinity of the BH. We are taking $M = 1$.

5.2.7 Shadow

Since 1998 [114] it has been suggested that supermassive black holes lie at the center of nearly every galaxy and indeed very recently the proof of the existence of such a black hole in the center of our galaxy has been reported.

The Event Horizon Telescope (EHT) is a large telescope array consisting of a global network of radio telescopes. The EHT project combines data from several very-long-baseline interferometry (VLBI) stations around Earth, which form a combined array with an angular resolution sufficient to observe objects the size of a supermassive black hole's event horizon. The project's observational targets include the two black holes with the largest angular diameter as observed from Earth: the black hole at the center of the elliptical galaxy Messier 87 (M87*), and Sagittarius A* (Sgr A*) at the center of the Milky Way [115].

Sgr. A* has been studied at several wavelengths: radio, millimeter, infrared, and X-ray. It has been discovered that the emission (at different wavelengths) originates near the BH's innermost stable circular orbit. The images of Sgr A* show a spiral polarization pattern that is stable, linearly polarized, and azimuthally symmetric [116].

The images obtained by the EHT collaboration verified that, for distant observers, the spherical accretion flows around a BH would appear as "rings of light" around a "shadow" [117]. In the vicinity of a BH, there is the possibility of unstable circular orbits of massless particles and photons; any perturbation will cause either the particle to fall into the BH or to escape to infinity. Photons that escape to infinity produce a shadow cast perceived by an external observer as a dark circular region.

The shadow of a BH is observable when the source of photons is sufficiently bright and is present close to the horizon to experience strong gravitational lensing, moreover, the source of photons, at the wavelength chosen for the observation, needs to be optically thin such that the shadow is not hidden by material generating radiation. These conditions are fulfilled by Sgr A*, then, the EHT collaboration determines the angular diameter of the BH shadow $d_{sh} = 48.7 \pm 7.0 \mu as$, and also a deviation parameter δ, which quantifies the fractional difference between the inferred shadow diameter and its expected value for a Schwarschild BH: $\delta = -0.08^{+0.09}_{-0.09}$. For comparison, a spinning BH has $-0.08 \leq \delta \leq 0$.

In [70] is presented the shadow produced by massless particles calculated considering the null geodesics of the background metric $g_{\mu\nu}$ of the ModMax BH, and it is analyzed the effect of the nonlinear parameter γ on the shadow measured by an observer co-moving with the cosmological expansion. As we have shown, there are two possible photon paths, corresponding to the null geodesics of the two effective or optical metrics. One of the trajectories corresponds to the null geodesics of the background metric, which we have denoted by $g^{\text{eff}(2)}_{\mu\nu} = g_{\mu\nu}$, and is the one studied in [70].

The second possible trajectory, the null geodesics of $g^{\text{eff}(1)}_{\mu\nu}$ generate a second shadow and a second absorption cross section (ACS), that we present in the following.

To calculate the radius of the shadow for a distant observer in a SSS spacetime, we can use the optical approximation where the critical impact parameter corresponds to the radius of the shadow $r_{sh} = b_c$, [118], [119], then from Eq. (5.2.21),

$$r_{sh1} = \sqrt{\frac{e^{-2\gamma} r_c^2}{f(r_c)}}, \qquad r_{sh2} = \sqrt{\frac{r_c^2}{f(r_c)}};$$

recall that r_c is the radius of the photosphere, i.e. the radius of the unstable circular orbits

(UCO) of the photon, that for a NLED BH has to be calculated from the effective metric. To compare the ModMax BH shadow with the observed angular radius of Sgr A^* we follow the methodology used in [119] considering the uncertainty allowed by the EHT observations, with δ as the fractional deviation between the shadow radius r_{sh} and the shadow radius of a Schwarzschild BH $\delta = r_{sh}/(3M\sqrt{3}) - 1$. Assuming Gaussianity, the values for δ following 1σ and 2σ confidence intervals are $-0.125 \gtrsim \delta \gtrsim 0.005$ for (1σ) and $-0.19 \gtrsim \delta \gtrsim 0.07$ for (2σ). In Fig. 5.14 is shown the shadow radius generated by the two effective metrics and the corresponding to the RN BH as a function of the BH charge Q, contrasted by the EHT for Sgr A^*. As the charge increases the radius of the shadow diminishes and the restrictions imposed by the 1σ allow us to set bounds in the BH charge or γ. For $g^{\text{eff}(1)}$ we are considering different values of γ, and note that as γ increases the shadow radius is no longer in the 1σ region. Consistency with the observations of the shadow of Sgr A^* for RN BH restricts the BH charge to $Q \leq 0.8M$; for the ModMax BH, this constraint becomes $Qe^{-\gamma/2} \leq 0.8M$, or $\gamma \geq -2\ln(0.8M/Q)$. For instance, if we set the value of $\gamma = 0.12$ as a lower bound of γ, the radius of the shadow is no longer in the 1σ region for values of the charge $Q \geq 0.2991$. For lower values of γ, a greater range of Q is allowed, i.e. the constraints for γ depend on the values of Q.

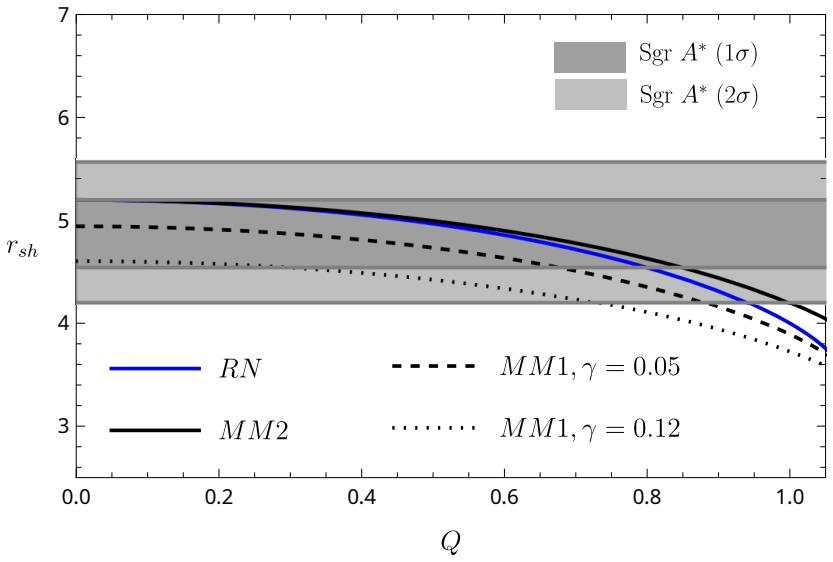

Figure 5.14: The shadow radius by the two effective metrics of the MM BH as a function of the BH charge. For $g^{\text{eff}(1)}$ (dashed and dotted) we fixed $\gamma = 0.05$ and $\gamma = 0.12$; while for $g^{\text{eff}(2)}$, $\gamma = 0.12$. The shadow radius for the RN BH (blue line) is the reference to define the effects due to the electromagnetic nonlinearity. The dark gray and light gray bands correspond to the 1σ and 2σ, respectively, for the Sgr A^* BH; the line at $r_{sh} = 3\sqrt{3} \approx 5.19$ corresponds to the Schwarzschild's shadow. We are taking $M = 1$.

5.2.8 The shadow for an observer at infinity

Alternatively, the shadow can be determined by considering a light ray from the observer to the UCO at an angle ψ_{sh} with respect to the radial direction. The expression for the deviation angle associated with the shadow is [45]

$$\sin^2(\psi_{sh})_a = -(b_{ca}^2)\left(\frac{g_{\phi\phi}^{\text{eff}(a)}}{g_{tt}^{\text{eff}(a)}}\frac{f^2(r_o)}{r_o^4}\right)_{r_o}. \tag{5.2.67}$$

In terms of the two impact parameters we obtain

$$\sin^2(\psi_{sh})_1 = e^{2\gamma}b_{c1}^2\frac{f(r_o)}{r_o^2}, \qquad \sin^2(\psi_{sh})_2 = b_{c2}^2\frac{f(r_o)}{r_o^2}. \tag{5.2.68}$$

The radius of the BH shadow is approximated in terms of the observer's position and the angle ψ_{sh} as [99], [120], [121]

$$r_{\text{sh}} = r_o \tan\psi_{sh} \approx r_o \sin\psi_{sh}. \tag{5.2.69}$$

Then using Eq. (5.2.21) we can calculate the radius of the shadow, assuming that the observer is located at infinity $r_o \mapsto \infty$. Despite the existence of two values for the impact parameter, corresponding to the two effective metrics, in this approximation, the static observer at infinity will detect only one shadow of the ModMax BH; the reason is that there is a cancellation of the screening factor, using the relation $e^{2\gamma} b_{c1}^2 = b_{c2}^2$ in Eqs. (5.2.68) and the approximation in Eq. (5.2.69) implies that $\sin^2(\psi_{sh})_1 = \sin^2(\psi_{sh})_2$.

In Fig. 5.15 are illustrated the radii of the BH shadows for Schwarzschild, RN, and the ModMax BHs, considering that the position of the observer is at infinity, $r_o \to \infty$. Notice that the shadow radius of the ModMax BH is larger than the RN one and smaller than Schwarzschild's, $r_{\rm sh}^{RN} < r_{\rm sh}^{MM} < r_{\rm sh}^{Schw}$, i.e. the radius of the shadow for the effective metric $g^{\rm eff(2)}$ is located between the radius of the shadow for RN BH and the one for the Schwarszchild BH in agreement with the results in [70].

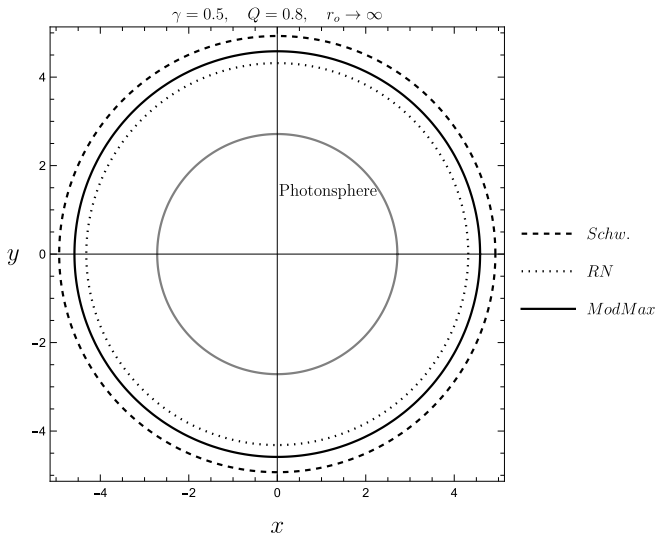

Figure 5.15: The radii of the BH shadows for Schwarzschild, RN, and the ModMax BHs are illustrated considering that the position of the observer is at infinity, $r_o \to \infty$; the relative sizes of the shadow radii are $r_{\rm sh}^{RN} < r_{\rm sh}^{MM} < r_{\rm sh}^{Schw}$. The gray circumference is the photosphere r_c of the ModMax BH. In this plot $Q = 0.8$ and $\gamma = 0.5$, $M = 1$ and polar coordinates are $x = r_{sh}\cos(\zeta)$, $y = r_{sh}\sin(\zeta)$.

In Fig. 5.16 is shown the shadow radius for the ModMax BH, for different values of γ, as well as the RN's, as a function of the charge Q, contrasted to the constraints by the EHT

for Sgr A^*. As the charge increases the radius of the shadow decreases. In the RN BH case constraints on the value of the charge can be deduced. In the case of the ModMax BH there is the additional parameter γ and the radius of the shadow depends on both (γ, Q). The screening of $e^{-\gamma}$ allows larger values for the charge; such that for the range $0 < \gamma < 3.6$ the ModMax BH shadow remains in the (1σ) interval.

For $\gamma = 3.6$ the shadow radius is $r_{sh} = 5.19521$ with a BH charge of $Q = 0.2$; while $r_{sh} = 5.18096$ with a BH charge $Q = 0.8$; both tend to the shadow radius for the Schwarszchild BH, $r_{sh,SHW} = 5.19615$ within the uncertainty established by the (1σ) interval.

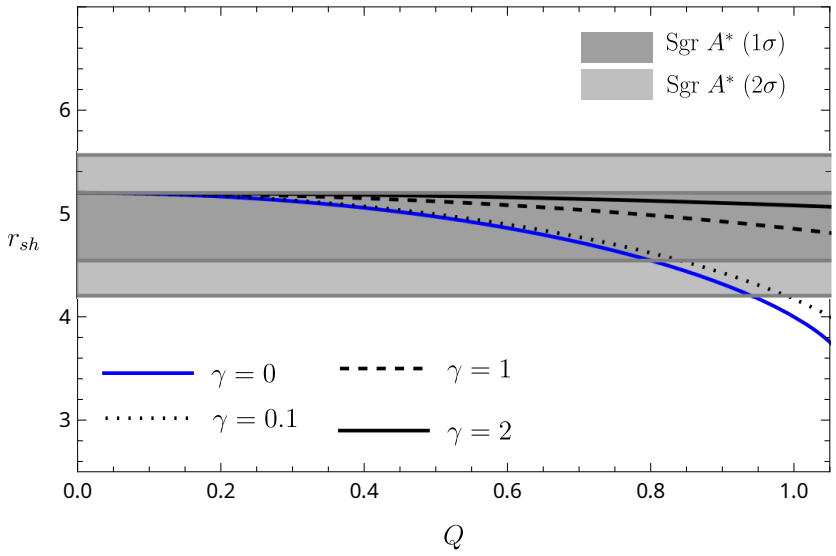

Figure 5.16: The shadow radius of the ModMax BH (black lines) as a function of the BH charge, for different values of γ, is compared to the shadow radius of the RN BH (black line). The dark gray and light gray bands correspond to the 1σ and 2σ, respectively, for the Sgr A^* BH. We are taking $M = 1$

5.2.9 Absorption cross section

On the plane of a distant observer, the boundary of the BH shadow marks the apparent image of the photon region that separates capture orbits from scattering orbits. The absorption cross-section (ACS) originates in the photons moving in UCO that are captured by the BH; in the limit of geometrical optics [122] the ACS is given by $\sigma_a = \pi b_c^2$, with b_c being the impact

parameter of the UCO. For the ModMax BH, due to the existence of two impact parameters corresponding to the two effective metrics Eqs. (5.1.4) and (5.1.5), there are two ACS,

$$\sigma_a = \pi b_{ca}^2, \quad a = 1, 2. \tag{5.2.70}$$

that are shown in Fig. 5.17. The relation between the two ModMax BH ACS is $\sigma_2 = e^{2\gamma}\sigma_1$ and the relative magnitude compared with Schwarzschild and RN ACS is $\sigma^{Schw} > \sigma_2 > \sigma^{RN} > \sigma_1$, in agreement with the shadow sizes.

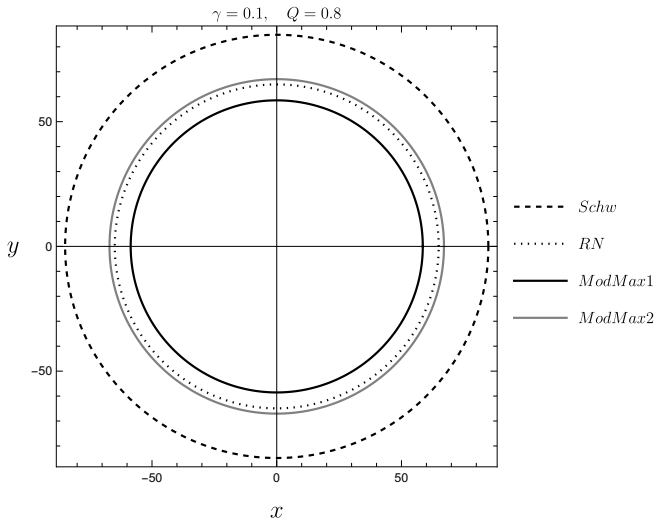

Figure 5.17: We plot the absorption cross sections (ACS) of the Shwarzschild, RN, and the two effective metrics of the ModMax BH. The ACS for the effective metric $g^{\text{eff}(1)}$ is the black circle (the smallest), and for the effective metric $g^{\text{eff}(2)}$ is the gray one. The ACS for the effective metric $g^{\text{eff}(2)}$ is larger than the RN one. The larger ACS corresponds to the Schwarszchild BH. This plot is in polar coordinates, with $x = r_{sh}\cos(\zeta)$, $y = r_{sh}\sin(\zeta)$. The chargeless BH is favored by observations. We are taking $M = 1$.

5.3 Conclusions

Coupling the ModMax nonlinear electrodynamics with the Einstein equations, static spherically symmetric solutions with horizons have been found in [93], characterized by the parameters of mass, electric and/or magnetic charges, and the ModMax parameter γ. It turns out that the ModMax BH metric has the form of the RN metric with a charge screened by the factor $e^{-\gamma/2}$. To study light propagation in the vicinity of the ModMax BH as the background metric, we determine the two effective metrics. One of the consequences of the NLED conformal invariance is that one of the effective metrics turns out to be the background metric, $g_{\mu\nu}^{\text{eff}(2)} = g_{\mu\nu}$, therefore the studied effects (phase velocities, light trajectories, light ray deflection, redshift of light coming from the BH, shadow) are qualitatively the same as the ones for massless particles for a RN BH, but with a smaller charge, due to the screening produced by the nonlinear parameter γ, in the form of $Q^2 \mapsto e^{-\gamma}Q^2$. While the effects due to the second effective metric $g_{\mu\nu}^{\text{eff}(1)}$ are more interesting and cannot be deduced from the background metric.

We emphasize that while the massless particle effects of the ModMax BH background metric (equivalently to $g_{\mu\nu}^{\text{eff}(2)}$) can be described as a transition from the RN to the Schwarzschild BH, and approaching Schwarzschild as γ increases, the results provided by the second effective metric ($g_{\mu\nu}^{\text{eff}(1)}$ in our work) for the photon behavior cannot be deduced from the geometric or background metric of the electromagnetic nonlinear charged BH.

The results presented in this chapter are published in [123]

E. Guzman-Herrera, N. Breton,

"Light propagation in the vicinity of the ModMax black hole"

Journal of Cosmology and Astroparticle Physics, JCAP **01**, 041 (2024) ,

DOI 10.1088/1475-7516/2024/01/041

Chapter 6

Comparative of the three nonlinear electrodynamics

Along this thesis, we have determined the phase velocities of light moving in three different NLEDs; although the parameter of each NLE is different we would like to know which NLED is the most effective in slowing down light velocity in a magnetic or electric background, for instance. Or regarding NLED coupled to gravity, we can compare the shadows of the respective black hole solutions, test their shadows, and determine the ranges of their respective parameters (μ for EH, b for BI, and γ for ModMax), for which these shadows are in agreement with the observational evidence of Sagittarius A^*.

Therefore in this chapter, we focus on the comparison between different NLEDs. First, we compare the phase velocities of propagating light in a magnetic or electric background in a Minkowski spacetime, for three different observers, one of them static, another in uniform motion, and a third one in accelerated motion.

Then, the shadows produced by the static spherically symmetric black hole solutions of the different NLEDs coupled to gravity are compared with the observed Sagittarius A^* shadow.

6.1 Phase velocities

In this section we examine the phase velocities corresponding to the three NLEDs, considering the Minkowski spacetime as the background metric with a purely magnetic field $\vec{B} = B_x\hat{x} + B_z\hat{z}$ as the background. We calculate the phase velocities for the case of a static observer, i.e. no coordinate transformation is applied to the effective metrics. Then, the phase velocities when applying a Lorentz boost and finally as measured in an accelerated frame.

6.1.1 Static observer

We recall the phase velocities corresponding to the three NLEDs addressed. To make the comparison we consider a magnetic background field B in Minkowski spacetime and light propagating along the z direction.

For the EH NLED, recalling Eqs. (3.2.12) and (3.2.14)

$$v^2_{\rm EH1} = 1 - \frac{14\mu B_x^2}{10B^2\mu + 1}, \quad v^2_{\rm EH2} = 1 - \frac{8\mu B_x^2}{1 - 4B^2\mu} \tag{6.1.1}$$

where μ is related to the fine structure constant $\alpha = 1/137$.

For the BI NLED, there is no birefringence, and the phase velocity is Eq. (4.3.2)

$$v^2_{\rm BI} = 1 - \frac{B_x^2}{b^2 + B^2} \tag{6.1.2}$$

with b being the maximum attainable electric or magnetic field.

For the ModMax NLED, there is birefringence and one of the light trajectories is the one in vaccum, with phase velocity $v^2 = c^2 = 1$. While the other one is

$$v^2_{\rm MM} = 1 - \frac{2{\rm Bx}^2\tanh(\gamma)}{B^2[\tanh(\gamma) + 1]} \tag{6.1.3}$$

We plot the phase velocities as a function of the corresponding adimensional parameters: μB^2 for EH; B^2/b^2 for BI; and the ModMax NLE the phase velocity depends on B_x/B, such that the diminishing in ModMax case is constant. In Fig. 6.1 we observe the differences in the diminishing of the phase velocity for the three NLED theories.

The phase velocities when considering an electric background field in a Minkowski spacetime are analogously analyzed.

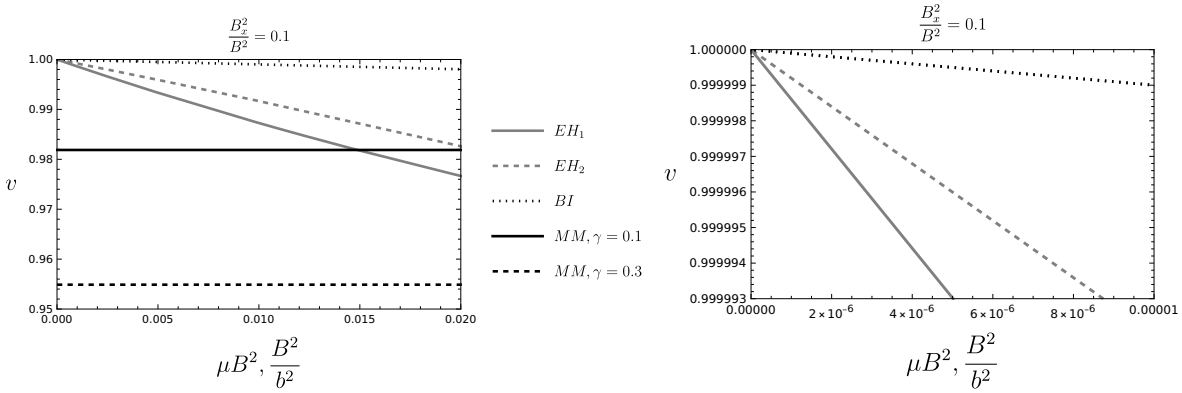

Figure 6.1: The phase velocities in the $z-$direction for three NLEDs are plotted. The gray lines corresponds to the phase velocity of a wave in the presence of an EH magnetic field. The black dotted line corresponds to the phase velocity of a wave in the presence of a BI background field. The black solid and dashed lines $v_{MM} = 0.990895$ corresponds to the value for the light velocity in vacuum in ModMax NLED. To the right, it is zooming the differences between EH and BI, which are qualitatively similar. We are considering the values of $Bx^2/B^2 = 0.1$.

The two possible phase velocities for the EH NLED are given by

$$v^2_{\mathrm{EH1,E}} = 1 - \frac{14E_x^2\mu}{4E^2\mu + 1}, \quad v^2_{\mathrm{EH2,E}} = 1 - \frac{8E_x^2\mu}{12E^2\mu + 1} \tag{6.1.4}$$

For the BI NLED, since there is no birefringence,

$$v^2_{\mathrm{BI,E}} = 1 - \frac{E_x^2}{b^2} \tag{6.1.5}$$

While phase velocity in a ModMax NLED,

$$v^2_{\mathrm{MM,E}} = 1 - \frac{2E_x^2\tanh(\gamma)}{E^2(\tanh(\gamma) + 1)} \tag{6.1.6}$$

The behavior at the order $\mu E^2, \frac{E^2}{b^2} \sim 10^{-2}$ is the same as the one for the magnetic background field. Moreover, the phase velocities for the wave in the presence of ModMax magnetic and electric fields in Eqs. (6.1.3) and (6.1.6) have the same dependence on the magnitude of the fields, a consequence of the dual invariance required by ModMax theory.

6.1.2 Observer in uniform motion

To determine phase velocities measured by an observer in uniform motion we perform a Lorentz boost. Previously this situation was only considered for the EH NLED. The phase velocities for the BI and ModMax NLEDs are calculated to complete the comparison.

For EH NLED recall Eqs. (3.4.7) and (3.4.8) for the phase velocities,

$$v_{L,EH1} = \frac{\left(\beta_L^2 - 1\right)\sqrt{\left(10B^2\mu + 1\right)\left(10B^2\mu - 14B_x^2\mu + 1\right)} - 14\beta_L B_x^2\mu}{\beta_L^2\left(-10B^2\mu + 14B_x^2\mu - 1\right) + 10B^2\mu + 1} \tag{6.1.7}$$

$$v_{L,EH2} = \frac{\left(\beta_L^2 - 1\right)\sqrt{\left(4B^2\mu - 1\right)\left(4B^2\mu + 8B_x^2\mu - 1\right)} - 8\beta_L B_x^2\mu}{\beta_L^2\left(4B^2\mu + 8B_x^2\mu - 1\right) - 4B^2\mu + 1} \tag{6.1.8}$$

For the BI theory, where there is no birefringence,

$$v_{L,BI} = \frac{\left(\beta_L^2 - 1\right)\sqrt{\left(b^2 + B^2\right)\left(b^2 + B^2 - B_x^2\right)} + \beta_L B_x^2}{\left(1 - \beta_L^2\right)\left(-b^2 - B^2\right) - \beta_L^2 B_x^2} \tag{6.1.9}$$

There is birefringence for the ModMax theory, but, the phase velocity due to one of the effective metrics is light velocity in vacuum c, and is invariant under Lorentz transformations. The second effective metric gives the phase velocity

$$v_{L,MM} = \frac{\left(\beta_L^2 - 1\right)\sqrt{B^2(\tanh(\gamma) + 1)\left(\left(B^2 - 2B_x^2\right)\tanh(\gamma) + B^2\right)} + 2\beta_L B_x^2\tanh(\gamma)}{B^2\left(\beta_L^2 - 1\right) + \tanh(\gamma)\left(B^2\left(\beta_L^2 - 1\right) - 2\beta_L^2 B_x^2\right)} \tag{6.1.10}$$

In Fig. 6.2 we plot the phase velocities Lorentz-transformed considering orders of $\mathcal{O}(\mu B^2)$ for EH, $\mathcal{O}(B^2/b^2)$ for BI and first order in γ for ModMax

$$v_{L,EH1} = 1 - 14B_x^2\mu\left(1 - \frac{1 - 3\beta_L}{2(1 - \beta_L)}\right) + \mathcal{O}(\mu^2) \tag{6.1.11}$$

$$v_{L,EH2} = 1 - 8B_x^2\mu\left(1 - \frac{1 - 3\beta_L}{2(1 - \beta_L)}\right) + \mathcal{O}(\mu^2) \tag{6.1.12}$$

$$v_{L,BI} = 1 - \frac{B_x^2}{b^2}\left(1 - \frac{\beta_L + 3}{2(\beta_L + 1)}\right) + \mathcal{O}(1/b^4) \tag{6.1.13}$$

$$v_{L,MM} = 1 - \frac{\gamma B_x^2}{B^2}\left(1 - \frac{2\beta_L}{1 - \beta_L}\right) + \mathcal{O}(\gamma^2) \tag{6.1.14}$$

While the behavior of the curves is qualitatively similar to the situation in the absence of motion of the frame the diminishing in the value of the phase velocities increases. In Chapter 3, the analogy between an effective optical metric and the effect of a material medium was

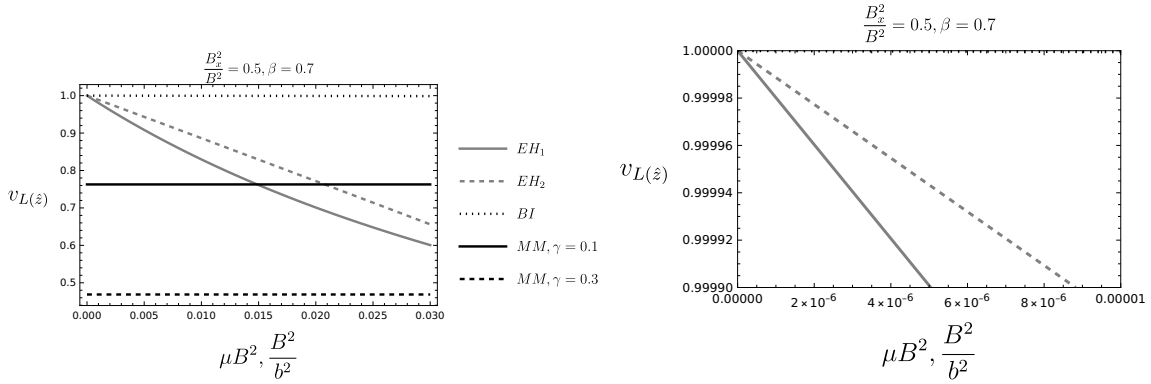

Figure 6.2: The phase velocities in the z-direction under a Lorentz transformation along z are plotted for the EH, BI, and ModMax NLEDs as follows: Gray lines with an EH background; black dotted lines for a BI background field and the black solid and dashed lines are the phase velocity of light through an intense ModMax background. We are considering the values of $B_x^2/B^2 = 0.5$, and $\beta_L = 0.7$.

introduced; in this context, we can interpret the Lorentz transformation as the movement of the medium. The velocity of the medium, Eq. (3.4.6), is now a function of the Lorentz parameter $\beta_L = v/c$ and the velocity of the propagating wave v_L. The analog medium velocities for the three NLEDs are listed and plotted in Fig. 6.3. For the NLED background, if the medium moves opposite to the propagating wave, it reaches very low values in the ranges $\mu B^2, B^2/b^2 \sim 10^{-2}$, respectively for EH and BI NLEDs, the medium velocity is close to zero. For the ModMax background, when the medium moves opposite to the propagating wave the diminishing in the velocity is more evident, as is appreciated in Figure 6.3.

$$V_{EH1} = \frac{14\beta_L B_x^2 \mu}{\left(1-\beta_L^2\right)\sqrt{\left(1-4B^2\mu\right)\left(-4B^2\mu+14B_x^2\mu+1\right)}} v_{L,EH1} \tag{6.1.15}$$

$$V_{EH2} = \frac{8\beta_L B_x^2 \gamma_L^2 \mu}{\sqrt{\left(1-12B^2\mu\right)\left(-12B^2\mu+8B_x^2\mu+1\right)}} v_{L,EH2} \tag{6.1.16}$$

$$V_{BI} = -\frac{\beta_L B_x^2 \gamma_L}{\sqrt{b^2\left(b^2+B_x^2\right)}} v_{L,BI} \tag{6.1.17}$$

$$V_{MM} = -\frac{2\beta_L B_x^2 e^{\gamma}\sinh(\gamma)}{B^2\left(1-\beta_L^2\right)\sqrt{\frac{B_x^2(e^{2\gamma}-1)}{B^2}+1}} v_{L,MM} \tag{6.1.18}$$

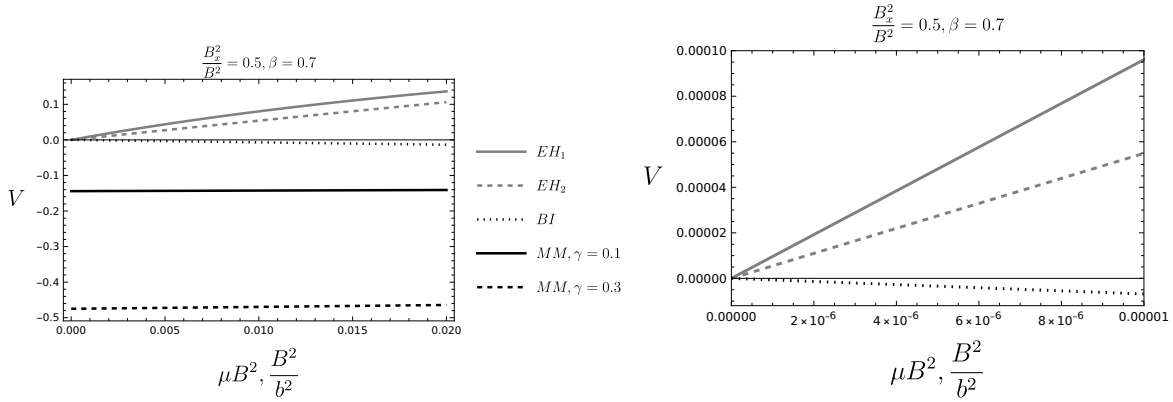

Figure 6.3: The medium velocities are plotted for the EH, BI, and ModMax NLEDs. Gray lines correspond to an EH background, the black dotted line to a BI background, and the black solid and dashed lines to the ModMax background. In the case of ModMax and BI, we note that the medium velocity moves in the opposite direction to the propagating wave (z). We are taking values of: $B_x^2/B^2 = 0.5$, $\gamma = 0.1$ and $\gamma = 0.3$ and $\beta_L = 0.7$

6.1.3 The accelerated frame

In Chapter 4 we determined the phase velocity of light rays propagating in a purely magnetic BI background as seen by an accelerated observer. Then, in this section, we calculate the case where the light rays propagate in purely magnetic EH and ModMax backgrounds. The phase velocities measured by an accelerated observer are listed below

$$\frac{v_{a,EH1}}{1+aZ} == \frac{-7B_x^2\mu\sinh(2aT) + \sqrt{(10B^2\mu+1)\,(10B^2\mu-14B_x^2\mu+1)}}{14B_x^2\mu\sinh^2(aT) + 10B^2\mu + 1} \tag{6.1.19}$$

$$\frac{v_{a,EH2}}{1+aZ} = \frac{4B_x^2\mu\sinh(2aT) - \sqrt{(4B^2\mu-1)\,(4B^2\mu+8B_x^2\mu-1)}}{-8B_x^2\mu\sinh^2(aT) + 4B^2\mu - 1} \tag{6.1.20}$$

$$\frac{v_{a,BI}}{1+aZ} = \frac{-B_x^2\sinh(2aT) + 2\sqrt{(b^2+B^2)\,(b^2+B^2-B_x^2)}}{2B_x^2\sinh^2(aT) + 2b^2 + 2B^2} \tag{6.1.21}$$

$$\frac{v_{a,MM}}{1+aZ} = \frac{-B_x^2\sinh(\gamma)\sinh(2aT) + \sqrt{B^4e^{2\gamma} - B^2B_x^2\,(e^{2\gamma}-1)}}{2B_x^2\sinh(\gamma)\sinh^2(aT) + B^2e^{\gamma}} \tag{6.1.22}$$

In Fig. 6.4 we plot the phase velocities for the accelerated observer considering orders of $\mathcal{O}(\mu B^2)$ for EH, $\mathcal{O}(B^2/b^2)$ for BI and $\mathcal{O}(\mu$ for ModMax

$$\frac{v_{a,EH1}}{1+aZ} = 1 - 7B_x^2\mu\,(1 + 2\sinh(aT)(\sinh(aT) + \cosh(aT))) + \mathcal{O}(\mu^2) \tag{6.1.23}$$

$$\frac{v_{a,EH2}}{1+aZ} = 1 - 4B_x^2\mu\,(1 + 2\sinh(aT)(\sinh(aT) + \cosh(aT))) + \mathcal{O}(\mu^2) \tag{6.1.24}$$

$$\frac{v_{a,BI}}{1+aZ} = 1 - \frac{B_x^2}{2b^2}\,(1 + 2\sinh(aT)(\sinh(aT) + \cosh(aT))) + \mathcal{O}(1/b^4) \tag{6.1.25}$$

$$\frac{v_{a,MM}}{1+aZ} = 1 - \frac{B_x^2\gamma}{B^2}\,(1 + 2\sinh(aT)(\sinh(aT) + \cosh(aT))) + \mathcal{O}(\gamma^2) \tag{6.1.26}$$

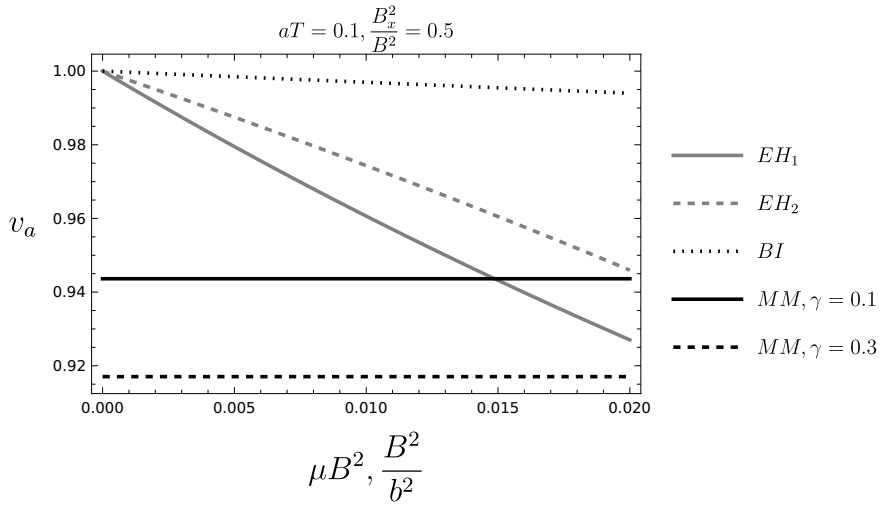

Figure 6.4: The phase velocities as measured by an accelerated observer are plotted for the EH, BI, and ModMax NLEDs. Gray lines correspond to an EH background. As the field increases, we note that the most effective NLED in diminishing the velocity is EH. The propagating wave in the BI background is the one that barely diminishes.

6.2 Black Holes

In Chapter 5 we considered the black hole solution of the ModMax NLED coupled to Einstein gravity. For the BI and ModMax NLEDs, there are as well static and spherically symmetric solutions that also admit a black hole interpretation. Therefore we address the BHs corresponding to the three NLEDs and compare the metric functions and the resulting radii of their shadows as seen by an observer at infinity and compare them with the observed Sagittarius A^* shadow.

6.2.1 Metric functions

In this section, we consider the corresponding BH metrics as the background metrics. It is interesting to compare the metric functions for the BHs of the three NLEDs in consideration with one of the Reissner-Nordstrom, the static spherically symmetric solution of the coupled Einstein-Maxwell equations. For the static spherically symmetric line element

$$ds^2 = -f(r)dt^2 + \frac{dr^2}{f(r)} + r^2 d\Omega, \tag{6.2.1}$$

The corresponding metric functions $f(r)$ for Schwarzschild, Reissner-Nordstrom (RN), Euler-Heisenberg (EH), Born-Infeld (BI), and ModMax (MM), are, respectively,

$$f_{Schw.}(r) = 1 - \frac{2M}{r} \tag{6.2.2}$$

$$f_{RN}(r) = 1 - \frac{2M}{r} + \frac{Q^2}{r^2} \tag{6.2.3}$$

$$f_{EH}(r) = 1 - \frac{2M}{r} + \frac{Q^2}{r^2} - \frac{\mu Q^4}{20 r^6} \tag{6.2.4}$$

$$f_{BI}(r) = 1 - \frac{2M}{r} + \frac{2}{3}b^2 r^2 \left(1 - \sqrt{\frac{Q^2}{b^2 r^4} + 1}\right) + \frac{2Q^2}{3r}\sqrt{\frac{b}{Q}} F\left[\text{ArcCos}\left(\frac{\frac{br^2}{Q} - 1}{\frac{br^2}{Q} + 1}\right), \frac{1}{\sqrt{2}}\right] \tag{6.2.5}$$

$$f_{MM}(r) = 1 - \frac{2M}{r} + \frac{e^{-\gamma} Q^2}{r^2} \tag{6.2.6}$$

In Fig. 6.5 we plot the metric functions for the Schwarschild, RN, EH, BI and ModMax black holes, when we consider a BH charge of $Qe = 0.9$, for $b > 0.7$, $f(r)$ is similar to the one for RN, while if $b < 0.7$, the metric function $f(r)$ is similar to Schwarzschild as established in [124].

6.2.2 The shadow of the black holes

In Chapter 5 we calculated the radius of the shadow of the ModMax BH, now we complete the study with the shadows of the EH and BI black holes and compare it to the RN BH; we consider an observer at infinity. Following Eq. (5.2.68) we obtain the deviation angle associated with the shadow. The critical impact parameters are calculated using Eq. (5.2.20)

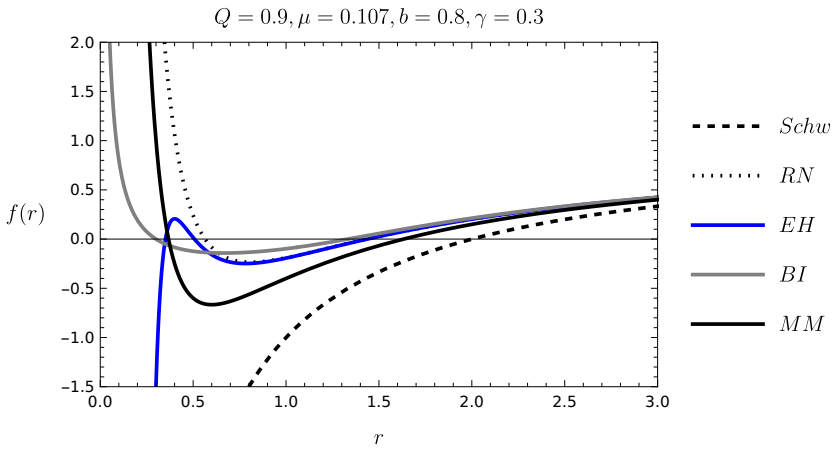

Figure 6.5: The metric functions $f(r)$ for the black holes considered are shown. The radii of the event horizons are the intersections of the corresponding metric functions with the $r-$axis.

and are listed below

$$b^2_{c,EH1} = \frac{r_c^2}{f_{EH}(r_c)} \frac{1 - 10\mu \frac{Q^2}{r_c^4}}{1 + 4\mu \frac{Q^2}{r_c^4}} \quad b_{c,EH2} = \frac{r_c^2}{f_{EH}(r_c)} \frac{1 + 4\mu \frac{Q^2}{r_c^4}}{1 + 12\mu \frac{Q^2}{r_c^4}} \tag{6.2.7}$$

$$b_{c,BI} = \frac{r_c^2 - \frac{Q^2}{b^2 r_c^2}}{f_{BI}(r_c)} \tag{6.2.8}$$

$$b_{c,MM1} = \frac{e^{-2\gamma} r_c^2}{f_{MM}(r_c)} \quad b_{c,MM2} = \frac{r_c^2}{f_{MM}(r_c)} \tag{6.2.9}$$

The NLED theories that present birefringence have two values for the critical impact parameter, corresponding to the two effective metrics. Using Eq. (5.2.69) we obtain the radius of the BH shadow

$$r^2_{sh,EH1} = r_c^2 \frac{f_{EH}(r_o)}{f_{EH}(r_c)} \frac{r_c^4 - 10Q^2\mu}{r_c^4 + 4Q^2\mu} \frac{r_o^4 + 4Q^2\mu}{r_o^4 - 10Q^2\mu} \tag{6.2.10}$$

$$r^2_{sh,EH2} = r_c^2 \frac{f_{EH}(r_o)}{f_{EH}(r_c)} \frac{r_c^4 + 4Q^2\mu}{r_c^4 + 12Q^2\mu} \frac{r_o^4 + 12Q^2\mu}{r_o^4 + 4Q^2\mu} \tag{6.2.11}$$

$$r^2_{sh,BI} = \frac{f_{BI}(r_o)}{f_{BI}(r_c)} \frac{r_o^4}{r_c^2} \frac{Q^2 - b^2 r_c^4}{Q^2 - b^2 r_o^2} \tag{6.2.12}$$

$$r^2_{sh,MM} = rc^2 \frac{f_{MM}(r_o)}{f_{MM}(r_c)} \tag{6.2.13}$$

As was established in Chapter 5, although there are two critical impact parameters for the ModMax BH, an observer located at infinity observes only one shadow, meanwhile, for the EH BH, there are two shadows.

In Fig. 6.6, assuming that the observer is located at infinity $r_o \to \infty$, we plot the radii of the BH shadows for Schwarzschild, RN, BI, EH, and ModMax BHs, considering the position of the observer at infinity. The radius of the shadow of the Schwarzschild BH is the larger one, for a value of the EH nonlinear parameter $\mu = 0.1$, $r_{SH} > r_{MM} > r_{RN} > r_{EH2} > r_{EH1} > r_{BI}$ and $\mu = 0.5$ $r_{SH} > r_{MM} > r_{RN} > r_{BI} > r_{EH2} > r_{EH1}$. As μ increases, the radius of the shadow becomes smaller.

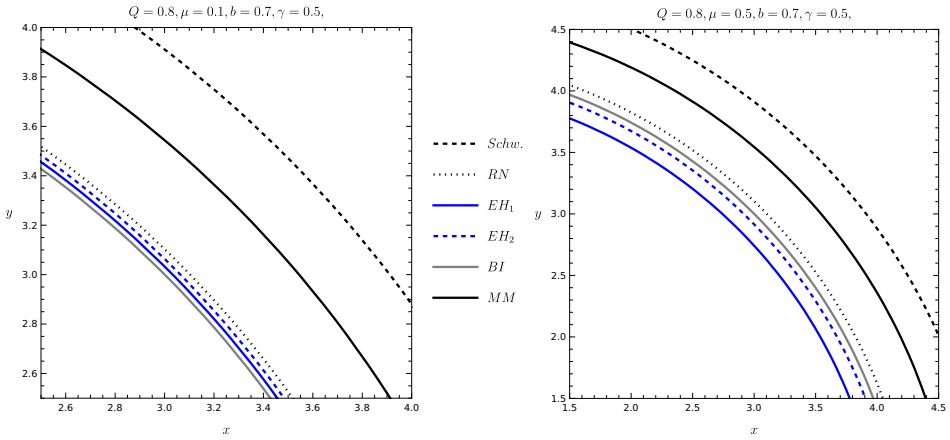

Figure 6.6: The radii of the BH shadows for Schwarzschild, RN, EH, BI, and ModMax BHs are illustrated considering an observer at infinity, $ro \to \infty$; the relative sizes of the shadow radii are $r_{SH} > r_{MM} > r_{RN} > r_{BI} > r_{EH2} > r_{EH1}$. In this plot $Q = 0.8$ and the nonlinear parameters $\mu = 0.5, b = 0.7, \gamma = 0.5$ and polar coordinates are $x = r_{sh}\cos(\zeta)$, $y = r_{sh}\sin(\zeta)$. We are taking $M = 1$.

As in Fig. 5.16 we show in Fig. 6.7 the shadow radius for the BHs in consideration as a function of the charge Q, contrasted to the constraints by the EHT for Sgr A^*. As the charge increases the radius of the shadow decreases.

We note that the radius of the shadow for BI and the second solution of EH behave similarly for values of the nonlinear parameters $b = 0.7, \mu = 0.5$. For the values of the nonlinear parameters $b = 0.7, \mu = 0.5, \gamma = 0.5$, the ModMax BH is the one that allows a

bigger value of the charge Q while the radius of the shadow is in the 1σ region of the plot.

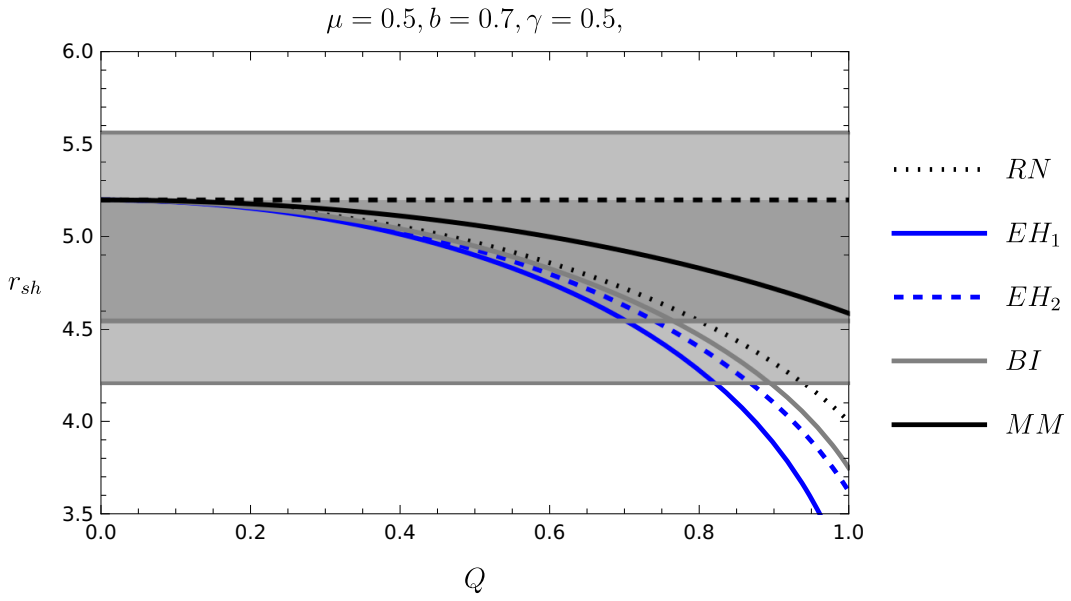

Figure 6.7: The shadow radii of the BHs in consideration as a function of the BH charge are compared. The dotted black line indicates the radius of the Schwarzschild BH which does not depend on the charge, the dotted line is the RN BH, the blue lines are the two shadows obtained for the EH BH, the gray line is the BI BH shadow and the black line indicates the ModMax BH one. The dark gray and light gray bands correspond to the 1σ and 2σ, respectively, for the Sgr A^* BH. We are taking $M = 1$.

In Fig. 6.8 we compare the radius of the shadow of the BI BH for different values of the nonlinear parameter b. As the value of b increases, the radius of the shadow tends to the one of the RN BH, as expected, since in the limit $b \to \infty$ Maxwell electrodynamics is recovered. Lower values of b restrict the values of the charge Q of the BH; for example, for a value of $b = 0.1$ the maximum attainable charge for the radius of the shadow to be in the region 1σ is $Q = 0.37$.

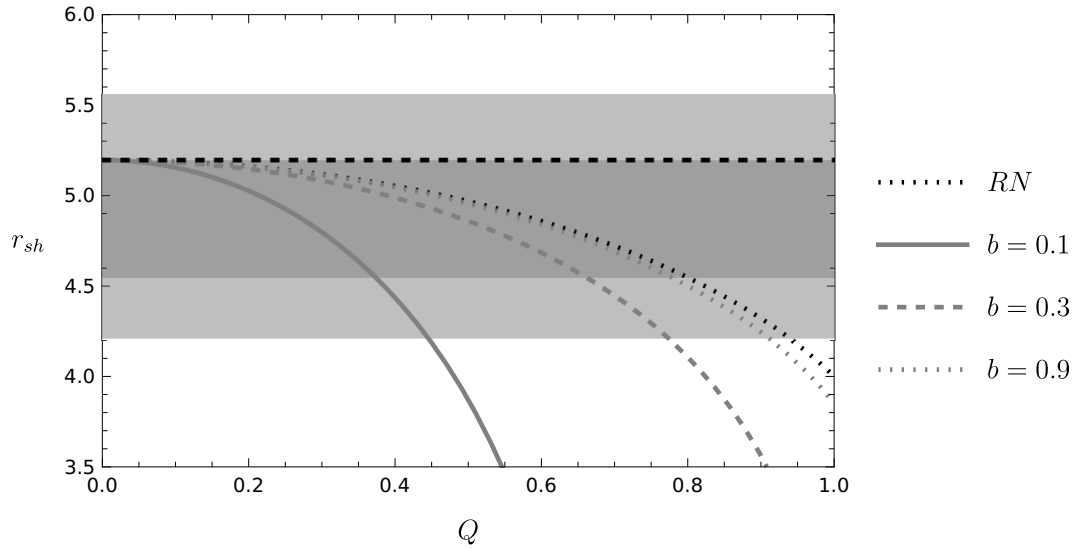

Figure 6.8: The shadow radius of the BI BH as a function of the BH charge is compared to RN BH. The dotted black line indicates the radius of the Schwarzschild BH, and the dotted line is the RN BH. The gray lines are the radius of the BI BH for different values of the nonlinear parameter b. The dark gray and light ray bands correspond to the 1σ and 2σ, respectively, for the Sgr A^* BH. We are taking $M = 1$.

In Fig. 6.9 we compare the radii of the shadow of the two solutions for the EH BH for different values of the nonlinear parameter μ. As the value of μ increases, the allowed values of the charge are more restricted, but the second solution (right plot) allows higher values of Q for the same values of μ. For instance, with $\mu = 5$, the limit value of the charge is $Q = 0.43$ for the first solution and $Q = 0.53$ for the second solution. Decreasing the values of μ we obtain similar limit values for the charge, for $\mu = 0.3$, the limiting value of the charge is $Q = 0.73$ for the first solution and $Q = 0.76$ for the second solution.

It is important to highlight that Figures 6.8 and 6.9 show that BI and EH nonlinear theories do not allow higher values of the charge according to the corresponding nonlinear parameters, then, if one looks for the existence of a charged black hole, neither BI or EH NLEDs are the theories that would help to achieve that, at least in the range of supermassive black holes.

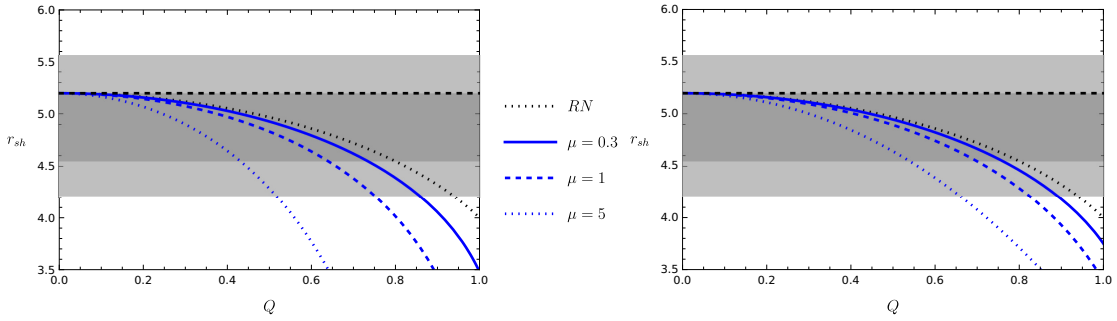

Figure 6.9: The shadow radius of the EH BH as a function of the BH charge Q is compared to RN BH. The dotted black line indicates the radius of the Schwarzschild BH, and the dotted line is the RN BH. The value lines are the radius of the EH BH for different values of the nonlinear parameter μ. The left-hand plot corresponds to the first solution for the radius of EH BH and the right-hand plot corresponds to the second solution for the radius of EH BH. The dark gray and light ray bands correspond to the 1σ and 2σ, respectively, for the Sgr A^* BH. We are taking $M = 1$.

Chapter 7

Conclusions

In studying light propagation in nonlinear electrodynamics (NLED), we considered three NLED theories: Born-Infeld (BI), Euler-Heisenberg (EH), and the more recent, modified Maxwell (ModMax). These theories model the effects produced in vacuum of intense electromagnetic fields; the effect of these intense fields in light propagation is the slowing down of the phase velocity. Another effect that arises due to the high intensities of the fields is birefringence in vacuum. For the NLED theories in consideration, only the BI theory does not present birefringence; and in the case of the ModMax theory, since it preserves conformal symmetry, one of the light trajectories coincides with the null geodesics of the background geometric metric, i.e. one of the two resulting optical effective metrics is the background metric. In Chapters 4, for BI, and 3, for EH, we considered uniform electric and/or magnetic fields in the Minkowski space as the background metric. While in Chapter 5, for the ModMax, we addressed a black hole background and compare the NLED effects with the ones for the linear solution of the Einstein-Maxwell equations, the Reissner-Nordstrom metric. In Chapter 6, we contrasted the slowing down of the phase velocities of the three NLED theories with the Minkowski metric as the background metric. We note that the diminishing in the phase velocity of the ModMax theory does not depend on the magnitude of the background fields as is the case of the two other NLEDs under study. The NLED theory that diminishes the phase velocity the most is the EH theory. It is important to note that when the fields satisfy

$B^2/b^2 \approx 10^{-2}$ and $\mu B^2 \approx 10^{-2}$ the diminishing in the velocities for BI and EH is similar; it is presented in Figure 6.1. Finally, in 6.2 we consider each of the three NLED coupled to Einstein equations and study the static spherically symmetric solution that in each case is a NLED charged black hole (previously known); then the radius of the shadow for each of the three NLED BHs is compared with the ones for RN and Schwarzschild BHs.

In this thesis, it was exploited the interpretation of the intense electromagnetic fields background as a medium; for the EH theory, we also modeled the case of a flowing medium, using a Lorentz boost on the effective metric and by writing the effective metric as a Paillevé-Lemaitre-Gullstrand (PLG) metric, it was identified the velocity of the propagating medium and the velocity of light through such a medium. It results that the effect of slowing down the wave is more efficient for a boost that is parallel to the propagating light. Moreover, when we compare the diminishing of the phase velocity in a Lorentz boosted frame, we conclude that the NLED most effective for diminishing the phase velocity is EH.

In Chapter 3 we analyzed the slowing down of an electromagnetic wave propagating through a very intense electromagnetic EH field background.

We presented the phase velocities of an electromagnetic wave propagating through an intense uniform magnetic or electric background according to the truncated Euler-Heisenberg Lagrangian; due to the wave-background interaction one electric longitudinal component, γE_w, arises affecting the polarization. The constant γ depends on three parameters: the velocity of the propagation, the magnetic background and the EH parameter $\gamma(\beta, B, \mu)$; if the magnetic field is such that there is no component perpendicular or parallel to the propagating direction, $B_\perp = 0$ or $B_\parallel = 0$, this effect does not occur and $\gamma = 0$.

Using the NLED effective metric approach [53], [54], [73], we derived birefringence and the two possible phase velocities of the propagating wave are presented. For intense magnetic background fields, but such that $B/B_{cr} \ll 1$ the velocities of the propagation slow down, diminishing to the order of hundred thousandths as B grows, this is illustrated in Fig. 3.2. The birefringence in the case of an electric uniform background is calculated as well.

By performing a Lorentz boost on the effective metric we model the situation of a flowing medium. By rescaling properly the coordinates of the effective metric it acquires the form

of a PLG metric, where the velocity of the propagating medium and the velocity of the perturbation through such a medium are identified. We present as an example the case of Lorentz boosts parallel and perpendicular to the propagating direction. The effect of slowing down the wave is more efficient for a boost that is parallel to the wave propagation.

In Chapter 4 we have considered an electromagnetic wave in the optical limit, i.e. a light ray, propagating through an intense uniform Born-Infeld (BI) background, and have determined the phase velocities measured by an accelerated observer. For the accelerated frame we have considered a Rindler spacetime. This situation also models an environment with a uniform gravitational field, according to the Einstein Equivalence Principle. The phase velocities are determined from the effective optical metric, which is equivalent to a curved spacetime produced by the presence of the intense BI magnetic or electric field.

Using the NLED effective optical metric approach [53], [54] and then applying a Rindler transformation, we obtain the phase velocity of the propagating wave from the null geodesics of the transformed effective optical metric. Our treatment is valid for very strong fields; if we consider, for instance, that $B^2/b^2 \approx 10^{-2}$, then the BI field is of the order of 10^{11} Tesla that is ten times the critical Schwinger field or $B_{\rm cr} \approx 10^9$ Tesla. We first considered a uniform BI magnetic background and then a purely electric background, and three different directions of the propagating wave, with the setting shown in Figure 4.3.

For the BI magnetic background, the phase velocity of the propagating light slows significantly for a wave moving in the same direction as the Rindler acceleration, diminishing as B grows; conversely, the phase velocity increases for a wave moving in the directions that are opposite and transversal to the Rindler acceleration, which we have considered as being $a\hat{z}$. The phase velocities depend on (aT) such that the effect of increasing the acceleration is the same as that of time elapsing. If the magnetic field component that is transversal to the acceleration vanishes, then neither the acceleration nor the BI field have effect on the phase velocity.

For fixed values of the BI magnetic field, the phase velocity of waves moving in the $+\hat{z}$ and $+\hat{x}$ directions decrease to zero and then increase again as aT increases, while the phase velocity of waves propagating in the $-z$ direction approaches the one in vacuum as aT increases. In

Figures 4.7 and 4.8, these behaviors are shown for the phase velocity squared. Recall that these are the velocities as measured by the accelerated observer, and the relative directions change as aT increases. Initially, the observer chases the light ray, and as it approaches the wave, the wave's velocity seems to decrease. Eventually, it is zero (the moment the observer reaches the wave), and then the relative direction changes as the observer moves away from the wave, then the wave's velocity starts to increase. Since the accelerated frame is no longer inertial, no special relativity light velocity invariance is expected.

We also addressed the situation of a propagating wave through an intense electric background field. The effect of the BI electric field (decreasing the phase velocity) is qualitatively very similar to the one of the BI magnetic background, and, in the approximation taken up to B^2/b^2 terms, the expressions for the phase velocities are the same apart from changing $B_i \mapsto E_i$. For $E_z = 0$ the decrease in velocity is maximized. The wave traveling in $-\hat{z}$ is not affected by the BI field and as aT increases the phase velocity reaches the one in vacuum. If the electric field component that is perpendicular to the acceleration vanishes, then there is no effect neither from the acceleration nor the BI field on the phase velocity, and its value is that in vacuum.

For strong fields, when B approaches the maximum attainable BI field b, the behavior of the phase velocities is quantitatively different depending on whether the background is electric or magnetic. The most effective for slowing down the phase velocity is the electric background, for all traveling directions of the light rays.

Finally, we analyzed the redshift of a light pulse sent from one accelerated object and received by another one when the light pulses travels through the BI magnetic background. From the trajectory of the pulse and the hyperbola worldline of the emitter and receiver, we determined the proper time intervals elapsing between the emission of the two pulses and then the proper time interval of the reception. Using these intervals we calculated the redshift. In the approximation of *weak* fields (still very intense) and small intervals of time the expression for the redshift shows two different contributions, one due to the acceleration of the frame and the other one produced by the presence of the BI magnetic background, resulting in a larger total redshift.

In Chapter 5 we study light propagation in the vicinity of the ModMax BH as the background metric and determine the two effective metrics. One of the effective metrics is the background metric as a consequence of the conformal invariance. We focus then on the second effective metric, $g_{\mu\nu}^{\text{eff}(1)}$ in our notation, which presents effects that cannot be deduced from the background metric.

The phase velocities of the two possible light trajectories in the vicinity of the ModMax BH are always slower than in the neighborhood of the Reissner-Nordstrom BH due to the screening of the charge. We note that while the light pulse moves in the radial direction there is no birefringence, only when the velocity has angular components birefringence appears.

Regarding light trajectories in the vicinity of the ModMax BH, there are two possible unstable circular orbits (UCO); the UCO that coincides with one of the corresponding background metrics, elapses between the ones corresponding to the RN and Schwarzschild BHs. The second UCO has a radius larger than the previously mentioned and therefore the distance to reach the horizon is larger.

The deflection angles were determined numerically in the regime of strong deflection and then analytically in the weak field limit using the Gauss-Bonnet theorem. From the numerical approach, for $g_{\mu\nu}^{\text{eff}(1)}$ we found a smaller deflection angle by a factor of $e^{-\gamma}$ additional to the screening of the charge. The effect of NLED on the effective metric $g_{\mu\nu}^{\text{eff}(2)}$ is only the screening of the BH charge. In the weak field limit, we verified that for an observer located at infinity, the light deflection angle is the same for the two effective metrics. The results for the weak deflection angle are in agreement with the ones presented in [70]. Moreover, we present a more accurate expression that includes three additional terms, resulting in a smaller deflection angle, showing that in [70] the deflection is overestimated.

The redshift measured by an observer in the vicinity of the BH and by another one located at infinity was determined, obtaining that the frequency measured by the former is larger than the frequency measured by the latter. Due to the existence of two effective metrics, there are two possible redshifts. In general the redshift produced by $g_{\mu\nu}^{\text{eff}(1)}$ is smaller than the one for the RN BH, while the one for the metric $g_{\mu\nu}^{\text{eff}(2)}$ is larger than the one for RN and smaller than the one of Schwarzschild BH.

The kinematic redshift, z_k is also presented, which is smaller than the previously described redshifts z.

The radii of the shadow for the effective metrics were analyzed. Our analysis for the effective metric $g^{\text{eff}(1)}_{\mu\nu}$ extended the one in [70], taking into account the second possible photon trajectory. We set constraints of acceptable pairs of BH charge and nonlinear parameter (Q, γ) that fall in the 1σ interval of the observations of the shadow of Sagittarius A^*. For RN BH the maximum acceptable BH charge is $Q = 0.8$; while for the ModMax BH, due to the screening, with $\gamma = 2$, higher charges of $Q \approx 1.1$ are allowed. For $\gamma > 3.6$ the ModMax BH shadow is indistinguishable from the Schwarzschild's shadow.

We emphasized that while the massless particle effects of the ModMax BH background metric (equivalently to $g^{\text{eff}(2)}_{\mu\nu}$) can be described as a transition from the RN BH to the Schwarzschild BH, and approaching Schwarzschild as γ increases, the results provided by the second effective metric ($g^{\text{eff}(1)}_{\mu\nu}$ in our work) for the photon behavior cannot be deduced from the geometric or background metric of the NLED BH. In Chapter 6 we compare the modifications of the phase velocities correspondent to the three nonlinear electrodynamics for the cases when no coordinate transformation is applied to the effective metrics, when applying a Lorentz boost, and as measured by an accelerated observer.

The plots that serve the comparison are done in terms of adimensional parameters μB^2 for EH and B^2/b^2 for BI. Still, it is important to keep in mind that the critical fields of both nonlinear theories have a difference of two orders of magnitude between them, being the BI theory the one with the larger critical field. Moreover, we determine that the Euler-Heisenberg theory is the most effective in slowing down the phase velocity as the background magnetic field increases, for all the coordinate transformations considered. We note that the ModMax theory modifies the phase velocities by establishing a new limit for it, the phase velocity is constant for a given magnetic background field and the diminishing in the value is due to the nonlinear parameter γ, as this parameter increases, the new limit for the phase velocity diminishes. When analyzing the modification of the phase velocities for a Lorentz boost, we note that this case is the most effective in diminishing the phase velocities. At the orders of magnitude considered, there is no difference in considering a magnetic or electric background.

We also analyze the case of the NLEDs coupled to gravity and compare the shadows of the black hole solutions, we can determine ranges for the nonlinear parameters μ for EH, b for BI, and γ for ModMax, for their shadows to be in agreement with the evidence of Sagittarius A^*. If one is looking for a charged BH, the most effective theory to do it is ModMax, as established in Chapter 5, this theory coupled with Einstein equations results in a metric function similar to the one for RN but with a screening charge, which allows larger values of the charge to agree with the observations for Sgr. A^*. Meanwhile, by modifying the BI and EH nonlinear parameters, we are not able to reach higher values of charge.

To compare of the effects of the EH and BI NLEDs, we expand the BI Lagrangian up to $1/b^4$ order and a term arises that depends on the two invariants squared,

$$L_{BI} = -\frac{F}{4} + \frac{1}{32b^2}\left(F^2 + G^2\right), \tag{7.0.1}$$

$$L_{EH} = -\frac{F}{4} + \frac{\mu}{4}\left(F^2 + \frac{7}{4}G^2\right). \tag{7.0.2}$$

In spite of the similarity, the question arises that birefringence does not happen in BI theory. In the absence of an experiment or observation that determines one or the other as the correct theory, we can give a possible explanation in the difference of ranges in which both theories apply, i.e. BI theory applies for fields of the order of $b = 10^{20}$V/m while EH was derived for the intensities of Schwinger fields, $E_{\rm cr} = 10^{18}$V/m. BI considers the nonlinear effects produced by photon splitting, while EH considers vacuum polarization. Another difference is the symmetries that both theories fulfill; the BI theory fulfills the duality invariance while the EH theory does not, this symmetry breaking might have its origin in the smaller intensities of the fields that it describes. Experiments like vacuum polarization or photon splitting could shed some light on whether one of the theories is more precise to use.

The research developed during the Ph.D. has been published in the papers

- E. Guzman-Herrera, N. Breton,
  "Euler–Heisenberg waves propagating in a magnetic background"
  Eur. Phys. J. C **81**, 115 (2021).
  DOI 10.1140/epjc/s10052-020-08783-1

- E. Guzman-Herrera, N. Breton,
  "Light Propagating in a Born–Infeld Background as Seen by an Accelerated Observer"
  Annalen Der Physik, **534**, 2200043 (2022).
  DOI 10.1002/andp.202200043

- E. Guzman-Herrera, N. Breton,
  "Light propagation in the vicinity of the ModMax black hole"
  Journal of Cosmology and Astroparticle Physics, JCAP **01**, 041 (2024) ,
  DOI 10.1088/1475-7516/2024/01/041

Chapter 8

Perspectives

- Since the effects of NLED can be modeled by curved geometries that resemble the behavior of linear electromagnetic fields in a material medium, the studied effects are of interest not only in the context of very intense electromagnetic fields. Wave propagation in material media is still a current and important theme of research, mainly because materials exhibiting new optical properties have been produced at an accelerated rate in material science laboratories. Thus, the theoretical description of new effects that can be produced in such materials could greatly impact the near-future conception of optical processes and technological devices (see for instance, ref. [125] for a review of magnetoelectric materials, and also refs. [126]–[132] for achievements and devices regarding metamaterials). One of the fundamental steps in this direction is the correlation between the optical effects and the corresponding optical coefficients in the expansion of the polarization and magnetization of the medium in powers of the electric and magnetic fields. After determining these correlations, the dispersion relation for the electromagnetic waves in the material leads to the formulation of analog models, opening a quite interesting window to investigate (in optical laboratories) phenomena predicted to occur in the context of other physical interactions (the most famous one is the well known Hawking radiation, whose optical analog has been measured in lab [133], [134]). We should also mention the great opportunity that the realm of metamaterials

offers to research in optics since it has expanded the phenomena that can be described (see ref. [135] for an extensive review of the subject). The demand for improved technological devices shows the importance of the study of the electromagnetic properties of matter under the influence of other electromagnetic fields [136]. Even analog models of gravity have contributed to the study of metamaterials due to the equivalence of light propagation through an optical material and the one in curved spacetimes. Advances in a general formalism to describe them can be consulted in[137].

Using the concept of effective geometry, the tensors that describe the properties of a given material (the susceptibility tensors) can be related to a geometry where wave propagation occurs along the same trajectories as the ones in the specific optical material. The background spacetime can be flat or curved. The effective geometry introduces extra contributions to the background metric adding information about the properties of the material medium. For a historical review of the use of effective geometry in optical materials see ref. [138], [139]. Research in this field takes advantage of the fact that, mathematically, electromagnetic fields propagating through some material media can be treated as propagating through an effective geometry. There are several tools to deal with the analogy; one of them is the so-called Transformation Optics [140] that considers that a curved path in a certain geometry is equivalent to a straight line in another geometry, and focuses on finding the right coordinates to transform the first geometry into the second one. For this reason, it turns out convenient to use the formalism of Maxwell's equations in arbitrary coordinates, and General Relativity comes in hand, in the sense of dealing with curved spacetimes. This method is useful if there is a coordinate transformation to apply to a background metric. But if instead there is a nonlinear Lagrangian for the physical system, the method established in ref. [55] can be used to derive an effective metric for light propagation in such a medium. The effective geometry can be used to relate the optical properties of the medium to the properties of the background metric, as in ref. [141] or in [140].

- Recently has been revisited the idea of NLED in the early universe where quantum corrections should be taken into account; in this context, Maxwell's electrodynamics

should be complemented with nonlinear electromagnetic effects. At those epochs, the nonlinear electromagnetic fields are strongly coupled to gravity, and induce a non-vanishing trace anomaly term (non-vanishing of the energy-momentum tensor trace) which is zero for a theory containing only massless fields, and nonzero for a theory containing massive field (or in a theory of gravity-NLED fields). The trace anomaly term which can be viewed as a quantum correction to the Einstein-Hilbert action and breaks the scale invariance in the NLED coupled to gravity theory, can generate negative pressures and hence drive the universe to accelerate. [142].

- There is also the subject of Emergent Cosmology models that use NLED to represent an Emergent universe. In [143] is considered inflationary expansion after Einstein's steady-state and cosmological parameters from observational PLANCK data exhibit some coincidences during inflation, in this situation NLED fields can also be considered as one of the causes of the accelerated expansion (inflation).

- In ref. [141] the consequences of birefringence of a light pulse in a curved background and the changes in the predictions of General Relativity are examined. In ref. [144], it is proposed a general ray tracing method for gradient-index media using Fermat's ray invariants. It is developed as an algorithm for any gradient-index distribution that possesses symmetry in a given curvilinear orthogonal coordinate system. The physical principles and calculations allow for further generalization of Snell's law to other variational principles or even to applications such as ray tracing in gradient-index media describing gravitational-like behavior to the human crystalline lens. In ref. [39] they report optical polarization measurements of an isolated neutron star, which is evidence for vacuum birefringence. In ref. [145] they obtain a metric relation that serves as a constitutive relation for electromagnetic fields in a material medium with superconductor properties. Our study of light propagating in NLED backgrounds can be enlarged in any of these directions.

Bibliography

[1] J. Agil, R. Battesti, and C. Rizzo, "On the speed of light in a vacuum in the presence of a magnetic field," *The European Physical Journal H*, vol. **48**, no. 1, p. 2, 2023. DOI: 10.1140/epjh/s13129-023-00050-7. [Online]. Available: https://doi.org/10.1140/epjh/s13129-023-00050-7.

[2] A. M. Smith, *From sight to light: The passage from ancient to modern optics*. University of Chicago Press, 2019.

[3] H. E. Burton, "The Optics of Euclid (English translation from Latin)," *Journal of Optical Society of America*, vol. **35**, no. 5, 1945. DOI: 10.1364/JOSA.35.000357. [Online]. Available: https://doi.org/10.1364/JOSA.35.000357.

[4] C. Rovelli, "Aristotle's Physics: A Physicist's look," *Journal of the American Philosophical Association*, vol. **1**, no. 1, pp. 23–40, 2015. DOI: 10.1017/apa.2014.11. [Online]. Available: https://doi.org/10.1017/apa.2014.11.

[5] T. A. Druart, *Al-Farabi on the Perfect State: Abū Naṣr al-Fārābı's Mabādi'Ārā'Ahl al-Madına al-Fāḍila*. JSTOR, 1986.

[6] N. El-Bizri, "In Defence of the Sovereignity of Phylosophy: Al-Baghdāsī's Critique of IBN Al-Haytham's Geometrisation of Place," *Arabic Sciences and Philosophy*, vol. **17**, no. 1, pp. 57–80, 2007. DOI: 10.1017/S0957423907000367. [Online]. Available: https://doi.org/10.1017/S0957423907000367.

[7] O. Roemer, "A demonstration concerning the motion of light," *Philosophical Transactions of the Royal Society*, vol. **12**, no. 136, p. 893, 1969. DOI: 10.1098/rstl.1677.0024. [Online]. Available: https://doi.org/10.1098/rstl.1677.0024.

[8] D. Halliday, R. Resnick, and K. S. Krane, *Fisica*. LTC, 1984, vol. **1**.

[9] N. J. Wade, "Light and sight since antiquity," *Perception*, vol. **27**, no. 6, pp. 637–670, 1998. DOI: 10.1068/p270637. [Online]. Available: https://doi.org/10.1068/p270637.

[10] J. Z. Buchwald and R. Fox, *The Oxford Handbook of the History of Physics*. OUP Oxford, 2013, vol. **48**.

[11] H. Wild, "Untersuchungen über die Identität von Lichtäther und elektrischem Fluidum," *Annalen der Physik*, vol. **200**, no. 3, pp. 507–512, 1865. DOI: 10.1002/andp.18652000313. [Online]. Available: https://doi.org/10.1002/andp.18652000313.

[12] A. Roiti, "1st der elektrische Strom ein Aetherstrom?" *Annalen der Physik*, vol. **226**, no. 9, pp. 164–171, 1873. DOI: 10.1002/andp.18732260912. [Online]. Available: https://doi.org/10.1002/andp.18732260912.

[13] A. Roiti, "Se la corrente elettrica sia una corrente di etere," *Il Nuovo Cimento (1869-1876)*, vol. **9**, no. 1, pp. 148–153, 1873.

[14] E. Lecher, "Einige elektrische Versuche mit negativem Resultate," *Repertorium der Physik*, vol. **20**, pp. 151–153, 1884.

[15] O. J. Lodge, "VI. Experiments on the absence of mechanical connexion between ether and matter," *Philosophical Transactions of the Royal Society of London. Series A, Containing Papers of a Mathematical or Physical Character*, vol. 1, no. 189, pp. 149–166, 1897. DOI: 10.1098/rsta.1897.0006. [Online]. Available: https://doi.org/10.1098/rsta.1897.0006.

[16] J. Schwinger, "On gauge invariance and vacuum polarization," *Physical Review*, vol. **82**, no. 5, p. 664, 1951. DOI: 10.1103/PhysRev.82.664. [Online]. Available: https://doi.org/10.1103/PhysRev.82.664.

[17] M. Born and L. Infeld, "Foundations of the new field theory," *Proceedings of the Royal Society of London. Series A, Containing Papers of a Mathematical and Physical Character*, vol. **144**, no. 852, pp. 425–451, 1934. DOI: 10.1098/rspa.1934.0059. [Online]. Available: https://doi.org/10.1098/rspa.1934.0059.

[18] E. Heisenberg and H. Euler, "Folgerungen aus der Diracshen Theorie des Positrons," *Zeitschrift fur Physik*, vol. **98**, pp. 714–732, 1936. DOI: 10.1007/BF01343663. [Online]. Available: https://doi.org/10.1007/BF01343663.

[19] H. Euler and B. Kockel, "The scattering of light by light in Dirac's theory," *Naturwissenschaften*, vol. **23**, no. 15, pp. 246–247, 1935. DOI: 10.1007/BF01493898. [Online]. Available: https://doi.org/10.1007/BF01493898.

[20] G. V. Dunne, "The Heisenberg-Euler effective action: 75 Years on," *International Journal of Modern Physics: Conference Series*, vol. **14**, pp. 42–56, 2012. DOI: 10.1142/S2010194512007222. [Online]. Available: https://doi.org/10.1142/S2010194512007222.

[21] V. Weisskopf, "The electrodynamics of the vacuum based on the quantum theory of the electron," *Kong. Dan. Vid. Sel. Mat. Fys. Med.*, vol. **14N6**, no. 6, pp. 1–39, 1936. DOI: 10.1017/CBO9780511608223.018. [Online]. Available: https://doi.org/10.1017/CBO9780511608223.018.

[22] M. Fouché, R. Battesti, and C. Rizzo, "Limits on nonlinear electrodynamics," *Physical Review D*, vol. **93**, no. 9, p. 093 020, 2016. DOI: 10.1103/PhysRevD.93.093020. [Online]. Available: https://doi.org/10.1103/PhysRevD.93.093020.

[23] I. Soares, R. Turcati, and S. B. Duarte, "Thermodynamics of blackbody radiation in nonlinear electrodynamics," *Physical Review D*, vol. **108**, no. 4, 043020, p. 043 020, Aug. 2023. DOI: 10.1103/PhysRevD.108.043020. arXiv: 2302.04367. [Online]. Available: https://doi.org/10.1103/PhysRevD.108.043020.

[24] R. Cameron, G. Cantatore, A. C. Melissinos, *et al.*, "Search for nearly massless, weakly coupled particles by optical techniques," *Physical Review D*, vol. **47**, pp. 3707–3725, 9 May 1993. DOI: 10.1103/PhysRevD.47.3707. [Online]. Available: https://link.aps.org/doi/10.1103/PhysRevD.47.3707.

[25] E. Zavattini, G. Zavattini, G. Ruoso, *et al.*, "New PVLAS results and limits on magnetically induced optical rotation and ellipticity in vacuum," *Physical Review D*, vol. **77**, p. 032 006, 3 Feb. 2008. DOI: 10.1103/PhysRevD.77.032006. [Online]. Available: https://link.aps.org/doi/10.1103/PhysRevD.77.032006.

[26] G. Zavattini, U. Gastaldi, R. Pengo, G. Ruoso, F. D. Valle, and E. Milotti, "Measuring the magnetic birefringence of vacuum: the PVLAS experiment," *International Journal of Modern Physics A*, vol. **27**, no. 15, p. 1 260 017, 2012. DOI: 10.1142/S0217751X12600172. [Online]. Available: https://doi.org/10.1142/S0217751X12600172.

[27] A. Ejlli, F. Della Valle, U. Gastaldi, *et al.*, "The PVLAS experiment: A 25 year effort to measure vacuum magnetic birefringence," *Physics Reports*, vol. **871**, pp. 1–74, 2020, The PVLAS experiment: A 25 year effort to measure vacuum magnetic birefringence, ISSN: 0370-1573. DOI: 10.1016/j.physrep.2020.06.001. [Online]. Available: https://doi.org/10.1016/j.physrep.2020.06.001.

[28] A. Cadène, P. Berceau, M. Fouché, R. Battesti, and C. Rizzo, "Vacuum magnetic linear birefringence using pulsed fields: status of the BMV experiment," *The European Physical Journal D*, vol. **68**, pp. 1–7, 2014. DOI: 10.1140/epjd/e2013-

40725-9. [Online]. Available: https://doi.org/10.1140/epjd/e2013-40725-9.

[29] G. Brodin, M. Marklund, and L. Stenflo, "Proposal for detection of QED vacuum nonlinearities in Maxwell's equations by the use of waveguides," *Physical Review Letters*, vol. **87**, no. 17, p. 171 801, 2001. DOI: 10.1103/PhysRevLett.87.171801. [Online]. Available: https://doi.org/10.1103/PhysRevLett.87.171801.

[30] F. Gelis and N. Tanji, "Schwinger mechanism revisited," *Progress in Particle and Nuclear Physics*, vol. **87**, pp. 1–49, 2016, ISSN: 0146-6410. DOI: 10.1016/j.ppnp.2015.11.001. [Online]. Available: https://doi.org/10.1016/j.ppnp.2015.11.001.

[31] N. Ahmadiniaz, T. E. Cowan, R. Sauerbrey, U. Schramm, H.-P. Schlenvoigt, and R. Schützhold, "Heisenberg limit for detecting vacuum birefringence," *Physical Review D*, vol. 101, no. 11, p. 116 019, 2020. DOI: 10.1103/PhysRevD.101.116019. [Online]. Available: https://doi.org/10.1103/PhysRevD.101.116019.

[32] A. Collaboration, "Evidence for light-by-light scattering in heavy-ion collisions with the ATLAS detector at the LHC," *Nature physics*, vol. **13**, no. 9, pp. 852–858, 2017. DOI: 10.1038/nphys4208. [Online]. Available: https://doi.org/10.1038/nphys4208.

[33] D. d'Enterria and G. G. da Silveira, "Observing Light-by-Light Scattering at the Large Hadron Collider," *Phys. Rev. Lett.*, vol. **111**, p. 080 405, 8 Aug. 2013. DOI: 10.1103/PhysRevLett.111.080405. [Online]. Available: https://link.aps.org/doi/10.1103/PhysRevLett.111.080405.

[34] S. Z. Akhmadaliev, G. Y. Kezerashvili, S. G. Klimenko, *et al.*, "Experimental investigation of high-energy photon splitting in atomic fields," *Physical Review*

Letters, vol. **89**, no. 6, p. 061 802, 2002. DOI: 10.1103/PhysRevLett.89.061802. [Online]. Available: https://doi.org/10.1103/PhysRevLett.89.061802.

[35] J. M. Dávila, C. Schubert, and M. A. Trejo, "Photonic processes in Born-Infeld theory," *International Journal of Modern Physics A*, vol. **29**, no. 30, p. 1 450 174, 2014. DOI: 10.48550/arXiv.1310.8410. [Online]. Available: https://doi.org/10.48550/arXiv.1310.8410.

[36] A. Fedotov, A. Ilderton, F. Karbstein, *et al.*, "Advances in QED with intense background fields," *Physics Reports*, vol. **1010**, pp. 1–138, 2023. DOI: 10.1016/j.physrep.2023.01.003. [Online]. Available: https://doi.org/10.1016/j.physrep.2023.01.003.

[37] L. Schoeffel, C. Baldenegro, H. Hamdaoui, S. Hassani, C. Royon, and M. Saimpert, "Photon–photon physics at the lhc and laser beam experiments, present and future," *Progress in Particle and Nuclear Physics*, vol. 120, p. 103 889, 2021. DOI: 10.1016/j.ppnp.2021.103889. [Online]. Available: https://doi.org/10.1016/j.ppnp.2021.103889.

[38] M. G. Baring, "Photon splitting and pair conversion in strong magnetic fields," in *AIP Conference Proceedings*, American Institute of Physics, vol. **1051**, 2008, pp. 53–64. DOI: 10.1063/1.3020681. [Online]. Available: https://doi.org/10.1063/1.3020681.

[39] R. P. Mignani, V. Testa, D. González-Caniulef, *et al.*, "Evidence for vacuum birefringence from the first optical polarimetry measurement of the isolated neutron star RX J1856. 5- 3754," *Monthly Notices of the Royal Astronomical Society*, vol. **465**, p. 2798, 2016. DOI: 10.1093/mnras/stw2798. [Online]. Available: https://doi.org/10.1093/mnras/stw2798.

[40] V. I. Ritus, "Radiative corrections in quantum electrodynamics with intense field and their analytical properties," *Annals of Physics*, vol. **69**, no. 2, pp. 555–

582, 1972. DOI: 10.1016/0003-4916(72)90191-1. [Online]. Available: https://doi.org/10.1016/0003-4916(72)90191-1.

[41] Z. Bialynicka-Birula and I. Bialynicki-Birula, "Nonlinear effects in quantum electrodynamics. Photon propagation and photon splitting in an external field," *Physical Review D*, vol. **2**, no. 10, p. 2341, 1970. DOI: 10.1103/PhysRevD.2.2341. [Online]. Available: https://doi.org/10.1103/PhysRevD.2.2341.

[42] S. Hu and B. Liu, "Birefringence and non-transversality of light propagation in an ultra-strongly magnetized vacuum," *Journal of Physics A: Mathematical and Theoretical*, vol. **40**, no. 46, p. 13 859, 2007. DOI: 10.1088/1751-8113/40/46/003. [Online]. Available: https://doi.org/10.1088/1751-8113/40/46/003.

[43] E. Guzman-Herrera and N. Breton, "Euler-Heisenberg waves propagating in a magnetic background," *The European Physical Journal C*, vol. **81**, pp. 1–8, 2021. DOI: 10.1140/epjc/s10052-020-08783-1. [Online]. Available: https://doi.org/10.1140/epjc/s10052-020-08783-1.

[44] M. Aiello, G. R. Bengochea, and R. Ferraro, "Anisotropic effects of background fields on Born–Infeld electromagnetic waves," *Physics Letters A*, vol. **361**, no. 1-2, pp. 9–12, 2007. DOI: 10.1016/j.physleta.2006.09.027. [Online]. Available: https://doi.org/10.1016/j.physleta.2006.09.027.

[45] V. Perlick, O. Y. Tsupko, and G. S. Bisnovatyi-Kogan, "Influence of a plasma on the shadow of a spherically symmetric black hole," *Physical Review D*, vol. **92**, no. 10, p. 104 031, 2015. DOI: 10.1103/PhysRevD.92.104031. [Online]. Available: https://doi.org/10.1103/PhysRevD.92.104031.

[46] S. Robertson, A. Mailliet, X. Sarazin, *et al.*, "Experiment to observe an optically induced change of the vacuum index," *Physical Review A*, vol. **103**, no. 2, p. 023 524, 2021. DOI: 10.1103/PhysRevA.103.023524. [Online]. Available: https://doi.org/10.1103/PhysRevA.103.023524.

[47] P. Gaete and J. A. Helayël-Neto, "A note on nonlinear electrodynamics," *Europhysics Letters*, vol. **119**, no. 5, p. 51 001, Nov. 2017. DOI: 10.1209/0295-5075/119/51001. [Online]. Available: https://doi.org/10.1209/0295-5075/119/51001.

[48] J. J. Klein and B. P. Nigam, "Birefringence of the Vacuum," *Phys. Rev.*, vol. **135**, B1279–B1280, 5B Sep. 1964. DOI: 10.1103/PhysRev.135.B1279. [Online]. Available: https://doi.org/10.1103/PhysRev.135.B1279.

[49] Y. N. Obukhov and G. F. Rubilar, "Fresnel analysis of wave propagation in nonlinear electrodynamics," *Physical Review D*, vol. **66**, no. 2, p. 024 042, 2002. DOI: 10.1103/PhysRevD.66.024042. [Online]. Available: https://doi.org/10.1103/PhysRevD.66.024042.

[50] A. N. Luiten and J. C. Petersen, "Detection of vacuum birefringence using intense laser pulses," *Physics Letters A*, vol. **330**, no. 6, pp. 429–434, 2004, ISSN: 0375-9601. DOI: 10.1016/j.physleta.2004.08.020. [Online]. Available: https://doi.org/10.1016/j.physleta.2004.08.020.

[51] V. Perlick, C. Lämmerzahl, and A. Macías, "Effects of nonlinear vacuum electrodynamics on the polarization plane of light," *Physical Review D*, vol. **98**, p. 105 014, 10 Nov. 2018. DOI: 10.1103/PhysRevD.98.105014. [Online]. Available: https://doi.org/10.1103/PhysRevD.98.105014.

[52] E. Goulart and S. E. Perez-Bergliaffa, "Nonlinear electrodynamics nonminimally coupled to gravity: Symmetric-hyperbolicity and causal structure," *Physical Review. D*, vol. **105**, p. 024 021, 2 Jan. 2022. DOI: 10.1103/PhysRevD.105.024021. [Online]. Available: https://doi.org/10.1103/PhysRevD.105.024021.

[53] M. Novello, V. A. De Lorenci, J. M. Salim, and R. Klippert, "Geometrical aspects of light propagation in nonlinear electrodynamics," *Physical Review D*, vol. **61**,

no. 4, p. 045 001, 2000. DOI: 10.1103/PhysRevD.61.045001. [Online]. Available: https://doi.org/10.1103/PhysRevD.61.045001.

[54] S. Alarcón Gutiérrez, A. L. Dudley, and J. F. Plebañski, "Signals and discontinuities in general relativistic nonlinear electrodynamics," *Journal of Mathematical Physics*, vol. **22**, no. 12, pp. 2835–2848, Dec. 1981, ISSN: 0022-2488. DOI: 10.1063/1.524874. [Online]. Available: https://doi.org/10.1063/1.524874.

[55] V. De Lorenci, R. Klippert, M. Novello, and J. Salim, "Light propagation in nonlinear electrodynamics," *Physics Letters B*, vol. **482**, no. 1, pp. 134–140, 2000, ISSN: 0370-2693. DOI: 10.1016/S0370-2693(00)00522-0. [Online]. Available: https://doi.org/10.1016/S0370-2693(00)00522-0.

[56] S. I. Tzenov, K. M. Spohr, and K. A. Tanaka, "Dispersion properties, nonlinear waves and birefringence in classical nonlinear electrodynamics," *Journal of Physics Communications*, vol. **4**, no. 2, p. 025 006, 2020. DOI: 10.1088/2399-6528/ab72c7. [Online]. Available: https://doi.org/10.1088/2399-6528/ab72c7.

[57] G. V. Dunne and Z. Harris, "Higher-loop Euler-Heisenberg transseries structure," *Physical Review D*, vol. **103**, no. 6, p. 065 015, 2021. DOI: 10.1103/PhysRevD.103.065015. [Online]. Available: https://doi.org/10.1103/PhysRevD.103.065015.

[58] P. V. Sasorov, F. Pegoraro, T. Z. Esirkepov, and S. V. Bulanov, "Generation of high order harmonics in Heisenberg–Euler electrodynamics," *New Journal of Physics*, vol. **23**, no. 10, p. 105 003, 2021. DOI: 10.1088/1367-2630/ac28cb. [Online]. Available: https://doi.org/10.1088/1367-2630/ac28cb.

[59] A. Rebhan and G. Turk, "Polarization effects in light-by-light scattering: Euler–Heisenberg versus Born–Infeld," *International Journal of Modern Physics A*,

vol. **32**, no. 10, p. 1 750 053, 2017. DOI: 10.1142/S0217751X17500531. [Online]. Available: https://doi.org/10.1142/S0217751X17500531.

[60] H. Kadlecová, "On the absence of shock waves and vacuum birefringence in Born–Infeld electrodynamics," *Journal of Mathematical Physics*, vol. **65**, no. 1, p. 012 302, Jan. 2024, ISSN: 0022-2488. DOI: 10.1063/5.0150790. [Online]. Available: https://doi.org/10.1063/5.0150790.

[61] I. Bandos, K. Lechner, D. Sorokin, and P. K. Townsend, "Nonlinear duality-invariant conformal extension of Maxwell's equations," *Physical Review D*, vol. **102**, p. 121 703, 12 Dec. 2020. DOI: 10.1103/PhysRevD.102.121703. [Online]. Available: https://doi.org/10.1103/PhysRevD.102.121703.

[62] A. Banerjee and A. Mehra, "Maximally symmetric nonlinear extension of electrodynamics with Galilean conformal symmetries," *Physical Review D*, vol. **106**, p. 085 005, 8 Sep. 2022. DOI: 10.1103/PhysRevD.106.085005. [Online]. Available: https://doi.org/10.1103/PhysRevD.106.085005.

[63] M. J. Neves, P. Gaete, L. P. R. Ospedal, and J. A. Helayël-Neto, "Considerations on the modified Maxwell electrodynamics in the presence of an electric and magnetic background," *Physical Review D*, vol. **107**, p. 075 019, 7 Apr. 2023. DOI: 10.1103/PhysRevD.107.075019. [Online]. Available: https://doi.org/10.1103/PhysRevD.107.075019.

[64] C. A. Escobar and R. Linares, "Spontaneous symmetry breaking in models with second-class constraints," *Physical Review D*, vol. **106**, p. 036 027, 3 Aug. 2022. DOI: 10.1103/PhysRevD.106.036027. [Online]. Available: https://doi.org/10.1103/PhysRevD.106.036027.

[65] I. Bandos, K. Lechner, D. Sorokin, and et al., "On p-form gauge theories and their conformal limits," *Journal of High Energy Physics*, vol. **22**, 2021. DOI:

10.1007/JHEP03(2021)022. [Online]. Available: https://doi.org/10.1007/JHEP03(2021)022.

[66] I. Bandos, L. K., D. Sorokin, and T. P. K., "ModMax meets SUSY," *Journal of High Energy Physics*, vol. **2021**, no. 10, pp. 1–32, 2021. DOI: 10.1007/JHEP10(2021)031. [Online]. Available: https://doi.org/10.1007/JHEP10(2021)031.

[67] J. Barrientos, A. Cisterna, D. Kubizňák, and J. Oliva, "Accelerated black holes beyond Maxwell's electrodynamics," *Physics Letters B*, vol. **834**, p. 137 447, 2022, ISSN: 0370-2693. DOI: 10.1016/j.physletb.2022.137447. [Online]. Available: https://doi.org/10.1016/j.physletb.2022.137447.

[68] A. Ballon Bordo, D. Kubizňák, and T. R. Perche, "Taub-NUT solutions in conformal electrodynamics," *Physics Letters B*, vol. **817**, p. 136 312, 2021, ISSN: 0370-2693. DOI: 10.1016/j.physletb.2021.136312. [Online]. Available: https://doi.org/10.1016/j.physletb.2021.136312.

[69] A. Bokulić, I. Smolić, and T. Jurić, "Black hole thermodynamics in the presence of nonlinear electromagnetic fields," *Physical Review D*, vol. **103**, p. 124 059, 12 Jun. 2021. DOI: 10.1103/PhysRevD.103.124059. [Online]. Available: https://doi.org/10.1103/PhysRevD.103.124059.

[70] R. C. Pantig, L. Mastrototaro, G. Lambiase, and A. Övgün, "Shadow, lensing, quasinormal modes, greybody bounds and neutrino propagation by dyonic ModMax black holes," *The European Physical Journal C*, vol. **82**, no. 12, p. 1155, 2022. DOI: 10.1140/epjc/s10052-022-11125-y. [Online]. Available: https://doi.org/10.1140/epjc/s10052-022-11125-y.

[71] H. Babaei-Aghbolagh, K. B. Velni, D. M. Yekta, and H. Mohammadzadeh, "Marginal $T\overline{T}$-like deformation and modified Maxwell theories in two dimensions," *Physical Review D*, vol. **106**, p. 086 022, 8 Oct. 2022. DOI: 10.1103/

PhysRevD.106.086022. [Online]. Available: https://doi.org/10.1103/PhysRevD.106.086022.

[72] G. Boillat, "Nonlinear Electrodynamics: Lagrangians and Equations of Motion," *Journal of Mathematical Physics*, vol. **11**, no. 3, pp. 941–951, Oct. 2003, ISSN: 0022-2488. DOI: 10.1063/1.1665231. eprint: https://pubs.aip.org/aip/jmp/article-pdf/11/3/941/8145096/941_1_online.pdf. [Online]. Available: https://doi.org/10.1063/1.1665231.

[73] S. Liberati, S. Sonego, and M. Visser, "Scharnhorst effect at oblique incidence," *Physical Review D*, vol. **63**, no. 8, p. 085 003, 2001. DOI: 10.1103/PhysRevD.63.085003. [Online]. Available: https://doi.org/10.1103/PhysRevD.63.085003.

[74] E. Goulart and S. E. Perez-Bergliaffa, "A classification of the effective metric in nonlinear electrodynamics," *Classical and Quantum Gravity*, vol. **26**, no. 13, p. 135 015, 2009. DOI: 10.1088/0264-9381/26/13/135015. [Online]. Available: https://doi.org/10.1088/0264-9381/26/13/135015.

[75] H. Gies and F. Karbstein, "An Addendum to the Heisenberg-Euler effective action beyond one loop," *Journal of High Energy Physics*, vol. **2017**, no. 3, pp. 1–35, 2017. DOI: 10.1007/JHEP03(2017)108. [Online]. Available: https://doi.org/10.1007/JHEP03(2017)108.

[76] F. Karbstein, "All-loop result for the strong magnetic field limit of the Heisenberg-Euler Effective lagrangian," *Physical Review Letters*, vol. **122**, no. 21, p. 211 602, 2019. DOI: 10.1103/PhysRevLett.122.211602. [Online]. Available: https://doi.org/10.1103/PhysRevLett.122.211602.

[77] S. L. Adler, J. N. Bahcall, C. G. Callan, and M. N. Rosenbluth, "Photon splitting in a strong magnetic field," *Physical Review Letters*, vol. **25**, no. 15, p. 1061, 1970. DOI: 10.1103/PhysRevLett.25.1061. [Online]. Available: https://doi.org/10.1103/PhysRevLett.25.1061.

[78] T. Gold, "Rotating neutron stars as the origin of the pulsating radio sources," *Nature*, vol. **218**, no. 5143, pp. 731–732, 1968. DOI: 10.1038/218731a0. [Online]. Available: https://doi.org/10.1038/218731a0.

[79] I. A. Batalin and A. E. Shabad, "Green's Function of a Photon in a Constant Homogeneous Electromagnetic Field of General Form," *Zh. Eksp. Teor. Fiz*, vol. **60**, pp. 894–900, 1971.

[80] E. Brezin and C. Itzykson, "Polarization phenomena in vacuum nonlinear electrodynamics," *Physical Review D*, vol. **3**, no. 2, p. 618, 1971. DOI: 10.1103/PhysRevD.3.618. [Online]. Available: https://doi.org/10.1103/PhysRevD.3.618.

[81] F. Karbstein, "Photon polarization tensor in a homogeneous magnetic or electric field," *Physical Review D*, vol. **88**, no. 8, p. 085 033, 2013. DOI: 10.1103/PhysRevD.88.085033. [Online]. Available: https://doi.org/10.1103/PhysRevD.88.085033.

[82] H. Gies, "Strong laser fields as a probe for fundamental physics," *The European Physical Journal D*, vol. **55**, pp. 311–317, 2009. DOI: 10.1140/epjd/e2009-00006-0. [Online]. Available: https://doi.org/10.1140/epjd/e2009-00006-0.

[83] F. Karbstein, "Probing vacuum polarization effects with high-intensity lasers," *Particles*, vol. **3**, no. 1, pp. 39–61, 2020. DOI: 10.3390/particles3010005. [Online]. Available: https://doi.org/10.3390/particles3010005.

[84] R. Aguero-Santacruz and D. Bermudez, "Hawking radiation in optics and beyond," *Philosophical Transactions of the Royal Society A*, vol. **378**, no. 2177, p. 20 190 223, 2020. DOI: 10.1098/rsta.2019.0223. [Online]. Available: https://doi.org/10.1098/rsta.2019.0223.

[85] D. G. Boulware, "Radiation from a uniformly accelerated charge," *Annals of Physics*, vol. **124**, no. 1, pp. 169–188, 1980. DOI: 10.1016/0003-4916(80)90360-7. [Online]. Available: https://doi.org/10.1016/0003-4916(80)90360-7.

[86] A. Gupta and T. Padmanabhan, "Radiation from a charged particle and radiation reaction reexamined," *Physical Review D*, vol. **57**, no. 12, p. 7241, 1998. DOI: 10.1103/PhysRevD.57.7241. [Online]. Available: https://doi.org/10.1103/PhysRevD.57.7241.

[87] C. De Almeida and A. Saa, "The radiation of a uniformly accelerated charge is beyond the horizon: A simple derivation," *American Journal of Physics*, vol. **74**, no. 2, pp. 154–158, 2006. DOI: 10.1119/1.2162548. [Online]. Available: https://doi.org/10.1119/1.2162548.

[88] D. Koks, "The Uniformly Accelerated Frame as a Test Bed for Analysing the Gravitational Redshift," *Universe*, vol. **7**, no. 1, p. 4, 2020. DOI: 10.3390/universe7010004. [Online]. Available: https://doi.org/10.3390/universe7010004.

[89] J. B. Formiga and C. Romero, "On the spectral shift and the time delay of light in a Rindler accelerated frame," *International Journal of Modern Physics D*, vol. **16**, no. 04, pp. 699–709, 2007. DOI: 10.1142/S021827180700984X. [Online]. Available: https://doi.org/10.1142/S021827180700984X.

[90] J. D. Hamilton, "The uniformly accelerated reference frame," *American Journal of Physics*, vol. **46**, no. 1, pp. 83–89, 1978. DOI: 10.1119/1.11169. [Online]. Available: https://doi.org/10.1119/1.11169.

[91] M. Aiello, G. R. Bengochea, and R. Ferraro, "Luminosity distance for Born–Infeld electromagnetic waves propagating in a cosmological magnetic background," *Journal of Cosmology and Astroparticle Physics*, vol. **2008**, no. 06, p. 006, 2008.

DOI: 0.1088/1475-7516/2008/06/006. [Online]. Available: https://doi.org/0.1088/1475-7516/2008/06/006.

[92] M. Alberici, "Measures and metrics in uniform gravitational fields," *arXiv preprint gr-qc/0503092*, 2005. DOI: 10.48550/arXiv.gr-qc/0503092. [Online]. Available: https://doi.org/10.48550/arXiv.gr-qc/0503092.

[93] D. Flores-Alfonso, B. A. González-Morales, R. Linares, and M. Maceda, "Black holes and gravitational waves sourced by non-linear duality rotation-invariant conformal electromagnetic matter," *Physics Letters B*, vol. **812**, p. 136 011, 2021. DOI: 10.1016/j.physletb.2020.136011. [Online]. Available: https://doi.org/10.1016/j.physletb.2020.136011.

[94] B. P. Kosyakov, "Nonlinear electrodynamics with the maximum allowable symmetries," *Physics Letters B*, vol. **810**, p. 135 840, 2020, ISSN: 0370-2693. DOI: 10.1016/j.physletb.2020.135840. [Online]. Available: https://doi.org/10.1016/j.physletb.2020.135840.

[95] J. D. Jackson, *Classical electrodynamics*. John Wiley & Sons, 1999.

[96] P. Pergola, "Modified Maxwell theory and its applications," Ph.D. dissertation, Universita Degli Studi de Padova, 2021. [Online]. Available: hdl.handle.net/20.500.12608/7984.

[97] D. P. Sorokin, "Introductory notes on non-linear electrodynamics and its applications," *Fortschritte der Physik*, vol. 70, no. 7-8, p. 2 200 092, 2022. DOI: https://doi.org/10.1002/prop.202200092. [Online]. Available: https://onlinelibrary.wiley.com/doi/abs/10.1002/prop.202200092.

[98] S. Chandrasekhar, *The mathematical theory of black holes*. Oxford University Press, 1985, vol. **69**. DOI: 10.1007/978-94-009-6469-3_2. [Online]. Available: https://doi.org/10.1007/978-94-009-6469-3_2.

[99] D. Amaro and A. Macías, "Exact lens equation for the Einstein-Euler-Heisenberg static black hole," *Physical Review D*, vol. **106**, no. 6, p. 064 010, 2022. DOI: 10.1103/PhysRevD.106.064010. [Online]. Available: https://doi.org/10.1103/PhysRevD.106.064010.

[100] E. F. Eiroa, G. E. Romero, and D. F. Torres, "Reissner-Nordström black hole lensing," *Physical Review D*, vol. **66**, no. 2, p. 024 010, 2002. DOI: 10.1103/PhysRevD.66.024010. [Online]. Available: https://doi.org/10.1103/PhysRevD.66.024010.

[101] F. Zhao, J. Tang, and F. He, "Gravitational lensing effects of a Reissner–Nordstrom–de Sitter black hole," *Physical Review D*, vol. **93**, no. 12, p. 123 017, 2016. DOI: 10.1103/PhysRevD.93.123017. [Online]. Available: https://doi.org/10.1103/PhysRevD.93.123017.

[102] V. Bozza, "Gravitational lensing in the strong field limit," *Physical Review D*, vol. **66**, no. 10, p. 103 001, 2002. DOI: 10.1103/PhysRevD.66.103001. [Online]. Available: https://doi.org/10.1103/PhysRevD.66.103001.

[103] N. Tsukamoto, "Gravitational lensing by a photon sphere in a Reissner-Nordström naked singularity spacetime in strong deflection limits," *Physical Review D*, vol. **104**, no. 12, p. 124 016, 2021. DOI: 10.1103/PhysRevD.104.124016. [Online]. Available: https://doi.org/10.1103/PhysRevD.104.124016.

[104] J. Jia and K. Huang, "Perturbative deflection angle, gravitational lensing in the strong field limit and the black hole shadow," *The European Physical Journal C*, vol. **81**, pp. 1–12, 2021. DOI: 10.1140/epjc/s10052-021-09026-7. [Online]. Available: https://doi.org/10.1140/epjc/s10052-021-09026-7.

[105] X. Pang and J. Jia, "Gravitational lensing of massive particles in Reissner–Nordström black hole spacetime," *Classical and Quantum Gravity*, vol. **36**, no. 6,

p. 065 012, 2019. DOI: 10.1088/1361-6382/ab0512. [Online]. Available: https://doi.org/10.1088/1361-6382/ab0512.

[106] S. Weinberg, *Gravitation and cosmology: principles and applications of the general theory of relativity*. John Wiley & Sons, 2004.

[107] G. W. Gibbons and M. C. Werner, "Applications of the Gauss-Bonnet theorem to gravitational lensing," *Classical and Quantum Gravity*, vol. **25**, no. 23, p. 235 009, 2008. DOI: 10.1088/0264-9381/25/23/235009. [Online]. Available: https://doi.org/10.1088/0264-9381/25/23/235009.

[108] M. Okyay and A. Övgün, "Nonlinear electrodynamics effects on the black hole shadow, deflection angle, quasinormal modes, and greybody factors," *Journal of Cosmology and Astroparticle Physics*, vol. **2022**, no. 01, p. 009, 2022. DOI: 10.1088/1475-7516/2022/01/009. [Online]. Available: https://doi.org/10.1088/1475-7516/2022/01/009.

[109] H. J. Mosquera Cuesta and J. M. Salim, "Non-linear electrodynamics and the gravitational redshift of highly magnetized neutron stars," *Monthly Notices of the Royal Astronomical Society*, vol. **354**, no. 4, pp. L55–L59, 2004. DOI: 10.1111/j.1365-2966.2004.08375.x. [Online]. Available: https://doi.org/10.1111/j.1365-2966.2004.08375.x.

[110] F. Payandeh and M. Fathi, "Isotropic Reissner-Nordström Geometry and the Corresponding Gravitational Redshift," *International Journal of Theoretical Physics*, vol. **52**, pp. 3313–3318, 2013. DOI: 10.1007/s10773-013-1628-x. [Online]. Available: https://doi.org/10.1007/s10773-013-1628-x.

[111] E. Guzman-Herrera and N. Breton, "Light Propagating in a Born–Infeld Background as Seen by an Accelerated Observer," *Annalen der Physik*, vol. **534**, no. 8, p. 2 200 043, 2022. DOI: 10.1002/andp.202200043. [Online]. Available: https://doi.org/10.1002/andp.202200043.

[112] A. Herrera-Aguilar and U. Nucamendi, "Kerr black hole parameters in terms of the redshift/blueshift of photons emitted by geodesic particles," *Physical Review D*, vol. **92**, no. 4, p. 045 024, 2015. DOI: 10.1103/PhysRevD.92.045024. [Online]. Available: https://doi.org/10.1103/PhysRevD.92.045024.

[113] C. W. Misner, K. S. Thorne, and J. A. Wheeler, *Gravitation*. WH Freeman & Company, 1970.

[114] J. Kormendy, R. Bender, A. S. Evans, and D. Richstone, "The mass distribution in the elliptical galaxy ngc 3377: Evidence for a 2 × 108 m⊙ black hole," *The Astronomical Journal*, vol. 115, no. 5, p. 1823, 1998. DOI: 10.1086/300313. [Online]. Available: https://dx.doi.org/10.1086/300313.

[115] E. H. T. Collaboration, "First sagittarius a* event horizon telescope results. i. the shadow of the supermassive black hole in the center of the milky way," *The Astrophysical Journal Letters*, vol. 930, no. 2, p. L12, 2022. DOI: 10.3847/2041-8213/ac6674. [Online]. Available: https://dx.doi.org/10.3847/2041-8213/ac6674.

[116] E. H. T. Collaboration, "First sagittarius a* event horizon telescope results. ii. eht and multiwavelength observations, data processing, and calibration," *The Astrophysical Journal Letters*, vol. 930, no. 2, p. L13, 2022. DOI: 10.3847/2041-8213/ac6675. [Online]. Available: https://dx.doi.org/10.3847/2041-8213/ac6675.

[117] E. H. T. Collaboration, "First sagittarius a* event horizon telescope results. iv. variability, morphology, and black hole mass," *The Astrophysical Journal Letters*, vol. 930, no. 2, p. L15, 2022. DOI: 10.3847/2041-8213/ac6736. [Online]. Available: https://dx.doi.org/10.3847/2041-8213/ac6736.

[118] V. Perlick and O. Y. Tsupko, "Calculating black hole shadows: Review of analytical studies," *Physics Reports*, vol. **947**, pp. 1–39, 2022. DOI: 10.1016/j.

physrep.2021.10.004. [Online]. Available: https://doi.org/10.1016/j.physrep.2021.10.004.

[119] S. Vagnozzi, R. Roy, Y. Tsai, *et al.*, "Horizon-scale tests of gravity theories and fundamental physics from the Event Horizon Telescope image of Sagittarius A," *Classical and Quantum Gravity*, vol. **40**, 2022. DOI: 10.1088/1361-6382/acd97b. [Online]. Available: https://doi.org/1088/1361-6382/acd97b.

[120] D. Amaro and A. Macías, "Geodesic structure of the Euler-Heisenberg static black hole," *Physical Review D*, vol. **102**, no. 10, p. 104 054, 2020. DOI: 10.1103/PhysRevD.102.104054. [Online]. Available: https://doi.org/10.1103/PhysRevD.102.104054.

[121] V. Perlick, O. Y. Tsupko, and G. S. Bisnovatyi-Kogan, "Black hole shadow in an expanding universe with a cosmological constant," *Physical Review D*, vol. **97**, no. 10, p. 104 062, 2018. DOI: 10.1103/PhysRevD.97.104062. [Online]. Available: https://doi.org/10.1103/PhysRevD.97.104062.

[122] L. C. B. Crispino, A. Higuchi, and E. S. Oliveira, "Electromagnetic absorption cross-section of Reissner-Nordström black holes revisited," *Physical review d*, vol. **80**, no. 10, p. 104 026, 2009. DOI: 10.1103/PhysRevD.80.104026. [Online]. Available: https://doi.org/10.1103/PhysRevD.80.104026.

[123] E. Guzman-Herrera and N. Breton, "Light propagation in the vicinity of the ModMax black hole," *Journal of Cosmology and Astroparticle Physics*, vol. **2024**, no. 01, p. 041, 2024. DOI: 10.1088/1475-7516/2024/01/041. [Online]. Available: https://doi.org/10.1088/1475-7516/2024/01/041.

[124] N. Bretón, "Geodesic structure of the Born–Infeld black hole," *Classical and Quantum Gravity*, vol. **19**, no. 4, p. 601, 2002. DOI: 10.1088/0264-9381/19/4/301. [Online]. Available: https://doi.org/10.1088/0264-9381/19/4/301.

[125] X. Liang, H. Chen, and N. X. Sun, "Magnetoelectric materials and devices," *APL Materials*, vol. **9**, no. 4, 2021. DOI: 10.1063/5.0044532. [Online]. Available: https://doi.org/10.1063/5.0044532.

[126] L. Herrera Diez, R. Kruk, K. Leistner, and J. Sort, "Magnetoelectric materials, phenomena, and devices," *APL materials*, vol. **9**, no. 5, 2021. DOI: 10.1063/5.0053631. [Online]. Available: https://doi.org/10.1063/5.0053631.

[127] W. Eerenstein, N. Mathur, and J. F. Scott, "Multiferroic and magnetoelectric materials," *nature*, vol. **442**, no. 7104, pp. 759–765, 2006. DOI: 10.1038/nature05023. [Online]. Available: https://doi.org/10.1038/nature05023.

[128] S. Toyoda, N. Abe, and T. Arima, "Nonreciprocal refraction of light in a magnetoelectric material," *Physical Review Letters*, vol. **123**, no. 7, p. 077 401, 2019. DOI: 10.1103/PhysRevLett.123.077401. [Online]. Available: https://doi.org/10.1103/PhysRevLett.123.077401.

[129] V. Kocsis, K. Penc, T. Rõõm, *et al.*, "Identification of antiferromagnetic domains via the optical magnetoelectric effect," *Physical review letters*, vol. **121**, no. 5, p. 057 601, 2018. DOI: 10.1103/PhysRevLett.121.057601. [Online]. Available: https://doi.org/10.1103/PhysRevLett.121.057601.

[130] M. Zaeimbashi, M. Nasrollahpour, A. Khalifa, *et al.*, "Ultra-compact dual-band smart NEMS magnetoelectric antennas for simultaneous wireless energy harvesting and magnetic field sensing," *Nature communications*, vol. **12**, no. 1, p. 3141, 2021. DOI: 10.1038/s41467-021-23256-z. [Online]. Available: https://doi.org/10.1038/s41467-021-23256-z.

[131] R. Masuda, Y. Kaneko, Y. Tokura, and Y. Takahashi, "Electric field control of natural optical activity in a multiferroic helimagnet," *Science*, vol. **372**, no. 6541, pp. 496–500, 2021. DOI: 10.1126/science.aaz4312. [Online]. Available: https://doi.org/10.1126/science.aaz4312.

[132] F. W. Hehl, Y. N. Obukhov, J.-P. Rivera, and H. Schmid, "Magnetoelectric Cr 2 O 3 and relativity theory," *The European Physical Journal B*, vol. **71**, pp. 321–329, 2009. DOI: 10.1140/epjb/e2009-00203-7. [Online]. Available: https://doi.org/10.1140/epjb/e2009-00203-7.

[133] J. Drori, Y. Rosenberg, D. Bermudez, Y. Silberberg, and U. Leonhardt, "Observation of stimulated Hawking radiation in an optical analogue," *Physical Review Letters*, vol. 122, no. 1, p. 010 404, 2019. DOI: 10.1103/PhysRevLett.122.010404. [Online]. Available: https://doi.org/10.1103/PhysRevLett.122.010404.

[134] T. G. Philbin, C. Kuklewicz, S. Robertson, S. Hill, F. König, and U. Leonhardt, "Fiber-optical analog of the event horizon," *Science*, vol. 319, no. 5868, pp. 1367–1370, 2008. DOI: 10.1126/science.1153625. [Online]. Available: https://doi.org/10.1126/science.1153625.

[135] M. F. Ferreira, E. Castro-Camus, D. J. Ottaway, *et al.*, "Roadmap on optical sensors," *Journal of Optics*, vol. **19**, no. 8, p. 083 001, 2017. DOI: 10.1088/2040-8986/aa7419. [Online]. Available: https://doi.org/10.1088/2040-8986/aa7419.

[136] N. I. Zheludev and Y. S. Kivshar, "From metamaterials to metadevices," *Nature materials*, vol. **11**, no. 11, pp. 917–924, 2012. DOI: 10.1038/nmat3431. [Online]. Available: https://doi.org/10.1038/nmat3431.

[137] V. De Lorenci and L. de Paula, "Analog models for gravity in linear magnetoelectrics," *arXiv preprint arXiv:2205.05149*, 2022. DOI: 10.48550/arXiv.2205.05149. [Online]. Available: https://doi.org/10.48550/arXiv.2205.05149.

[138] C. Barcelo, S. Liberati, and M. Visser, "Analogue gravity," *Living reviews in relativity*, vol. **14**, pp. 1–159, 2011. DOI: 10.12942/lrr-2011-3. [Online]. Available: https://doi.org/10.12942/lrr-2011-3.

[139] U. Leonhardt and T. G. Philbin, "Transformation optics and the geometry of light," in *Progress in optics*, vol. **53**, Elsevier, 2009, pp. 69–152. DOI: 10.1016/S0079-6638(08)00202-3. [Online]. Available: https://doi.org/10.1016/S0079-6638(08)00202-3.

[140] U. Leonhardt and T. G. Philbin, "General relativity in electrical engineering," *New Journal of Physics*, vol. **8**, no. 10, p. 247, 2006. DOI: 10.1088/1367-2630/8/10/247. [Online]. Available: https://doi.org/10.1088/1367-2630/8/10/247.

[141] A. Guerrieri and M. Novello, "Photon propagation in a material medium on a curved spacetime," *Classical and Quantum Gravity*, vol. **39**, no. 24, p. 245 008, 2022. DOI: 10.1088/1361-6382/aca23a. [Online]. Available: https://doi.org/10.1088/1361-6382/aca23a.

[142] H. B. Benaoum, G. Leon, A. Övgün, and H. Quevedo, "Inflation driven by non-linear electrodynamics," *The European Physical Journal C*, vol. **83**, no. 5, p. 367, 2023. DOI: 10.1140/epjc/s10052-023-11481-3. [Online]. Available: https://doi.org/10.1140/epjc/s10052-023-11481-3.

[143] P. Sarkar and P. K. Das, "Emergent cosmology in models of nonlinear electrodynamics," *New Astronomy*, vol. **101**, p. 102 003, 2023. DOI: 10.1016/j.newast.2023.102003. [Online]. Available: https://doi.org/10.1016/j.newast.2023.102003.

[144] J. Gómez-Correa, A. Padilla-Ortiz, A. Jaimes-Nájera, J. Trevino, and S. Chávez-Cerda, "Generalization of ray tracing in symmetric gradient-index media by Fermat's ray invariants," *Optics Express*, vol. **29**, no. 21, pp. 33 009–33 026, 2021. DOI: 10.1364/OE.440410. [Online]. Available: https://doi.org/10.1364/OE.440410.

[145] D. Flores-Alfonso, C. S. Lopez-Monsalvo, and M. Maceda, "Contact geometry in superconductors and New Massive Gravity," *Physics Letters B*, vol. **815**, p. 136 143, 2021. DOI: 10.1016/j.physletb.2021.136143. [Online]. Available: https://doi.org/10.1016/j.physletb.2021.136143.